Title

Advanced Pulse-Shape Analysis and Implementation of Gamma-Ray Tracking in a Position-Sensitive Coaxial HPGe Detector

Author

Kuhn, Austin L

Publication Date

2002-11-01

LBNL-51726

ERNEST ORLANDO LAWRENCE
BERKELEY NATIONAL LABORATORY

Advanced Pulse-Shape Analysis and Implementation of Gamma-Ray Tracking in a Position-Sensitive Coaxial HPGe Detector

Austin L. Kuhn

Nuclear Science Division

November 2002

Ph.D. Thesis

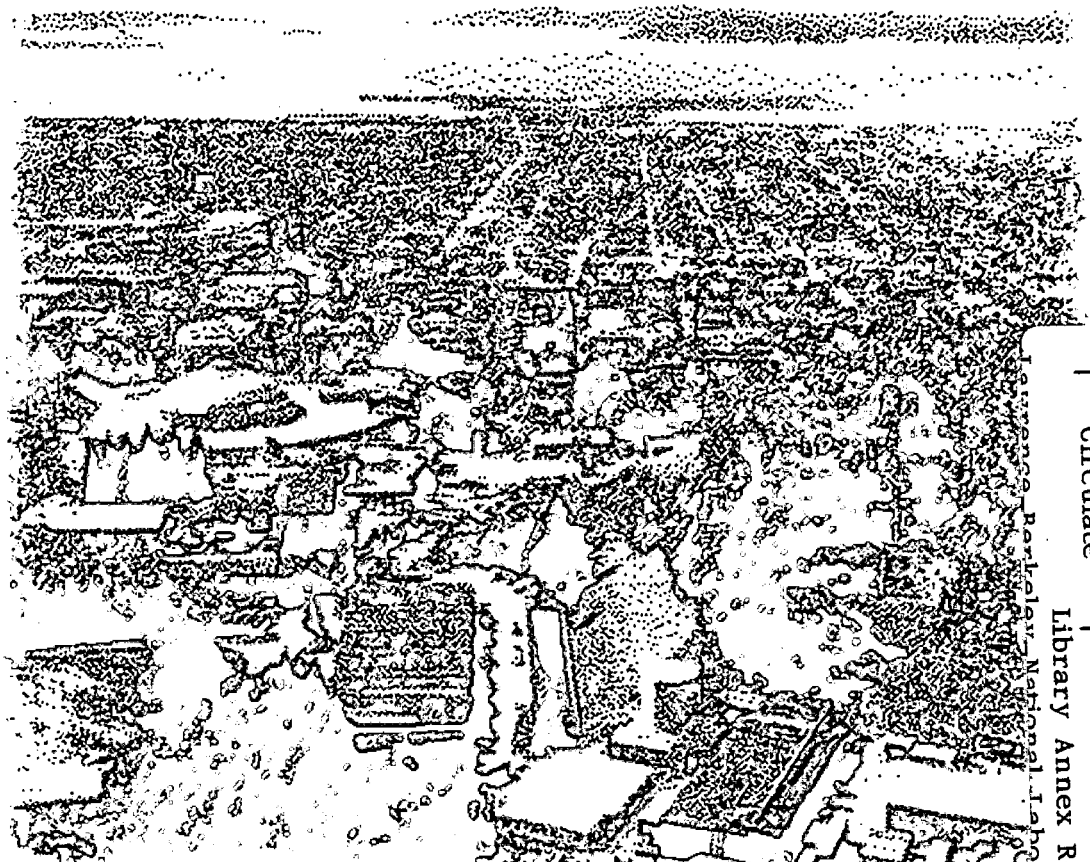

DISCLAIMER

LBNL-51726

Advanced Pulse-Shape Analysis and Implementation of Gamma-Ray Tracking in a Position-Sensitive Coaxial HPGe Detector

Austin Lee Kuhn
Ph.D. Thesis

Department of Nuclear Engineering
University of California, Berkeley

and

Nuclear Science Division
Ernest Orlando Lawrence Berkeley National Laboratory
University of California
Berkeley, CA 94720

November 2002

This work was supported by the Director, Office of Science, through the U.S. Department of Energy under Contract No. DE-AC03-76SF00098.

Advanced Pulse-Shape Analysis and Implementation of Gamma-Ray Tracking in a Position-Sensitive Coaxial HPGe Detector

by

Austin Lee Kuhn

B.S. (United States Merchant Marine Academy) 1997
M.S. (University of California, Berkeley) 1999

A dissertation submitted in partial satisfaction of the

requirements for the degree of

Doctor of Philosophy
in

Engineering - Nuclear Engineering

in the

GRADUATE DIVISION

of the

UNIVERSITY OF CALIFORNIA, BERKELEY

Committee in charge:

Professor Stanley G. Prussin, Chair
Professor Jasmina L. Vujic
Professor Eugene E. Haller

Fall 2002

Abstract

Advanced Pulse-Shape Analysis and Implementation of Gamma-Ray Tracking in a Position-Sensitive Coaxial HPGe Detector

by

Austin Lee Kuhn

Doctor of Philosophy in Engineering-Nuclear Engineering

University of California, Berkeley

Professor Stanley G. Prussin, Chair

A new concept in γ-radiation detection utilizing highly segmented position-sensitive germanium detectors is currently being developed. Through pulse-shape analysis these detectors will provide the three-dimensional position and energy of individual γ-ray interactions and allow the full-energy and direction vectors of the incident radiation to be reconstructed in a process termed tracking.

Here, a prototype segmented detector has been utilized in the assessment of theoretically modeled pulse shapes to gain insight into the factors that effect their agreement with those experimentally measured. It was found that simple modeling of the charge-collection process would provide fair agreement between calculated and experimental pulse shapes. However, in some cases significant deviations between the two were present. This was a result of insufficient modeling of all the processes involved in pulse-shape formation. Factors contributing to this include the three-dimensional spatial distribution of the charge carriers, the path of the primary electron, and

fluctuations in the electric fields near electrode surfaces and due to variations in impurity concentrations.

Additionally, the sensitivity of pulse shapes to changes in the interaction location has been studied. The results indicate that single interactions with energy deposition of 662 keV can potentially be localized to better than the desired position resolution of 2 mm. However, when the study was extended to two interactions totaling 662 keV a different conclusion was reached. It was shown that the pulse shapes resulting from two interactions were ambiguous with that of pulse shapes from single interactions over dimensions greater than 2 mm in the larger detector segments. The size of these segments in future detectors must be reduced in order to increase their sensitivity.

Ultimately, a signal decomposition algorithm was developed and implemented to extract the position and energy of γ-ray interactions, occurring in the prototype detector, from both experimentally measured and simulated pulse shapes. For the first time, this allowed the peak-to-total ratio obtained in the energy spectra of ^{137}Cs, ^{60}Co, and ^{152}Eu to be improved by preferentially removing partial-energy events in the tracking process. Larger gains in the peak-to-total ratio were obtained in the simulation as compared to the experiment. These discrepancies were largely a result of insufficient agreement between the experimentally measured pulse shapes and those theoretically calculated to form the basis pulse shapes in the decomposition process.

Contents

List of Figures

List of Tables

Acknowledgments

There have been many people throughout the course of my graduate studies that have given me the encouragement and assistance I needed to complete this work. First, I would like to thank my academic advisor Stanley Prussin for his unwavering support over the years. He has always encouraged me to address issues fundamentally, to question, and be precise in response. His frank advice, both on an academic and personal level, has been invaluable to me and for that I will always be grateful. I would also like to thank Jasmina Vujic and Eugene Haller for taking the time to serve as members of my dissertation committee. In addition to serving on my dissertation committee, both participated as members of my qualifying exam committee and taught several courses that I enjoyed attending.

The research I took part in at Lawrence Berkeley National Laboratory could not have been completed without the guidance and assistance of Kai Vetter. He encouraged my ideas, provided advice and was there when I needed help. His dedication and persistence to his work always inspired me to excel. He has mentored and taught me by example and I can't thank him enough for that. Additionally, I would like to thank the members of the Nuclear Structure Group and I-Yang Lee. Their fruitful discussions, ideas and continual support have provided me with an excellent working environment.

Of course, my family deserves special thanks. Without them, I couldn't have made it through this. The encouragement and support of my Mom, Dad, Ryan and Katie

has been a motivation throughout my education. They have always been there for me and believed in me throughout it all.

Finally, I want to thank my fiancée Nas for the endless love, support, and friendship she has provided. She has endured my countless complaints about exams, my frustrations with writing a dissertation, and months of separation; yet, through it all she never fails to cheer me up. She has been a source of inspiration in my life.

Chapter 1

INTRODUCTION

Whether it is the outer reaches of distant galaxies, the inner workings of the human body, or inside the nucleus of an atom, scientists have long used electromagnetic radiation as a tool for peering into the unknown. To effectively use it, researchers are often forced to devise innovative ways of detecting the photons, thus, allowing them to obtain such information as the photon energy, incident direction, or intensity to name a few. This radiation can span orders of magnitude in energy. Therefore, each detection device must be designed to best suit the task at hand.

In the field of nuclear structure, γ-ray detection systems designed for energies ranging from approximately 0.1 to 10 MeV are essential components in the study of nuclei. For many decades, semiconductor detectors have been utilized for this task. The first of these detectors were fabricated of germanium which had undergone a lithium drifting process (Ge(Li) detectors) [1]. The lithium acted to compensate the germanium impurities, thereby allowing greater depletion regions to be achieved and thus greater detector volumes. The Ge(Li) detectors also offered an improved energy resolution over that of previously used scintillation detectors such as sodium iodide (NaI). As germanium crystal growing methods advanced, greater purity levels were obtained. This allowed for the production of high-purity germanium (HPGe) detectors [2]. Large

volume detectors with impurity concentrations as low as 10^{10} atoms/cm^3 can currently be fabricated [3].

Today HPGe detectors are used regularly in nuclear structure experimentation. Typically, to perform the experiments an energetic beam of ions, with energies on the order of several MeV per nucleon, is incident on a stationary target material. Depending upon the energy of the incident beam and the make-up of both the beam and target, various nuclear reactions (i.e. inelastic scattering, fusion, etc.) can take place between the two nuclei. These reactions often lead to the production of nuclei in highly-excited states. By selection of the beam energy and the beam and target make-up, researchers can optimize the experiment for the production of the desired nuclei to be studied.

The excited nuclei produced in the reactions generally decay to lower energy states through the emission of multiple discrete energy γ rays. The emitted γ rays occur in sequences, referred to as cascades, where the highly-excited nuclei makes several transitions in energy before reaching its lowest energy state. The detection of these γ-ray cascades provides meaningful information about the properties of the nucleus. The energy and intensity of the γ rays in the cascade give a picture of the energy level scheme of the nucleus. The angular distribution and correlation of emitted γ rays help to determine spins, magnetic moments and static quadrupole moments. However, this information only comes provided the detection system can accurately measure the energy, time and angle of emission of the γ rays in a cascade. With this information, cascades of γ rays can be selected from the large background of unwanted γ rays. The large background is a result of partial-energy deposition in the detection device as well as

γ rays from the reactions taking place between the beam and target which are not of interest.

1.1 Current Detection Systems for Nuclear Structure

1.1.1 Detection System Requirements

In order to isolate specific γ-ray cascades, the detection system must meet several system requirements. One of the most important requirements is that two γ rays close in energy be distinguishable from one another. This allows for good separation between the γ rays of interest and those of the background. This feature is referred to as high energy resolution. As in most systems, efficiency also plays an important role. The detection system as a whole must provide an efficient means for detecting the full energy of the γ rays emitted or high full-energy efficiency. Full-energy efficiency is measured as the number of full-energy events recorded by the detection system divided by the total number of γ rays emitted by the source. Not only should the device have high full-energy efficiency, it should also produce a substantial ratio of the number of full-energy events detected to the total number of events in the energy spectrum (peak-to-total ratio).

The time and angular resolution of the device also have an impact on its performance. Typically, there are many γ rays emitted in a cascade (up to 30 in some cases) and the ability to determine the time of a γ-ray interaction, or time resolution of the system, is important. Adequate time resolution allows multiple γ rays to be correlated to a single cascade. Since the γ rays from a cascade are usually emitted on time scales that

are orders of magnitude smaller than that of the achievable detector time resolution, the cascade is effectively instantaneous for the detection system. In order to separate the multiple γ rays the system must have the ability to localize individual γ rays that are spatially close together. Each of these factors plays an essential part in the overall performance of the detection system.

1.1.2 Compton-Suppressed Arrays

Because the desired information is the total energy of each of the γ rays emitted from the nucleus, γ rays which undergo Compton scattering such that the scattered photon escapes from the detector are not of direct interest and are only a part of the detected background radiation. One way to reduce this background is to remove these events from the energy spectrum whenever possible. Detection systems utilizing Compton-suppression have been used for more than twenty years [4]. This process involves surrounding the primary detection medium (HPGe in this case) with an efficient shielding detector. The shielding detector acts to detect the photons scattering out of the HPGe detector (depositing partial-energy in the detector) and help prevent the scatter of photons between two HPGe detectors. By disregarding γ-ray interactions in the HPGe detector which occur in coincidence (simultaneously) with interactions detected in the shielding detector the background can be reduced. This helps to increase the peak-to-total ratio. For example, the peak-to-total ratio for a single HPGe detector (7 cm in diameter and 9 cm in length) at a γ-ray energy of 1.3 MeV is approximately 20%. The same detector using Compton-suppression has a peak-to-total ratio of approximately 50% [5].

Currently, large detector arrays consisting of numerous Compton-suppressed HPGe detector modules and covering a solid angle of nearly 4π are used to perform high resolution spectroscopy. Figure 1.1 shows a cross section through three detector modules in such an array. Using tapered hexagonal and pentagonal geometry the detector modules can surround the target. Large arrays used today, such as GAMMASPHERE and Euroball, consist of approximately 100 of these modules [6]. Each module consists of a HPGe detector surrounded by a Bismuth Germanate (BGO) scintillation detector. The BGO is an efficient material for absorbing the scattered radiation, several times greater than that of NaI, due to its relatively high density and high atomic number of bismuth.

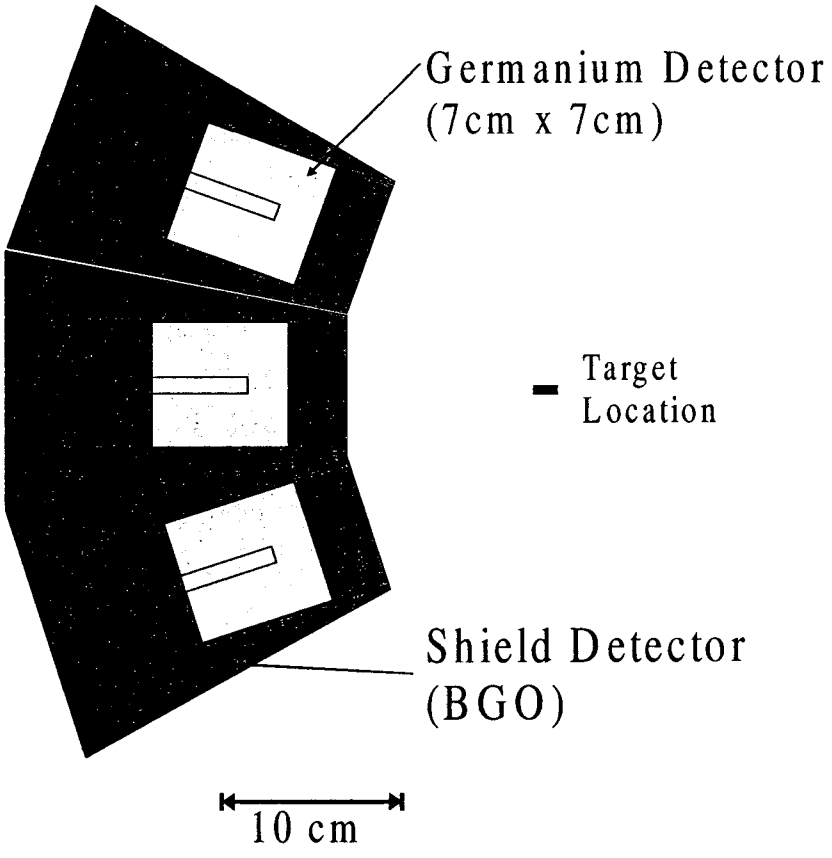

Figure 1.1: Cross section through 3 modules of a Compton-Suppressed Array.

The grouping of Compton-suppressed detector modules into an array provides great advantages over the use of individual modules. The increased coverage in solid angle of the array allows for a more efficient means of detecting rare or weak γ-ray cascades (cascades occurring much less frequently than the majority emitted from the target). A current array such as GAMMASPHERE has a peak-to-total ratio of 53% and a full-energy efficiency of 9% at a γ-ray energy of 1.3 MeV. Besides the obvious improved coverage in solid angle around the target, the arrays also allow for improved angular correlation between emitted γ rays. The current arrays have an angular resolution of about 8°, given by the detector diameter (7 cm) and the target to detector distance (25 cm). Angular resolution also plays a important role in the Doppler shifting of γ-ray energy. Since the γ rays can be emitted from nuclei that are not at rest, a shift in γ-ray energy can be seen dependent upon the angle at which the γ ray was emitted. The relationship between the observed γ-ray energy E' and angle of emission relative to the velocity vector of the source θ is given by:

$$E' = E_o\left(\frac{\sqrt{1-\beta^2}}{1-\beta\cos\theta}\right), \tag{1.1}$$

where β is the velocity of the source divided by the speed of light c, and E_o is the energy of the γ ray when emitted from a source at rest relative to the detection system. The ability to determine angle of emission of the γ rays allows for a correction of the Doppler shift in γ-ray energy to be made.

The improvements brought about by Compton-suppressed arrays have led to many breakthroughs in the field of nuclear structure, one of which was the discovery of so-called "superdeformed" nuclei [7]. These nuclei, at high angular momentum, take the shape of an ellipsoid with an axis ratio near 2. Superdeformed states are produced only in a small percentage of the reactions which take place at the target, therefore it was not until the use of Compton-suppressed arrays that this feature of nuclear structure was able to be detected. A measure of the ability of a detection device to isolate the full-energy peaks in a given γ-ray cascade from a complex energy spectrum is termed its resolving power *RP* [6]. A precise formulation of resolving power can be found in reference [8]. However, here it is only important to understand it in general terms given by the equation:

$$RP = \exp\left[\frac{\ln\left(\frac{N_o}{N}\right)}{1-\frac{\ln\varepsilon}{\ln\left(0.76\left(\frac{E_{sp}}{\delta E}\right)(P/T)\right)}}\right], \tag{1.2}$$

where N is the number of events detected in a given full-energy peak, N_o is the total number of events emitted by the source in a given cascade, E_{sp} is the average energy spacing between full-energy peaks in the cascade, δE is the energy resolution of the detection system, ε is the full-energy efficiency and P/T is the peak-to-total ratio. The parameters that have the greatest influence on the resolving power are the energy resolution δE, peak-to-total ratio P/T, and the full-energy efficiency ε. Increases in these factors give Compton-suppressed arrays a resolving power approximately 100 times

greater than that of an individual Compton-suppressed HPGe detector and 10000 times greater than that of a Ge(Li) detector.

1.1.3 Limitations of Current Arrays

Although Compton-suppressed arrays provide orders of magnitude improvement in resolving power over past systems and brought to light many new phenomena in nuclear structure, there are limitations faced by the current systems. Clearly, the largest drawback with the current arrays is their relatively low full-energy efficiency. This is in part due to the loss in solid angle coverage around the target by the incorporation of the shielding detectors. The entire array covers a solid angle of nearly 4π, however, there is only about 2π coverage by the HPGe. Secondly, efficiency is reduced due to the escaping of scattered γ rays from the germanium. For example, a 1.3 MeV γ ray incident upon a 7 cm diameter by 7 cm length germanium detector only deposits it full energy in the detector about 20% of the time. These factors limit the highest full-energy efficiency that can be reached by Compton-suppressed arrays to approximately 15% [5].

Another limiting factor in the performance of current systems is their angular resolution. As previously mentioned, the angular resolution of the system dictates ones ability to correct for the Doppler shift in energy of emitted γ rays. A finite angular resolution leads to a broadening (degradation in energy resolution) of the γ-ray full-energy peak because of the inability to completely correct for the γ ray's shift in energy. In the current arrays, the angular resolution is limited by the opening angle of individual HPGe detectors given by the target to detector distance of about 25 cm and the 7 cm diameter of the detector. This results in an angular resolution of about 8°. As an

example of Doppler broadening in energy, take the case of a 1 MeV γ ray emitted from a nucleus at the target location with a $\beta = 0.3$. According to Equation 1.1, a detector located at 90° relative to the velocity vector of the nucleus would measure γ rays with a Doppler shifted energy of 0.954 MeV with an uncertainty of $\pm$0.038 MeV given by the angular resolution. This uncertainty leads to a degradation in energy resolution at 1 MeV from the intrinsic value (i.e. when the source and detector are at rest relative to one another) of 0.2% to a value of about 4.2%.

1.2 Detection Systems Utilizing γ-ray Tracking

1.2.1 Concept

A new concept for a γ-ray detection system was proposed and is currently under development at Lawrence Berkeley National Laboratory which aims to address the limitations faced by Compton-suppressed detector arrays. The detector array proposed, called the Gamma Ray Energy Tracking Array (GRETA), will consist of a shell of approximately 100 HPGe detectors each similar in size to that of the detectors in existing arrays. However, there will be no shielding detectors surrounding each of the GRETA HPGe detectors. Each detector will be shaped into a tapered hexagon to fit together forming a spherical shell 9 cm thick with an inner diameter of 24 cm [9]. Furthermore, the outer electrode of each detector will be segmented into 36 electrically isolated sectors. Each segment electrode will collect charge from regions of volume in the HPGe detector dictated by the local electric fields. This process will be investigated in greater detail in the next chapter.

The electrical segmentation of the detectors along with signal processing will allow the energy and position of each γ-ray interaction (i.e. predominantly photoelectric absorption, Compton scattering, and pair production in the energy range of interest) to be determined. In a procedure based on the principles of Compton scattering and photoelectric absorption and termed "tracking", groups of interactions belonging to individual γ rays will be identified, distinction will be made between groups of interactions that comprised the full energy of the γ ray and those that comprise partial energy, and in full-energy groups the sequence in which the interactions occurred will be determined. To achieve this, scattering angles from the known source position (i.e. the target location) are calculated for the γ rays using the energy of each interaction in the Compton scattering formula and then compared to the scattering angles measured using the locations determined for each interaction. Due to the finite position and energy resolution of the system, judgment is made on the agreement between the two sets of scattering angles to determine if the group of interactions likely comprised the full energy of the γ ray or not and, if so, the sequence in which the interactions took place. This ultimately results in the ability to preferentially remove partial-energy events from the detected energy spectrum while maintaining full-energy events and determine the γ rays angle of emission from the source. This process will be thoroughly described in Chapter 5.

1.2.2 System Requirements

In order for a detection system based on γ-ray tracking to provide significant gains over the current systems, there are a few unique requirements the system must meet in addition to the ones mentioned in Section 1.1.1. These new requirements stem from the fact that GRETA will cover a solid angle of nearly 4π around the target with HPGe. Just as in the example in Section 1.1.3, the majority of γ rays in the energy range of interest will not deposit their full energy in a single HPGe detector but will most likely deposit part of their energy in multiple detectors. This does not pose a significant problem if single γ rays are emitted from the target on time scales significantly larger than that distinguishable by the detector (e.g. on the order of 10 ns). In this case, the energy deposited simultaneously in multiple HPGe detectors can be summed together under the assumption of having come from a single γ ray. Therefore, a shell of HPGe 9 cm thick would increase the full-energy efficiency for a 1.3 MeV γ ray to 60% (up from 9% in the Compton-suppressed arrays). However, in reality, multiple γ rays are emitted from the target on the time scale of picoseconds which is much smaller than that distinguishable by the detector. Here, summing of energies, even of those in neighboring detectors, can't necessary be performed due to the significant losses this would cause in the efficiency and peak-to-total ratio because of the possibility of summing energies belonging to separate γ rays.

Therefore, the process of tracking is employed to deal with this problem so a good full-energy efficiency and peak-to-total ratio can be maintained. This places a requirement on the detectors in the array to accurately provide both the energy and position of each γ-ray interaction. As will be discussed in Chapter 5, the greater the

accuracy to which the positions and energies are provided the more effective the tracking process. Current simulations show that GRETA can provide significant gains over the existing arrays with position resolution of 1-2 mm [5]. However, this degree of position resolution can not be achieved by segmentation of the detectors alone. Practical constraints place a limit on the size of the electrical segmentation of the detector and thus lead to segment sizes substantially larger than that of the desired position resolution.

Signal processing is needed to increase the position resolution beyond that of the segmentation size. In this process, the detailed signal shape from the detector will be used to help determine the location of each interaction within the detector. The pulse shape from each of the electrodes in the detector(s) where an interaction(s) has (have) taken place will be digitized. The signals will then be compared to a set of basis signals that have been calculated from theoretical modeling of pulse-shape generation in the detector. A computer algorithm will be used to perform this comparison, which is referred to as the signal decomposition process, and will return a set of interaction locations and energies reproducing the signal generated. This process will be discussed in detail in Chapter 4.

1.2.3 Capabilities

Implementation of a detector system utilizing γ-ray tracking will bring about many new and improved features over that of existing arrays. The ability to reconstruct the path of incident γ rays, allows the target to be surrounded with HPGe detectors without Compton-suppression. This greatly increases the full-energy efficiency of the array. Current estimates show that, with tracking, the full-energy efficiency at a γ-ray

energy of 1.3 MeV will increase to about 55%. The ability to track γ rays allows distinction to be made between γ rays that deposit their full energy in the array from those that deposit only part of their energy. This process also allows γ rays interacting close together (i.e. with interactions separated by about 2 mm) to be separated from one another, including γ rays which interact in the same HPGe detector. These factors lead to an increase in the predicted peak-to-total ratio of the detector system to approximately 85% at a γ-ray energy of 1.3 MeV.

The ability to localize the first interaction of the γ ray within 1-2 mm will have an effect on the angular resolution of the system. Given the current calculations with a position resolution of 2 mm it is predicted that an angular resolution of about 0.5° can be achieved with an array of inner diameter 24 cm at a target to detector distance of 12 cm. This would greatly improve the Doppler energy broadening correction capabilities of the array. For the case mentioned in Section 1.1.3 (a 1 MeV γ-ray energy, with β=0.3, and a detector location of 90°), correction for the Doppler shift in energy would lead to a degradation in energy resolution from 0.2% to only 0.28% (as compared to 4.2% in existing arrays).

As was previously discussed, a measure of the detector arrays sensitivity is given by the systems resolving power (refer to Equation 1.2). The potential improvements in the full-energy efficiency, peak-to-total ratio, and angular resolution lead to a predicted improvement in resolving power of GRETA compared to that of Compton-suppressed arrays. Dependent upon the given experiment to be performed with the array, the improvement in resolving power can be upwards of two orders of magnitude over the Compton-suppressed arrays. Figure 1.2 shows the evolution in resolving power of

various detector systems over time. Each new detection system has led to the recognition and exploitation of many new physical phenomena. It is predicted that GRETA will be beneficial in the study of exotic nuclei (e.g. neutron or proton rich and very far from stability) and nuclei at extreme levels of excitation both of which have cross sections for production yields that are very small.

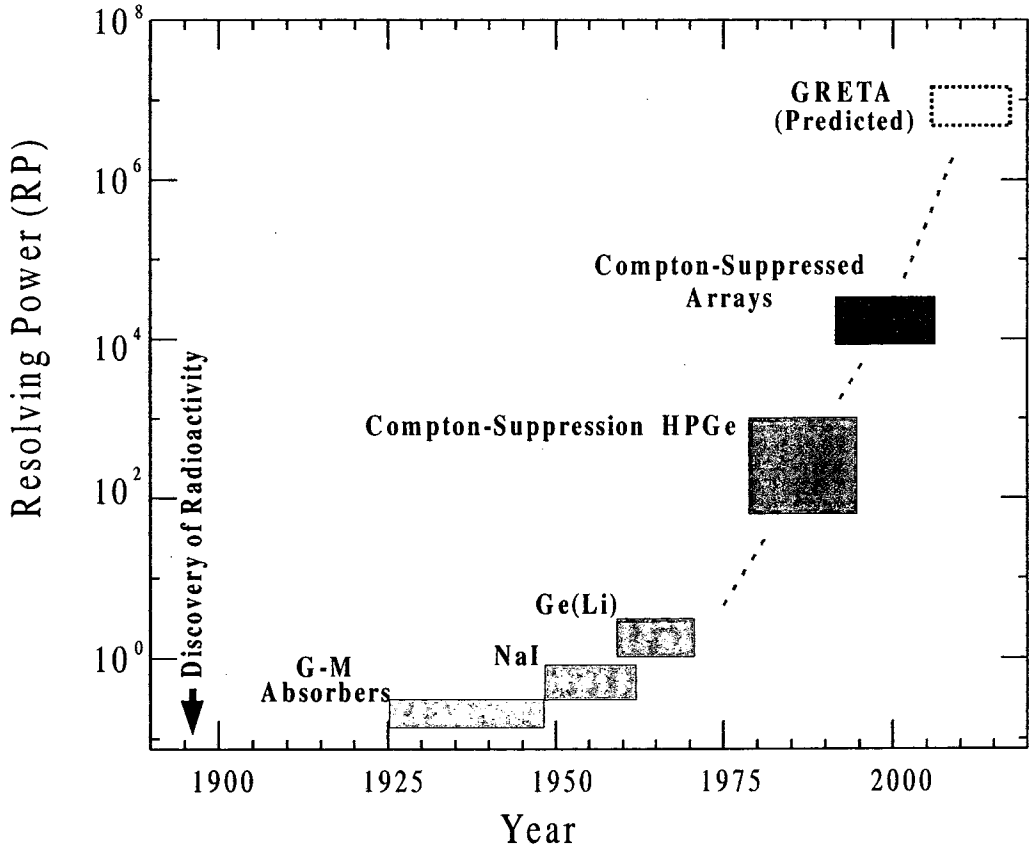

Figure 1.2: Evolution of resolving power, as defined in Eq. 1.2, of various detection systems over the years (after A. O. Macchiavelli [55]).

1.3 Research Overview

The research presented in this dissertation addresses several issues faced in the development of a detection system based on γ-ray tracking. Measurements utilizing a prototype electrically segmented HPGe detector were carried out to assess the ability of theoretical signal calculations to match that of actual measured detector signals. Additionally, investigation was performed to assess the sensitivity of the pulse shapes to changes in the γ-ray interaction location. This was performed for both one and two interactions occurring within a single segment of the detector. Furthermore, a computer algorithm was developed to utilize the signal pulse shapes (both theoretically calculated and experimentally measured) from the detector and return the location and energy of γ-ray interactions within the detector that resulted in the pulse shape input (i.e. signal decomposition). Ultimately, the signal decomposition code along with a tracking algorithm were used to demonstrate, for the first time, the tracking of γ rays with a segmented coaxial HPGe detector.

In the following chapter, background on signal generation in HPGe detectors is discussed as well as the formation of signals in the current segmented prototype detector. It also examines the fundamental aspects of extracting three-dimensional position information from the pulse shapes generated in an electrically segmented detector. Chapter 3 contains investigation into the comparison between calculated signal pulse shapes and those experimentally measured as well as the assessment of the sensitivity of the pulse shapes to interaction location. The signal decomposition code developed to return the location and energy of γ-ray interactions within the detector is presented in

Chapter 4, including simulations performed to assess its capabilities. In Chapter 5, a discussion of the tracking process used to evaluate both simulated and experimentally measured data is presented. Additionally, analysis of results from the implementation of the signal decomposition and tracking for both sets of data is included. Finally, Chapter 6 summarizes the finding of the dissertation and their relation to the GRETA project as well as brief discussion on further applications of γ-ray tracking.

Chapter 2

PRINCIPLES OF GAMMA-RAY DETECTION WITH HIGH-PURITY GERMANIUM DETECTORS

An understanding of the principles involved in γ-ray detection with germanium semiconductor detectors is crucial in the development of pulse-shape analysis methods to determine interaction positions within the detector. Since the theoretical modeling of pulse shapes is important in the methods developed and discussed later in this dissertation for the determination of γ-ray interaction locations within the detector, it is worthwhile examining these principles in detail. These include the physical processes associated with the interaction of electromagnetic radiation with matter, the basic properties of germanium as related to its use in semiconductor detectors, and the factors involved in signal formation within the detector. Each area contributes to ones ability to accurately model the pulse shapes formed by γ-ray interactions.

This chapter will first examine the fundamentals of the interaction of electromagnetic radiation with matter, with emphasis on the processes dominant in the energy range of interest. Secondly, the principles involved in the use of germanium as a semiconductor detector will be investigated. Here, attention will be given to the factors involving signal generation in large high-purity coaxial detectors such as the one used in

this research. These principles will then be extended to a segmented detector and several new aspects of signal formation in such a detector will be explored. Finally, a discussion will be presented on the principles of determining a γ-ray interaction position with a segmented germanium detector.

2.1 Interaction of Electromagnetic Radiation with Matter

Electromagnetic radiation can interact with a material in several ways. The probability that a photon will undergo an interaction per unit path length traveled in a material is called the linear attenuation coefficient, α. With this, a beam of monoenergetic photons incident upon a material of thickness t will be attenuated such that:

$$I = I_o e^{-\alpha t}, \tag{2.1}$$

where I is the intensity of transmitted photons and I_o is the intensity before passing through the material.

For this research, the interest lies in γ radiation with energies from about 100 keV to several MeV. Figure 2.1 shows α as a function of photon energy in germanium. Separate components for the three dominant interaction mechanisms, photoelectric absorption, Compton scattering, and pair production as well as the total linear attenuation coefficient is shown. When one or more of these processes take place within the detector, it results in the transfer of a portion of the γ-ray energy to a primary electron in the germanium. Each process is briefly outlined in the following sections in the context

of γ-ray detection. It is noteworthy mentioning that these processes also play an important part in the tracking process described in Chapter 5.

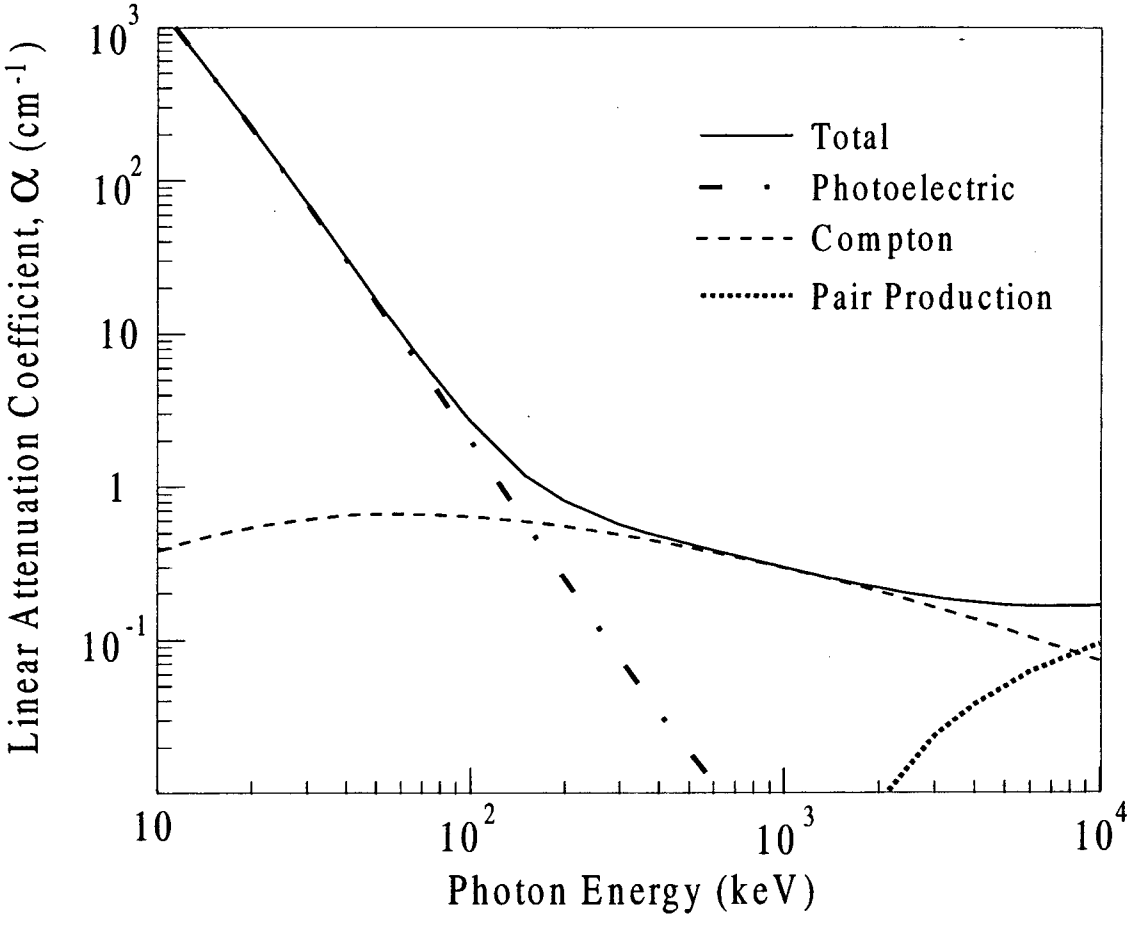

Figure 2.1: Linear attenuation coefficient as a function of photon energy in germanium. The components for the photoelectric absorption, Compton scattering, and pair production are shown as well as the total α (i.e., the sum of each component).

2.1.1 Photoelectric Absorption

A γ-ray incident on the germanium detector and undergoing photoelectric absorption transfers its entire energy to the detection material. The interaction takes place between the incident γ-ray and an atom, resulting in the transfer of energy to an electron in a bound energy shell or the conduction band. The resulting free electron is referred to as a photoelectron and has an energy (E_e) given by:

$$E_e = E_\gamma - E_b \,, \tag{2.2}$$

where E_γ is the energy of the incident γ-ray and E_b is the binding energy of the electron. This process is dominant at relatively low γ-ray energies (up to approximately 200 keV in germanium, see Figure 2.1) [10]. In the case that an atomic electron is ejected in the process, a resulting vacancy is left behind in the electron shell of the atom. The vacancy is quickly filled by an electron in a higher-energy state, leading to the emission of a characteristic x-ray or Auger electron. The x-ray can then transfer its energy by means of a further photoelectric absorption with electrons of higher-energy shells (e.g. less tightly bound). The photoelectrons (and Auger electrons) undergo secondary interactions transferring their energy via ionization of the germanium atoms. This process and its relation to signal formation will be discussed further in Section 2.2.3.

2.1.2 Compton Scattering

In the Compton scattering process, the incident γ ray undergoes an inelastic collision with an electron. The result is a scattered photon with an energy less than the incident γ ray and a free electron with an energy of that lost by the incident γ ray. This

process is illustrated in Figure 2.2. Considering the electron to be free and at rest allows the solution to the conservation of linear momentum to yield the scattered photon energy (E'_γ). This is given by:

$$E'_\gamma = \frac{E_\gamma}{1+(E_\gamma / m_o c^2)(1-\cos\theta)}, \tag{2.3}$$

where E_γ is the incident γ-ray energy, $m_o c^2$ is the rest mass of the electron and θ is the scattering angle of the photon. This formula provides the basis for the tracking process described later in this dissertation. Here it is important to note that the energy deposited in the detector is that of the scattered electron. The scattered electron losses energy through ionization of germanium atoms and other excitation processes just as in the case of photoelectrons. The scattered photon can then undergo one or more interactions (i.e., a single photoelectric absorption or one or more Compton scattering) until finally disappearing in a photoelectric absorption or scattering out of the detector. The Compton scattering process is dominant in germanium for γ-ray energies between approximately 200 keV and 8 MeV. As an example, a 1 MeV γ ray will most likely make four interactions in germanium in order that its full energy is deposited (3 Compton scattering followed by a photoelectric absorption).

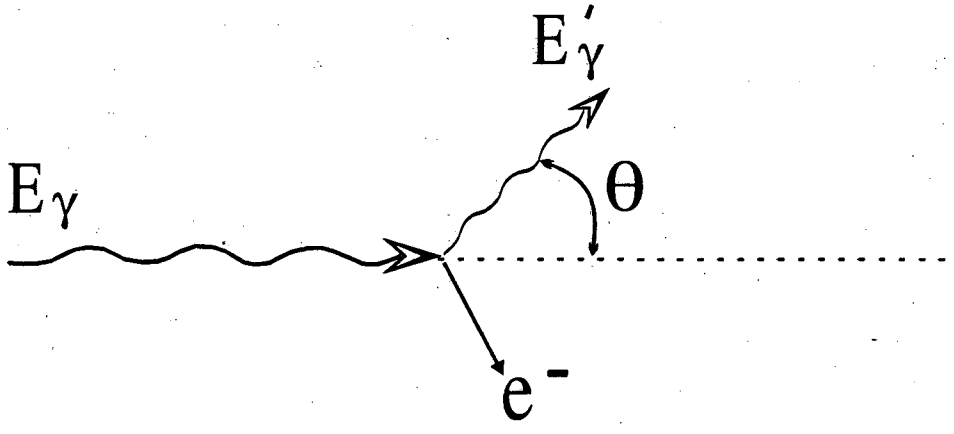

Figure 2.2: Illustration of Compton scattering process.

2.1.3 Pair Production

It is not until γ-ray energies greater than approximately 8 MeV that pair production becomes the dominant interaction mechanism in germanium (see Figure 2.1). Pair production is a threshold process that becomes energetically possible at twice the electron rest mass or about 1022 keV. In the most common process, with nuclei of atomic number larger than about 10, the γ ray interacts with the field of the atomic nucleus and its energy goes into the creation of an electron-positron pair. The energy balance is given by:

$$E_\gamma = E_{e^-} + E_{e^+} + 2m_o c^2 \tag{2.4}$$

Again, E_γ represents the incident γ-ray energy, E_{e^-} and E_{e^+} are the kinetic energy of the electron and position respectively, and $m_o c^2$ is the rest mass of the electron. This process requires the presence of the atom for conservation of momentum, however, the amount of

energy transfer to it is negligible. The electron and position lose their kinetic energy through ionization and other interactions just as in the previous cases. However, as the positron comes to rest it will annihilate with an electron and give rise to the emission of two photons with energies of about 511 keV. These two photons can then interact via photoelectric absorption and Compton scattering before being fully absorbed in the detector or scattering out of the detector.

2.2 High-Purity Germanium Radiation Detectors

2.2.1 Properties

Germanium radiation detectors have been used for decades in the field of high-resolution γ-ray spectroscopy. There are several characteristics of germanium that make it well suited for use as a detection medium for γ rays. One of these is its relatively large atomic number, Z, of 32 as compared to other solid media such as silicon (Z=14). The importance of this is reflected in the cross-sections for the various interaction mechanisms, the photoelectric absorption cross-section is proportional to $Z^{3.5}$, the Compton cross-section is proportional to Z, and the pair production cross-section is proportional to Z^2 [10]. Table 2.1 lists several relevant material properties of germanium.

Atomic Number	32
Atomic Weight	72.60
Density	5.32 g/cm^3
Dielectric Constant	16
Band Gap Type	indirect
Band Gap (@ 300 K)	0.665 eV
Band Gap (@ 0 K)	0.746 eV
Average Energy per e-h pair (@ 77 K)	2.96 eV

Table 2.1: Properties of Ge [3].

The germanium used in the fabrication of HPGe detectors is machined from a single crystal. Germanium in its crystalline form is a semiconductor, meaning that there is a forbidden energy gap between the most weakly bound electrons in the valence band and free electrons in the conduction band. By definition of a semiconductor, this gap must be less than about 3 eV and in germanium the gap is 0.665 eV at 300 K [11]. The crystals can be grown to large sizes with net impurity concentrations of less than 10^{10} atoms cm^{-3} [12,13]. This allows the germanium to be used as a reverse bias diode with large depletion regions. However, due to the large thermally produced leakage current at 300 K the germanium has to be cooled and is typically operated near liquid nitrogen temperature of 77 K.

2.2.2 Closed-ended Coaxial Geometry

The germanium crystal can be machined to several different geometries dependent on the requirements for use of the detector. The geometry of interest in this

research is that of closed-ended coaxial. In the simplest closed-ended coaxial geometry, the germanium crystal is cylindrical in shape. A small diameter hole is bored in the center of the cylinder starting from the back face and extending approximately through 80% of the crystal axis and acts as the central electrode of the reverse bias diode. The outer surface acts as the opposing electrode, with the exception of the back face, which is made to be a neutral surface with no electric field distortions through passivation (US Patent 4,589,006). Typically, boron (a substitutional acceptor atom in germanium) is implanted to form the p+ electrode (the + indicates that the concentration is about 10^{19} atoms/cm^3) and lithium (an interstitial donor atom in germanium) is diffused to form the n+ electrode [14,15].

Although the impurity concentration is extremely low, the germanium is termed n-type or p-type if the impurities are majority donor or acceptor atoms, respectively. Here the interest lies in n-type HPGe. In this case, the p+ electrode is on the outer surface and the n+ electrode is on the central hole. Figure 2.2 shows two cross sections through a closed-ended coaxial detector. Although the detector used in the research presented in this dissertation is not a true cylindrical closed-ended coaxial geometry (i.e. the outer contact is tapered hexagonal not cylindrical), the same principles of charge carrier production and signal generation hold true for both. The more complex geometry of the prototype detector will be discussed in Section 2.3.

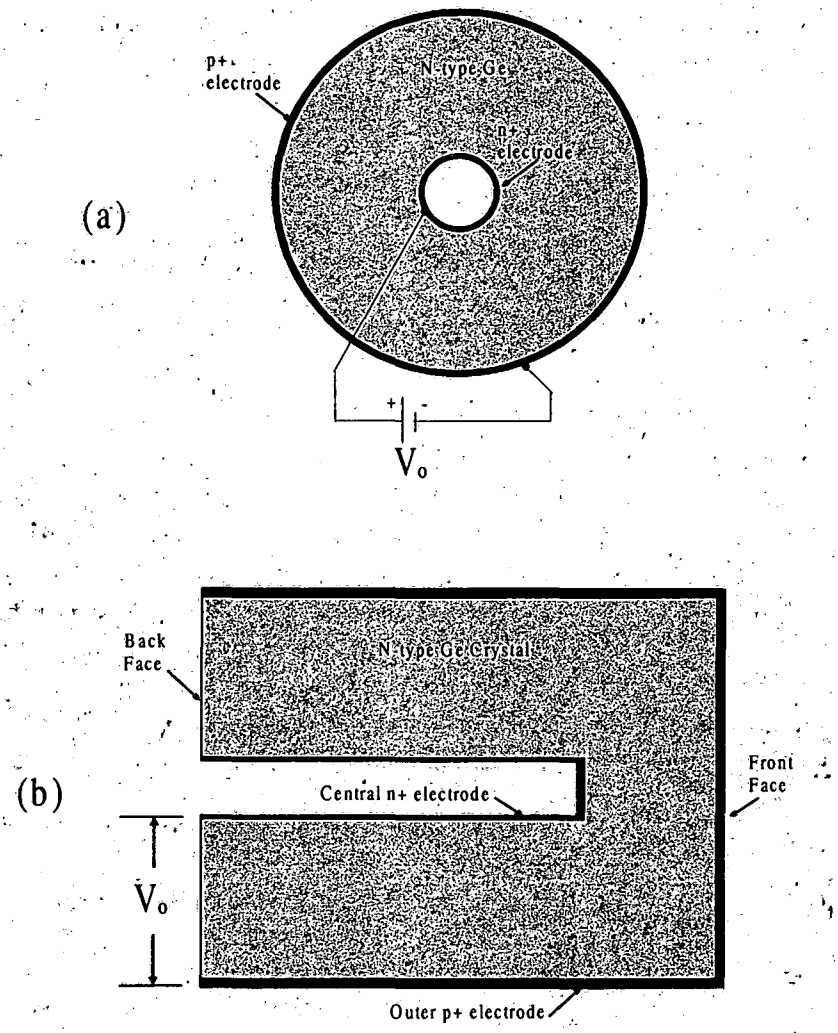

Figure 2.3: Transverse (a) and longitudinal (b) cross sections through a cylindrical closed-ended coaxial Ge detector illustrating the layout of the electrodes, crystal geometry, and applied bias voltage V_o.

2.2.3 Charge Carrier Production

The γ radiation that interacts in the germanium crystal via one of the mechanisms described in Section 2.1 results in the production of an electron (and positron in the case of pair production) with an energy which can be significantly higher than that of the electrons bound in the lattice. The high-energy electron subsequently transfers about half

of its energy to the crystal via direct and indirect ionization of the electrons in the lattice and the rest through non-ionizing excitations (i.e. phonons). This occurs both directly by the primary high-energy electron and by secondary electrons which have gained energy from the primary. The ionization process results in the formation of a cloud of charge in the region of the interaction. This cloud of charge has a size on the order of the stopping distance of the primary high-energy electron. For example, a 1 MeV electron brought to rest in germanium via ionization interactions has a range of just less than 1 mm [16]. This is an important factor in the position resolution achievable with HPGe detectors and will be discussed later in this context.

The charge cloud produced consists of the electrons moved into higher-energy states in the conduction band and the vacancies left behind in the valence band called holes. The holes behave as net positive charge in the crystal and have distinct charge carrier properties that differ from those of the electrons. Since each electron raised to the conduction band leaves a corresponding hole in the valence band, the two sets of charge carriers are referred to as electron-hole pairs. An important factor in charge carrier formation is the average energy spent by the primary electron to produce one electron-hole pair. This quantity has a value of 2.96 eV in germanium at 77 K [3] and is essentially independent of the primary electron energy. This allows for a direct relation between the number of electron-hole pairs produced and the energy deposited by the incident γ-ray.

2.2.4 Signal Generation

In order to obtain useful information from the distribution of electron-hole pairs formed (such as energy and position of the interaction) an electrical signal is generated. A potential is placed across the electrodes of the detector as shown in Figure 2.3. This creates a depletion region throughout the majority of the crystal. The value of the potential Φ is given by the Poisson equation:

$$\nabla^2\Phi(r) = -\frac{\rho(r)}{\varepsilon}, \tag{2.5}$$

where ε is the dielectric constant of germanium, and $\rho(r)$ is the net space charge density which is a function of location in the crystal (r). The space charge density represents the net-ionized donor impurity sites in n-type HPGe, and is given by:

$$\rho(r) = eN_D(r). \tag{2.6}$$

Here, $N_D(r)$ is the local net-donor concentration and e is the electronic charge. The applied potential generates a strong electric field across the detector crystal. The electric field value (E) can be obtained through solution of the equation:

$$E(r) = -\nabla\Phi(r). \tag{2.7}$$

For complex geometries, it is useful to solve the potential and electric field numerically by employing finite element methods.

The electric field present in the detector prevents the recombination of the electron-hole pairs generated after a γ-ray interaction takes place. The force acting on both the electrons and holes in the presence of the electric field causes them to drift toward opposing n+ (anode) and p+ (cathode) electrodes, respectively. The value of the charge-carrier drift velocity (v) for low electric fields is given by:

$$v_{e,h}(r_{e,h}) = \mu_{e,h} E(r_{e,h}), \tag{2.8}$$

where $\mu_{e,h}$ is the electron (e) or hole (h) mobility and $E(r_{e,h})$ is the electric field at position $r_{e,h}$ for the electrons or holes, respectively. The mobility of the charge carriers is dependent upon several factors and is defined as:

$$\mu_{e,h} = \frac{e\tau}{m^*_{e,h}}, \tag{2.9}$$

where e is electronic charge, τ is the mean time between collisions and $m^*_{e,h}$ is the effective mass of the electron or hole. The effective mass varies dependent upon the direction of travel of the charge carriers relative to the crystallographic axes (i.e. <100>,<111>, ect.). The change in effective mass causes a change in the mobility of the carriers, and at high electric fields leads to a significant anisotropy in the drift velocity of

the carriers. The study of this effect and its impact on signal generation in HPGe detectors can be found in reference [17-20].

As the charge carriers drift, mirror charge is induced at the electrodes and a current is produced. The current, *I(t)*, which is produced in the detector is related to the induced charge by:

$$I(t) = \frac{dQ}{dt}. \tag{2.10}$$

Here, dQ represents the total differential charge which is induced by the motion of both the electrons and holes (i.e. $dQ = dQ_e$ (electrons) + dQ_h (holes)). Furthermore, the differential charge $dQ_{e,h}$ induced by the motion of the charge carriers from position $r_{e,h}$ to $(r_{e,h} + dr_{e,h})$ can be obtained through solution of the equation:

$$dQ_{e,h} = \frac{qE(r_{e,h})dr_{e,h}}{V_o}, \tag{2.11}$$

where q is the charge deposited in the detector ($q = ne$, where n is the number of electron-hole pairs and e is electronic charge), and V_o is the applied reverse bias voltage across the crystal. However, as will be seen in the following chapter, it is important to obtain the induced charge as a function of time in order for theoretical calculations of detector signals to be made. Accordingly, a relation can be obtained by using the drift velocity v = *dr/dt*. This yields the equation:

$$dQ = \frac{q}{V_o}\left(E(r_e)\mathrm{v}_e + E(r_h)\mathrm{v}_h\right)dt\,. \tag{2.12}$$

Here, the separate contributions from both the electrons and holes to the total induced charge are shown. Their contribution will be different due to the fact that the drift velocity for electrons and holes differ and they experience different electric fields as they drift.

The induced charge on the electrodes rises as the charge carriers approach opposing electrodes and a maximum value is reach when both pairs have been collected. The maximum, in an ideal crystal (i.e. no trapping of charge carriers), is equal to the charge deposited q. This means that, on average, the amount of charge collected is proportional to the energy deposited in the interaction.

2.3 Segmented HPGe GRETA Prototype Detector

2.3.1 Detector Description

The HPGe detector that was utilized for the measurements presented in this dissertation was designed as a prototype for the GRETA project at Lawrence Berkeley National Laboratory and manufactured by Eurisys Mesures. Accordingly, it was designed to fit into a spherical shell of tapered hexagonal detectors, as described in the previous chapter. The prototype detector consists of a closed-ended n-type HPGe crystal with the outer surface tapered in a hexagonal shape. The crystal geometry is illustrated in

Figure 2.4. The length of the crystal is 9 cm with a diameter at the back of 7 cm and a maximum diameter at the front of 4.4 cm. The outer surface has a 10° taper angle. The inner electrode hole extends 7.5 cm from the back face with a diameter of 1 cm.

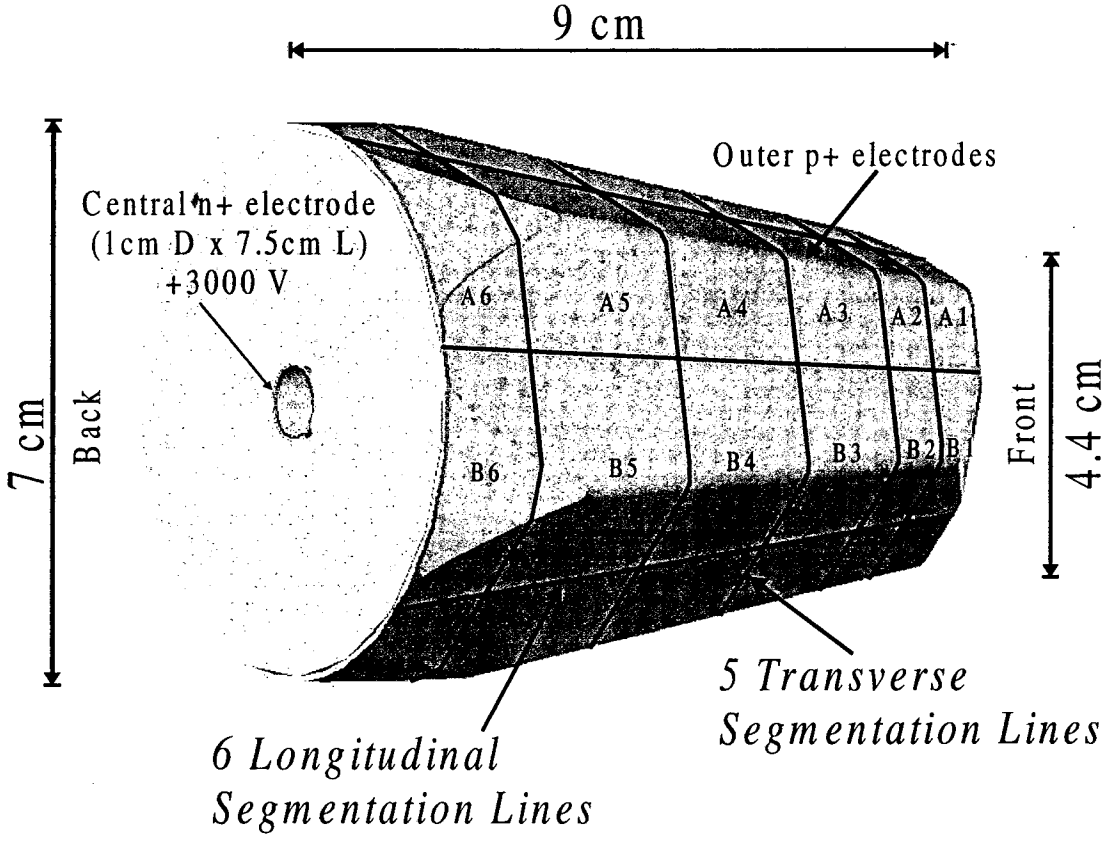

Figure 2.4: The GRETA prototype detector crystal.

The outer electrode is electrically segmented into 36 individual segments. This is accomplished with six longitudinal boundaries lying on the flat surfaces of the taper and five transverse boundaries. The spacing between the transverse boundaries starting at the front face and ending at the back face are 0.75, 0.75, 1.5, 2.0, 2.5 and 1.5 cm,

respectively. It is important to note, for future reference, that the segments are referred to by numbers 1 to 6 from the front face to back face along with letters A to F in the azimuthal direction (see Figure 2.4). The segmentation geometry was chosen as a means of studying the effects of the various segment sizes on the sensitivity of the pulse shapes [21]. This will be addressed in the pulse-shape analysis studies presented in Chapter 3.

In order to simulate the geometry that will be needed to closely pack multiple detectors in a spherical shell, the Ge crystal is encased in a 1 mm thick aluminum can with the same shape as that of the crystal. There is a 1 mm separation between the Ge crystal and the aluminum can. The field effect transistors (FETs) for each of the segments, which act as the first stage of the preamplifier, are located and cooled in the same vacuum system as the crystal. Cooling of the FETs reduces the noise on the signal providing for increased energy resolution [22-24] as well as being beneficial for the determination of the locations of the γ-ray interactions. The energy resolution, measured experimentally at photon energies of 59.54 keV and 1332.5 keV, for each of the working segments is listed in Table 2.2. It is important to note that, as delivered, one segment (D6) of the detector did not produce an output signal. To bypass this problem, this segment was shorted together with segment D5. This resulted in a larger capacitance for segment D5 and is reflected in the degradation in energy resolution measured for that segment. The output from the FETs of two segments, E3 and E5, were lost shortly after receiving the detector. In general, the energy resolution values measured for the working segments were in good agreement with average values of 1.41 and 2.15 keV at energies of 59.54 and 1332.5 keV, respectively.

Segment	Energy Resolution @ 59.54 keV	@ 1332.5 keV	Segment	Energy Resolution @ 59.54 keV	@ 1332.5 keV
A1	1.25	2.10	D1	1.20	1.96
A2	1.26	1.98	D2	1.19	1.94
A3	1.40	2.02	D3	1.42	2.00
A4	1.51	2.09	D4	1.43	2.11
A5	1.47	2.23	D5	2.22	2.80
A6	1.70	2.40	D6	xxx	xxx
B1	1.22	2.07	E1	1.29	2.10
B2	1.17	2.20	E2	1.26	1.94
B3	1.32	2.02	E3	xxx	xxx
B4	1.35	2.18	E4	1.55	2.11
B5	1.80	2.59	E5	xxx	xxx
B6	1.46	2.25	E6	1.58	2.41
C1	1.23	1.96	F1	1.29	1.97
C2	1.18	2.05	F2	1.19	2.01
C3	1.30	2.01	F3	1.36	2.04
C4	1.51	2.14	F4	1.45	2.19
C5	1.56	2.26	F5	1.50	2.40
C6	1.41	2.30	F6	1.42	2.20

Table 2.2: Measured energy resolution for each of the detector segments at 59.54 and 1332.5 keV. The average uncertainity was $\pm$ 0.01 and $\pm$ 0.02 keV for the 59.54 and 1332.5 keV γ-ray energies, respectively.

2.3.2 Signal Generation in a Segmented Detector: Transient Induced Charge Signals

The same basic principles of charge carrier formation and signal generation outlined in Sections 2.2.3 and 2.2.4 hold true for the segmented prototype detector. However, in a segmented detector, charge can be induced on multiple electrodes by the drift of electrons and holes. This phenomenon gives rise to the formation of "transient induced signals". The time dependence of the signals induced at each segment electrode depends upon the factors given in Equation 2.12. However, since multiple sensing

electrodes are involved, the electric field vector (E) requires derivation from the weighting potential for the electrode of interest.

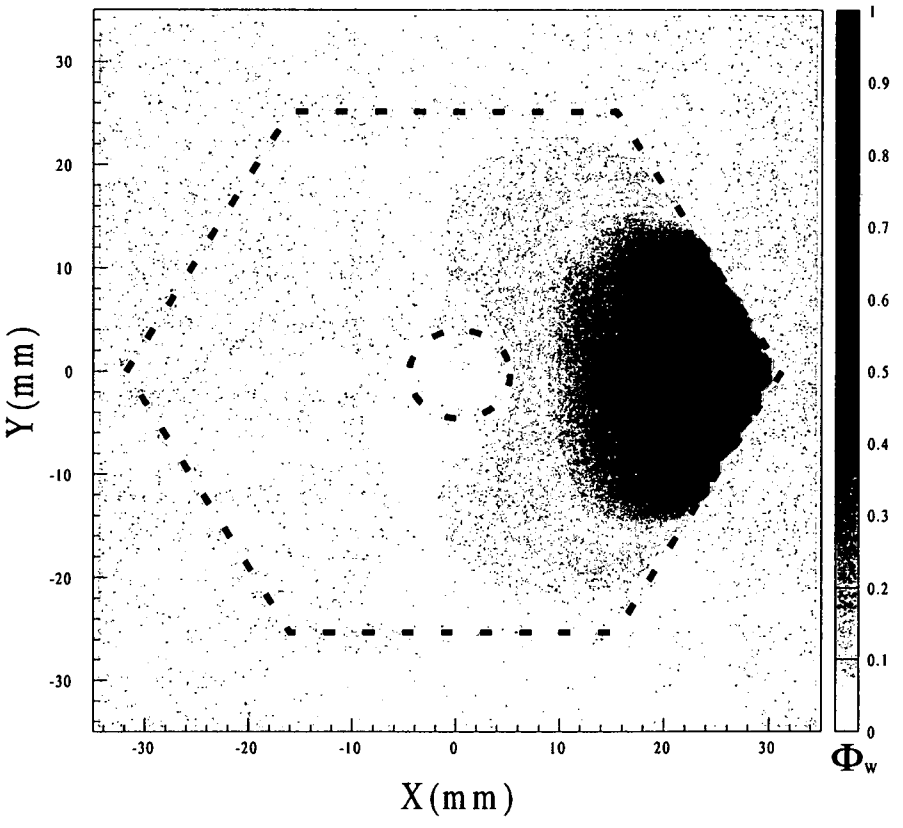

Figure 2.5: A cross section through the detector crystal illustrating an intensity plot of the calculated weighted potential for one segment.

The weighting potential is a fractional measure of the capacitance of an infinitesimal electrode and the sensing electrode [25]. It represents the electrostatic coupling between the charge carriers and a given sensing electrode. In order to perform the theoretical calculation of detector signals from each segment, the weighting potential is needed. The solution can be obtain through the use of Ramo's theorem and is described in reference [26]. Figure 2.5 shows a cross section through the fourth layer of

segments and the calculated weighting potential for one segment. It is important to note that the weighting potential is only a mathematical formulation and not a true physical potential. The true operating potential, determined by the applied bias voltage, is what dictates the motion of the charge carriers. The calculated operating potential, for the same cross section through the detector as in Figure 2.5, can be seen in Figure 2.6.

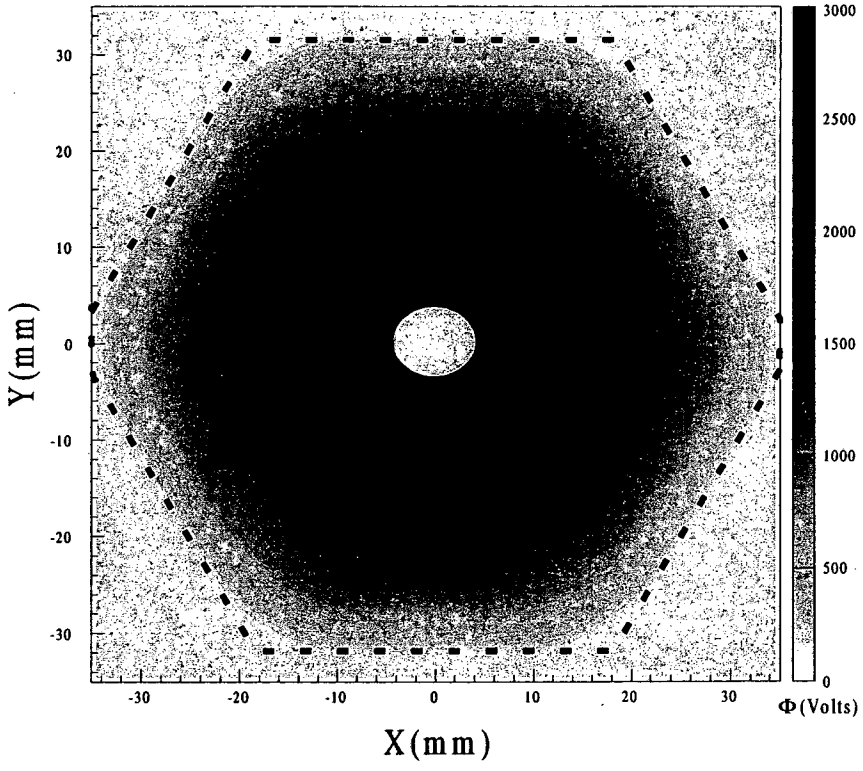

Figure 2.6: Intensity plot of the calculated potential through the same cross section of the detector crystal as illustrated in Figure 2.5.

As a simple illustration of the pulse shapes generated, Figure 2.7a shows a cross section through the fourth layer of segments in the detector, the location of a γ-ray interaction and the respective drift path of the electrons and holes. When the charge

carriers are at a large distance from their destination electrode (i.e. the central electrode for the electrons and outer electrodes for the holes), the mirror charge induced by the drift of the carriers is distributed over several segment electrodes. As the charge carriers drift, the weighted potential (shown in Figure 2.5) for any given electrode varies along their path. This variation dictates the shape of the pulse produced at each electrode according to Equation 2.12.

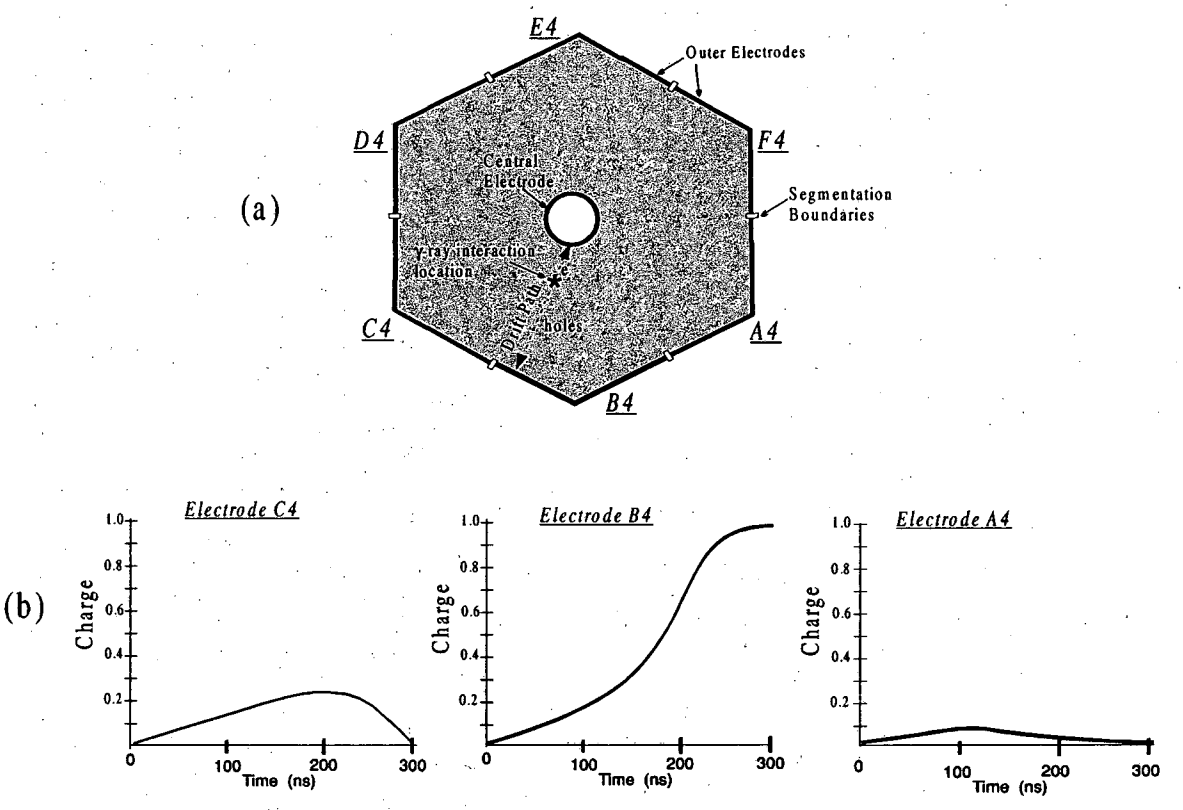

Figure 2.7: (a) Cross section through fourth layer of segments illustrating the location of a γ-ray interaction and the drift path for both electrons and holes. (b) Corresponding charge signals produced at three segment electrodes.

Figure 2.7b shows the charge signals generated at the electrodes of three neighboring segments (A4, B4, and C4) from the γ-ray interaction in Figure 2.7a. In the early stages of signal generation ($0 \leq$ time ≤ 100 ns), the induced charge steadily increases on each of the three electrodes as the charge carriers drift. In this case, the interaction takes places close to the central electrode and the electrons, having a shorter distance to travel, will complete the collection process before the holes. Accordingly, at times between 100 and 200 ns, only the holes are left to drift toward electrode B4 (close to the C4 boundary) and the induced charge decreases on electrode A4 as the weighted electric field for that electrode decreases. The drift of the holes continually increases the induced charge on electrodes B4 and C4 until a time of approximately 200 ns. At about this time, the holes near the destination electrode of B4 and the amount of induced charge on C4 decreases. At the end of the charge collection process, a net charge is measured on the B4 electrode and the induced charge on the neighboring electrodes of A4 and C4 return to zero. Hence, the signals on the neighboring electrodes to that which "charge collection" takes place are referred to as "transient". It is important to point out the difference in shape and maximum amplitude of the transient signals. These features are crucial in determining the interaction position and will be discussed in this context in the following section. A more in-depth investigation into the formation and modeling of the pulse shapes will be covered in Chapter 3.

2.3.3 Localization of γ-ray Interactions

It is possible, and often necessary in many applications, to extract more than the energy of the interacting γ-ray from the detector signal. Many signal-processing techniques have been developed to extract the time of the interaction, the type of radiation, and rough estimations of the mean position of the interactions [27-30]. However, in the tracking of γ rays, as considered here, three-dimensional position resolutions on the order of 1-2 mm are needed. In the electrically segmented detector, simple determination of the charge-collecting electrode will give a position resolution on the order of the segment size. Manufacturing restraints limit the size of the electrical segmentation on the outer electrode of the detector. This leads to segment sizes that are substantially larger than the desired position resolution needed in the implementation of tracking γ rays. Therefore, signal processing techniques which use the detailed pulse shape from each segment electrode are needed to determine the locations of γ-ray interactions within the volume of the detector to better than that of the segment size.

Studies with non-segmented coaxial detectors have shown that the position of a γ-ray interaction, in one dimension (the direction of charge carrier drift), can be inferred from the pulse shape. The varying drift times of the electrons and holes, dependent upon the location of the interaction, provide the necessary shape changes in the charge signal to allow for the extraction of position information. Such processes are described in reference [17,30,31]. However, without electrical segmentation on the outer electrode, the pulse shape is only sensitive in one dimension. By segmenting the outer electrode, three-dimensional position information can be obtained. In addition to the pulse shape from the segment electrode collecting the charge, the "transient" induced pulse shapes on

the neighboring electrodes provide the added information necessary to resolve the interaction position in three dimensions.

As an example, Figure 2.8a shows a cross section through the detector in fourth sets of segments and two γ-ray interaction positions labeled 1 and 2, which result in net charge collection in segment B4. Because the two positions are symmetric about the centerline of segment B4, the pulse shapes generated at that electrode for the case of a single γ-ray interaction at position 1 or position 2 will be identical. This can be seen in the resulting pulse shapes in Figures 2.8b and 2.8c. The figures also illustrate how the induced signals on the neighboring segment electrodes of A4 and C4 act to break the symmetry of the two interactions. The pulse shape seen on electrode A4 and C4 are interchanged for the two different interaction positions. A similar illustration can be made with interactions occurring at different depths (the direction perpendicular to the plane of the cross section) in the detector. In this case, the symmetry would be broken by the neighboring segments of B3 and B5. This clearly illustrates the importance of the detailed pulse shape from each of the detector electrodes in determining the position of an interaction. It will be the focus of the following chapter to examine the sensitivity of the pulse shapes to the location of a γ-ray interaction dependent upon such variables as signal noise and segment size.

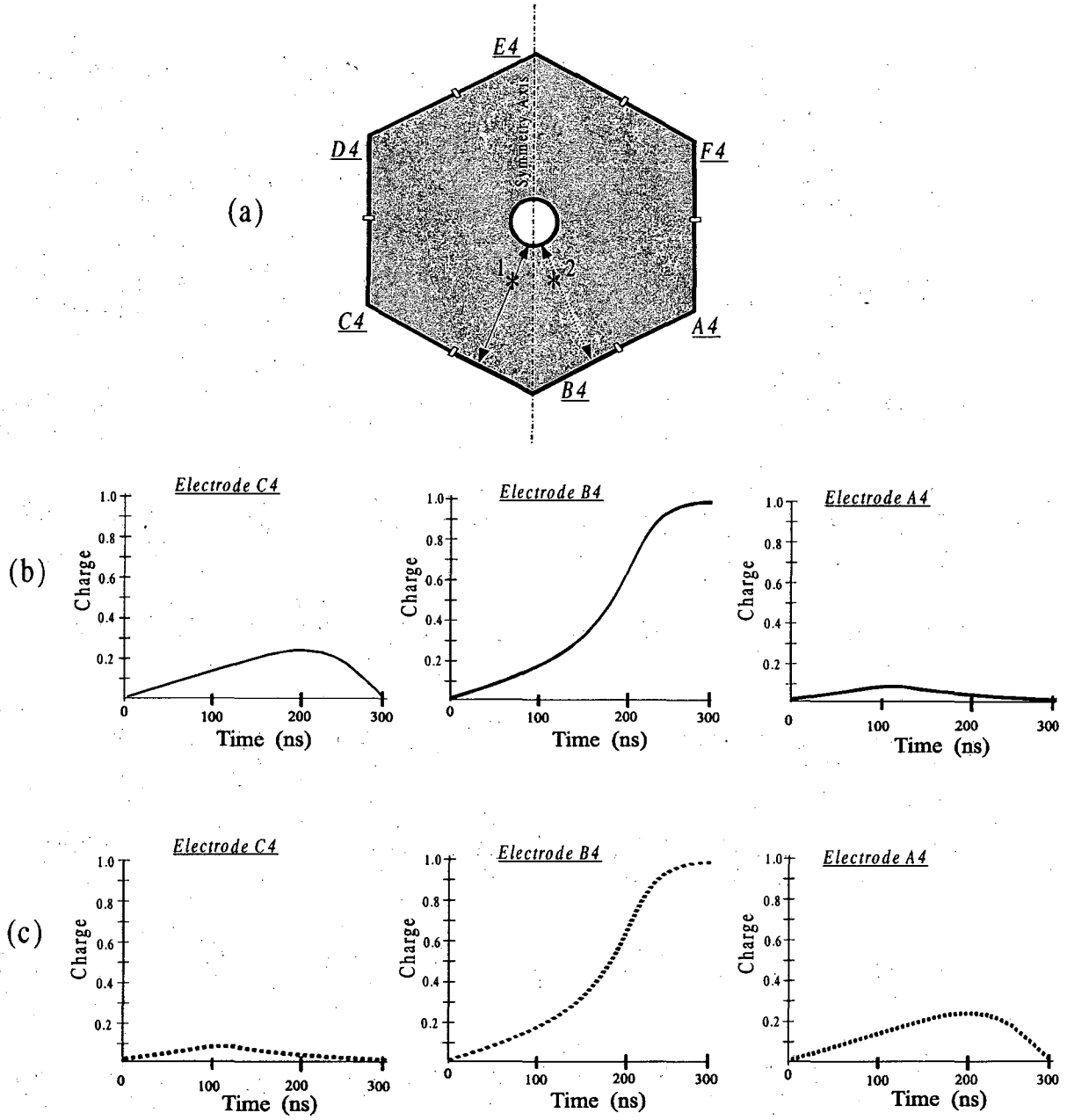

Figure 2.8: (a) Cross section through detector crystal in the fourth layer of segments illustrating γ-ray interaction locations 1 and 2 (*). (b) Pulse shapes produce at three electrodes for interaction 1. (c) Same as (b) for interaction at 2.

Chapter 3

EXAMINATION OF THE PROTOTYPE DETECTOR PULSE SHAPES AND POSITION SENSITIVITY STUDIES

Determination of the location of a γ-ray interaction in three dimensions within the detector volume to an accuracy better than the segmentation size, requires the use of the detailed pulse shapes from each of the segments. As illustrated in the previous chapter, the change in the signal shape at each segment electrode provides the means for extraction of position information. This point raises a fundamental question. How sensitive is the pulse shape to a change in interaction location, relative to the uncertainty in the signal itself (i.e. the noise)? Quantifying this sensitivity provides a measure of the ability to localize an interaction based on the pulse shapes generated. Since the factors involved in pulse-shape generation change with location in the detector, so too does the sensitivity. Unfortunately, it is not feasible to make this comparison using experimentally measured pulse shapes from single γ-ray interactions throughout the detector volume. Therefore, one must rely on theoretically calculated pulse shapes. This, in turn, raises a separate issue addressing the accuracy to which the theoretically calculated pulse shapes can represent those generated within the detector. The accuracy of modeled pulse shapes is also of importance in the signal decomposition process

developed and outlined in Chapter 4. Because it is not feasible to construct such a process using experimentally measured pulse shapes, the signal decomposition process relies on the use of theoretically modeled pulse shapes.

The aim in this chapter is to address issues associated with the accuracy of the calculated pulse shapes and to quantify the sensitivity of pulse shapes to changes in the interaction location. The following section will describe the model used in the generation of pulse shapes. In Section 3.2, the experimental measurements performed to verify the accuracy of the theoretical pulse shapes are described. In addition, a discussion is included on the agreement between the model and measurements addressing the factors limiting the model. The studies performed to quantify the sensitivity of the pulse shapes to a change in interaction location (termed "position sensitivity") are presented in Section 3.3. The studies include sensitivities for both single and double γ-ray interactions in one segment of the detector. These studies were performed for the most part with calculated pulse shapes so that the entire volume of the detector crystal could be covered. However, in the select regions where pulse shapes were experimentally measured they were used and compared to modeled results. Finally, a discussion of the findings is included.

3.1 Calculation of Charge Signals

The theoretical calculations utilized to model detector pulse shapes are important in several respects. First, the studies performed to examine the sensitivity of the current prototype detector rely on the use of such calculations. In addition, the signal decomposition process developed also makes use of the calculated pulse shapes. It is

important to note that the process of modeling pulse shapes was developed prior to the research presented in this dissertation. However, it is important to outline the process developed to provide a sound understanding of the assumptions of the model. The experiments performed to assess the accuracy of the address such assumptions by comparing the experimentally measured and calculated pulse shapes.

The objective of model is to calculate pulse shapes resulting from charge-carrier generation at a specified location within the current prototype detector. This is performed by finding an approximate solution to Equation 2.12. First, solution to the Poisson equation (Equation 2.5) for the given detector geometry and applied bias voltage V_o (+3000V) is obtained by employing finite element methods. Here, the net space charge density $\rho(r)$, which is location dependent, must be approximated. The manufacturer of the prototype detector provides average impurity concentration values, N_D, of 11 X 10^9 atoms/cm^3 and 6 X 10^9 atoms/cm^3 at the front and back face of the detector, respectively. Therefore, a linear variation is assumed from the front to the back face, which effectively yields $\rho(z)$ (the Z-direction being perpendicular to the front and back face). However, it is known that variations in the impurity concentration from the mean are also present in other directions [32]. Solution to the Poisson equation yields the potential $\Phi(r)$. Rather than repeat this process each time the potential is needed at different locations, values of $\Phi(r)$ are stored at locations ("grid points") separated by 1 mm throughout the detector volume (the calculated potential for a cross section of the detector was shown previously in Figure 2.6). With this information, Equation 2.7 is solved for the electric field $E(r)$ at each grid point.

Using the electric field determined in this way, the drift path of the charge carriers is calculated for a given γ-ray interaction location. Several assumptions are made in this process. The time required for formation of electron-hole pairs and the time interval for the pairs to reach the velocity given by the local electric field are assumed to be negligible compared to the total drift time of the charge carriers. In addition, the range of the primary electron and finite size of the electron-hole pair distribution is neglected. Therefore, it is assumed that the charge-carrier distributions are represented by a point charge drifting along the field lines. These assumptions will be discussed in Section 3.2.3 in further detail. The initial trajectory of the electrons and holes is determined by interpolating the electric field between grid points for the given γ-ray interaction site. The relation expressing the charge carrier drift velocity as a function of electric field and crystal orientation is taken from references [18,19]. With this, the path of the charge carriers is determined for a finite time interval (Δt) chosen to be 1 ns. The time interval is chosen to be small compared to the total drift time (~200-500 ns dependent upon location in the crystal) preventing large discontinuities in the drift velocity. This process is repeated until both electrons and holes reach the inner and outer electrodes, respectively. Figure 3.1 shows calculated drift paths for both the electrons and holes for an interaction located in segment B4.

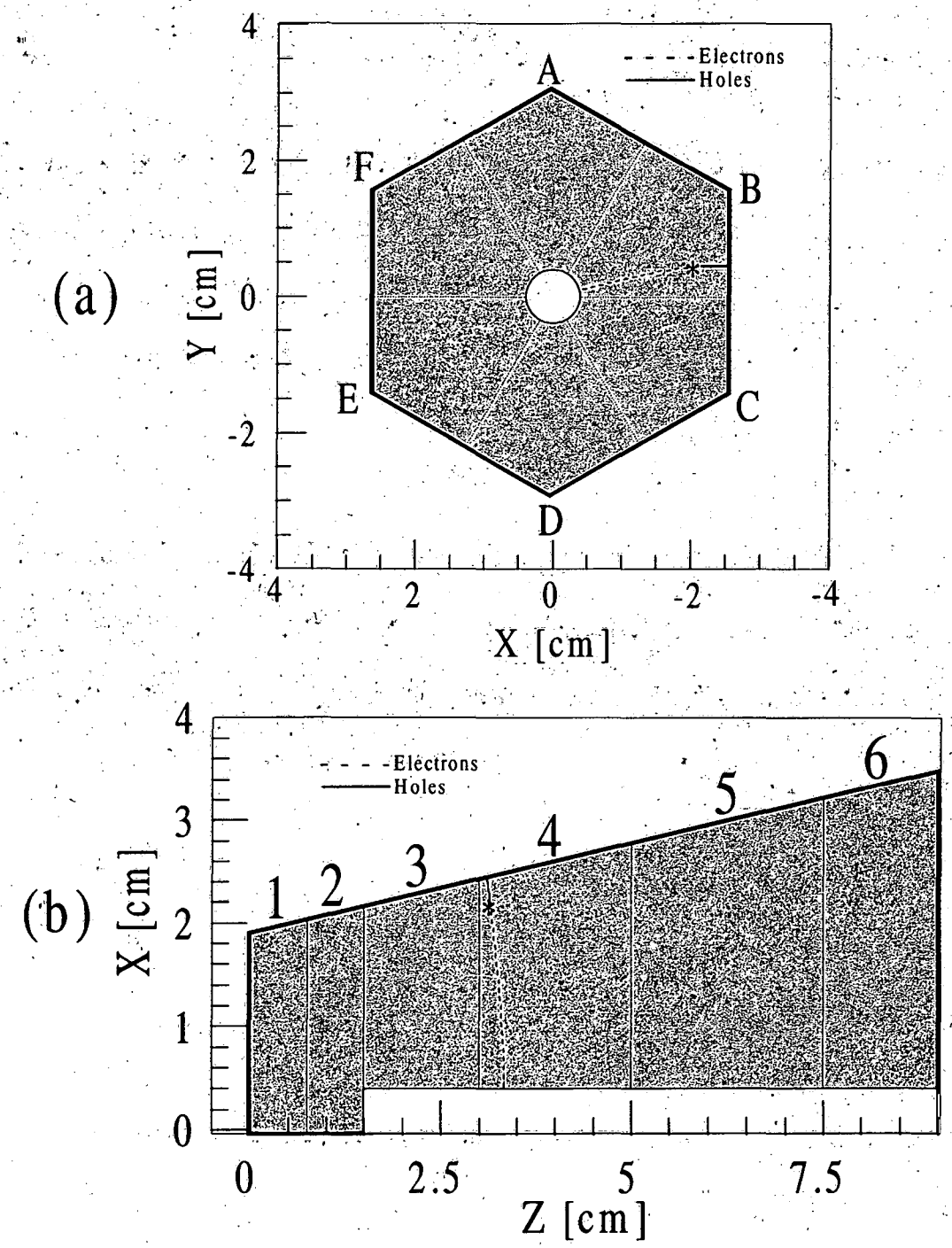

Figure 3.1: XY (a) and XZ (b) cross sections through the prototype detector illustrating the interaction location (*) and calculated drift paths for the electrons and holes. The small dashed lines (·····) show the segmentation boundaries.

Calculation of the charge induced at each of the segment electrodes requires use of a weighted potential. By employing similar finite element methods, the weighting potential for each segment electrode is obtained (a cross section of the detector crystal indicating the calculated weighting potential for one segment was shown previously in Figure 2.5). The values of the weighted electric field for each electrode are calculated and stored at the same 1 mm grid point locations. Using the previously determined drift paths for both the electrons and holes the induced charge ΔQ_j on segment electrode j is determined for time intervals Δt of 1 ns along the path such that:

$$\Delta Q_j = \frac{q_o}{V_o}\left((E_j(r_e) \bullet v_e) + (E_j(r_h) \bullet v_h)\right)\Delta t \ . \qquad (3.1)$$

Here, q_o represents the total charge produced in the interaction (normalized to 1) and $E_j(r_{e,h})$ is the weighted electric field for segment j at the location along the drift path for the electrons or holes. Figure 3.2 shows the calculated pulse shapes induced at electrodes B3, B4 and C4 for the interaction depicted in Figure 3.1. The separate contributions from the electrons and holes to the total induced charge are illustrated for electrode B4. Only the total induced charge for the transient pulse shapes in segments B3 and C4 is shown.

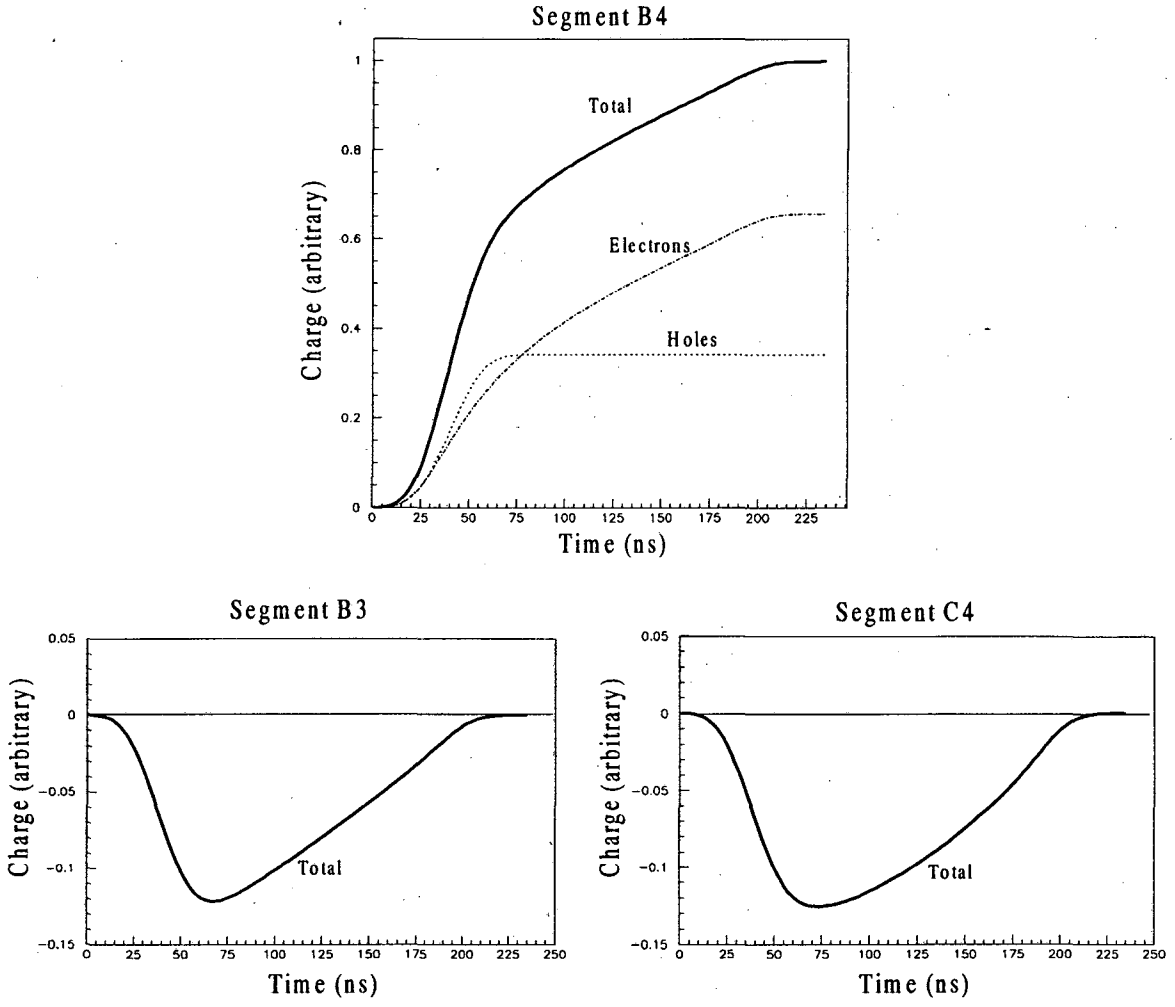

Figure 3.2: Calculated pulse shapes at electrodes B4, B3, and C3 for the interaction shown in Figure 3.1. Separate electron and hole components are illustrated for segment B4 (charge-collecting electrode).

3.2 Experimental Measurements of Pulse Shapes from Localized Single Events in the Prototype Detector

As a means of verifying the accuracy of the calculated pulse shapes described in the previous section, an experimental arrangement was designed to localize γ-ray interactions within the prototype detector. The goal was to confine energy deposition to a

small volume of the detector crystal at a known location. The resulting pulse shapes from charge collection were then digitally recorded to allow comparison to the calculated pulse shapes.

3.2.1 Experimental Arrangement and Methods

The γ-ray source utilized in the measurements was 1 mCi of ^{137}Cs (β^- decay to ^{137}Ba followed by the emission of a 661.7 keV γ ray [33]). The source was fixed in a collimated tungsten absorber such that the collimated γ rays were incident upon the front face of the detector crystal. Both a top and side view of the detector and source arrangement are illustrated in Figure 3.3. The cylindrical collimator opening in the absorber measured 1 mm in diameter and 7 cm in length. By fixing the absorber to a scanning system, its location relative to the detector in the XY plane (see Figure 3.3) could be adjust with an accuracy of $^{\pm}10^{-2}$ mm. In order to provide the necessary collimation in the Z-direction (depth into the detector crystal), three collimated NaI detectors were employed. These detectors were chosen due to their relatively large size (12.7 cm diameter and 15.2 cm length) and, therefore, large solid angle coverage around the prototype detector. Lead absorbers, each 10 cm thick, were arranged in front of each of the NaI detectors. Each of the lead absorbers had a 1 mm slit parallel to the XY plane (see Figure 3.3) providing the collimation for the NaI detectors. The NaI detectors and the lead absorbers could be raised or lowered to adjust the collimation in the Z-direction.

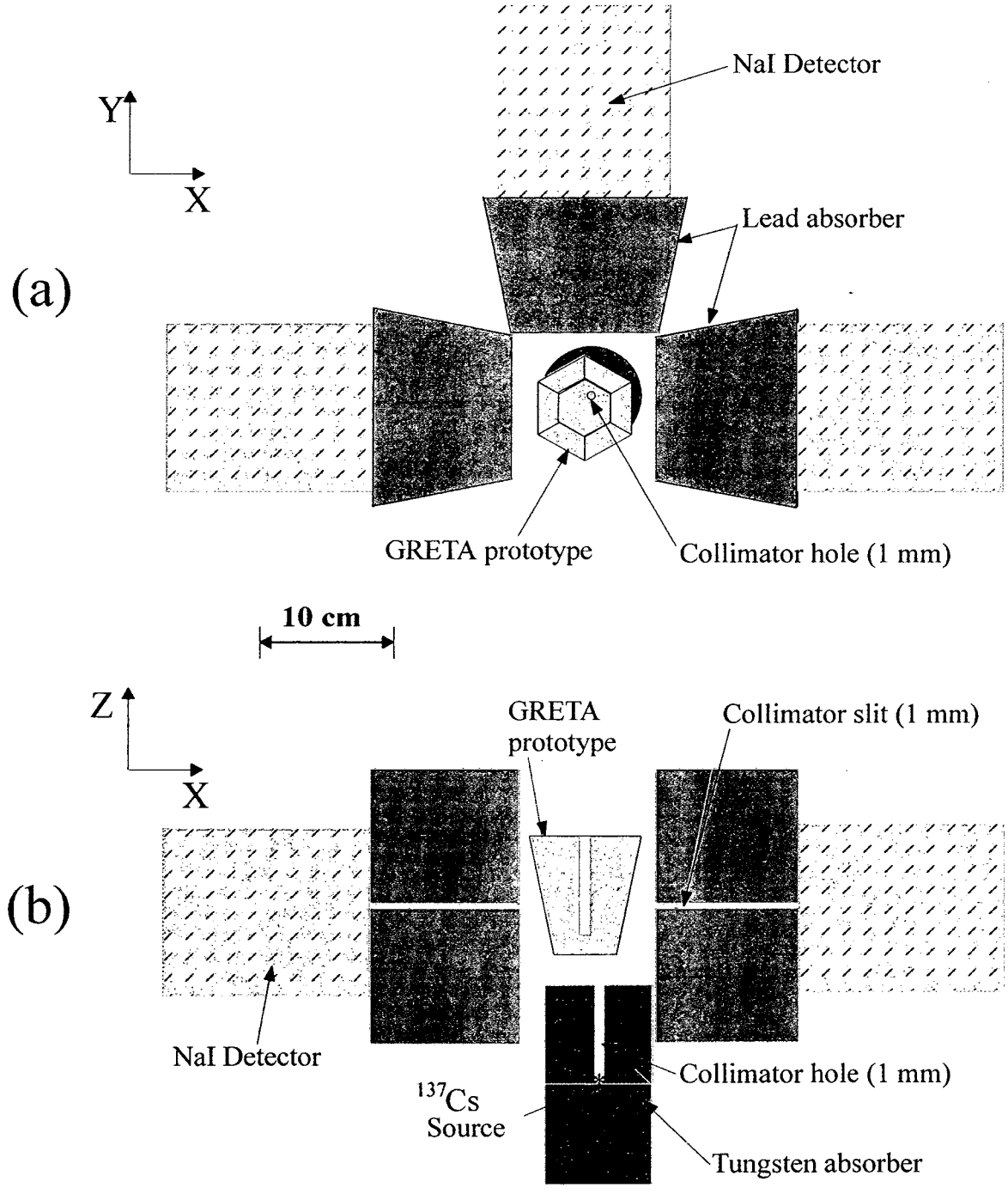

Figure 3.3: Top (a) and side (b) views of the collimation and detector arrangement employed to localized single γ-ray interactions in the prototype detector.

The locations of γ-ray interactions were fixed by selecting events with simultaneous energy deposition in both the prototype detector and one of the NaI detectors (events in "coincidence"). Because the collimation of the source and NaI detectors are at 90° to one another, such events imply the occurrence of an approximate 90° ±1° Compton scattering process in the region of the prototype detector defined by the collimation. In such a case, the incident γ ray will deposit about 374 ± 5 keV in the prototype detector. This fact is used to further aid in localization of single interactions. By selecting events with energy deposition close to 374 keV in the prototype detector, the number of events that undergo more than one Compton scattering in the prototype can be reduced.

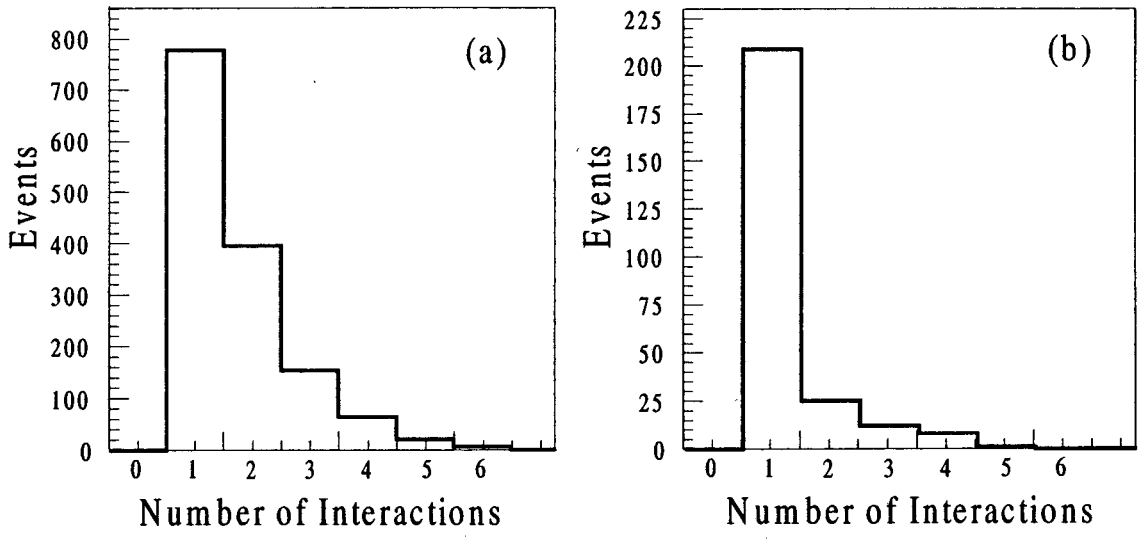

Figure 3.4: Distributions of coincident events as a function of the number of interactions in the prototype detector with (b) and without (a) requiring energy deposition of 374 ± 5 keV.

Figure 3.4 shows results of Monte Carlo simulations of the radiation transport performed with GEANT-3 [34] for the given experimental arrangement. The figure illustrates the distribution of coincident events as a function of the number of interactions of the incident γ ray, both with and without requiring energy deposition of 374 ± 5 keV in the prototype. Without the energy requirement, only about 55% of the coincident events are the result of a single interaction in the detector. However, with the energy requirement, approximately 85% of the events are the result of a single interaction. The distributions of interaction locations in the X- and Z-direction, also obtained from the simulation, are shown in Figure 3.5. The distribution in the Y-direction is very similar to that of the X-direction, both being dictated by the cylindrical collimation of the source. Due to the very small opening angles, the arrangement defines a nearly cylindrical volume in the prototype detector for single interactions with a diameter of about 1.5 mm (in XY plane) and depth of about 1.9 mm (in Z-direction), both measured as the full-width at half-maximum.

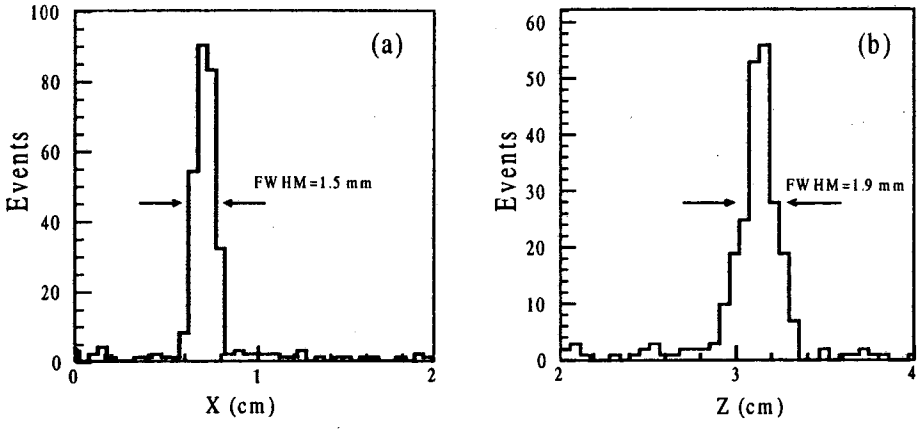

Figure 3.5: Monte Carlo simulations showing distributions of interaction locations in the X-direction (a) and Z-direction (b). The full-width at half-maximum obtained by fitting the distributions with a Gaussian is indicated for each.

In order to define the X- and Y-locations of the source relative to the detector, the scanning system was utilized. The source was moved in 1 mm increments along the X- and Y-directions. The intensity of the 661.7 keV γ ray was measured in each of the segments for fixed time intervals at each location. Plotting the intensity in each segment as a function of source position allowed the transitions in intensity between segments to be determined and thus the location of the segment boundaries to be estimated. Figure 3.6 shows measured intensity distributions for the first and third layer of segments (A1, B1, C1 and A3, B3, C3) and the estimated segment boundaries.

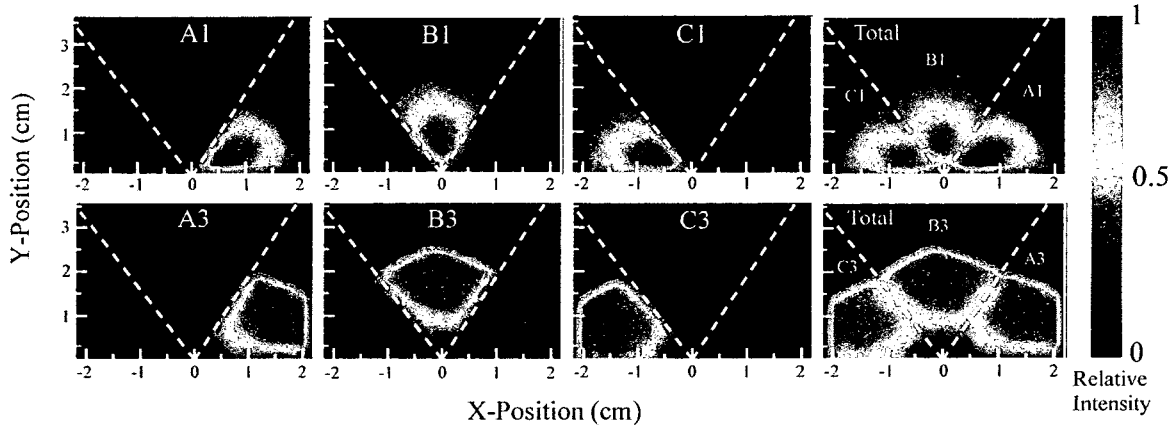

Figure 3.6: Experimentally measured intensity distributions in the XY plane from the collimated ^{137}Cs γ-ray source. The dashed lines indicate the estimated segment boundary locations.

To determine the alignment in the Z-direction between the collimated NaI detectors and the prototype detector a separate ^{241}Am source (E_γ = 59.54 keV) was employed. This source was positioned behind the 1 mm slit in the lead absorber such that the γ rays incident upon the prototype detector were collimated in the Z-direction. By

translating the lead absorber and source along the Z-direction in 1 mm increments and measuring the transition in intensities between segments, just as in the X- and Y-alignment, the segment boundaries in the Z-direction (i.e. B1, B2, B3, ect.) could be estimated.

After defining the alignment of the collimator-detector arrangement, the ^{241}Am source was removed and pulse shapes from the coincident events of the ^{137}Cs source (including the energy requirement in the prototype detector) were measured at various locations in the detector. Because the event rates were small, in some cases less than 1 event per hour, a limited number of positions in segments B1, B2, and B4 were chosen. Locations resulting in charge collection in segments B1 and B2 (smaller front segments) and B4 (larger middle segment) provided a good variety of pulse shapes for comparison with model predictions. Pulse shapes from a total of 91 locations (36 in segment B4 and 55 in segments B1 and B2) were measured. Locations were separated by 4 mm in the X-direction and 3 mm in both the Y- and Z-directions. Figure 3.7 illustrates the relative locations of the interaction sites in the detector. On average, events were acquired at each location for a period of one day. The number of events measured at each location ranged from about 10 to 200, dependent upon the location in the detector crystal. Locations toward the inside of the crystal (i.e. smaller X and/or larger Z) resulted in fewer measured events. At each location the pulse shapes from the segment collecting the charge as well as the eight nearest neighboring segments (i.e. for an interaction in B1; A1-3, B2-3, and C1-3) were digitally recorded using an 8 bit flash analog to digital converter (ADC) operating at a sampling rate of 500 Mhz. The ADC digitized the voltage from each of the nine segments every 2 ns.

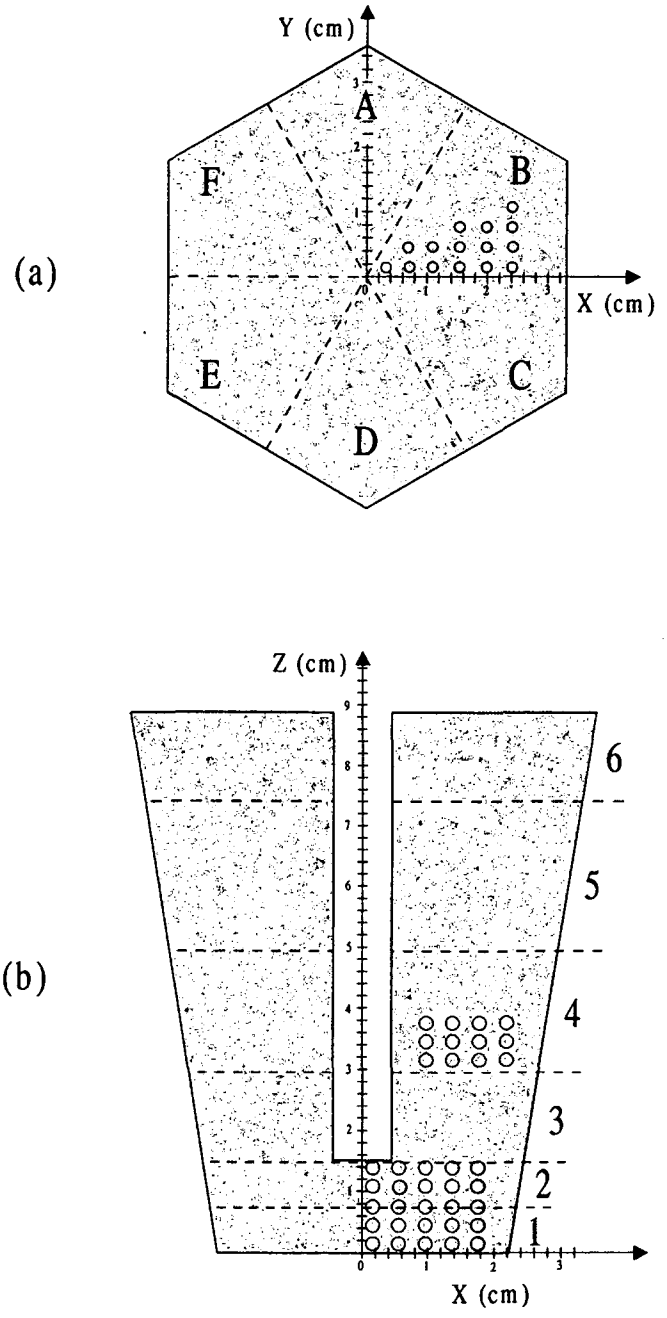

Figure 3.7: Cross sections of the detector crystal in the XY (a) and XZ (b) planes illustrating the locations where pulse shapes were measured (open circles). The size of the circles represent the approximate volume defined by the collimating system and the dashed lines show the segment boundaries.

3.2.2 Experimental Results and Comparisons with Model Predictions

In order to illustrate the experimental data and the relative quality of the calculated pulse shapes, a select group out of the 91 measured data sets is presented in this section. This group is representative of the overall quality of the comparison between experiment and model calculations for all the positions and the subsequent discussion of factors effecting their agreement applies to γ-ray interactions throughout the detector volume. Figure 3.8 shows a set of six experimentally measured pulse shapes (solid traces) and the calculated pulse shape (dashed trace) at the position X = 18, Y = 1.5, and Z = 1 mm for segment B1 (charge-collecting electrode) and the eight neighboring electrodes. Note that the position is given as the centroid of the collimated volume for the experimental pulse shapes (see Figure 3.7). Additionally, the charge amplitudes are given relative to a pulse height in segment B1 (normalized to 100) and the scale is much increased for the neighboring segments. In general, the calculated pulse shapes from each segment closely represent the pulse shapes experimentally measured. As an example of the effect that location has on the pulse shapes, Figure 3.9 shows a set of six measured pulse shapes and the calculated pulse shape for the position of X = 6, Y = 1.5, Z = 1 mm using the same format as in Figure 3.8. Because this position is much closer to the central electrode and thus the charge carriers experience higher electric fields over short distances, the pulse shape seen at electrode B1 rises much faster than that shown in Figure 3.8. This feature is also present in the model and suggests that the electric fields and charge carrier drift contained in the model are reasonable. The discrepancies between the experimental data and model calculations, seen mostly in the neighboring segments, will be discussed later in this section.

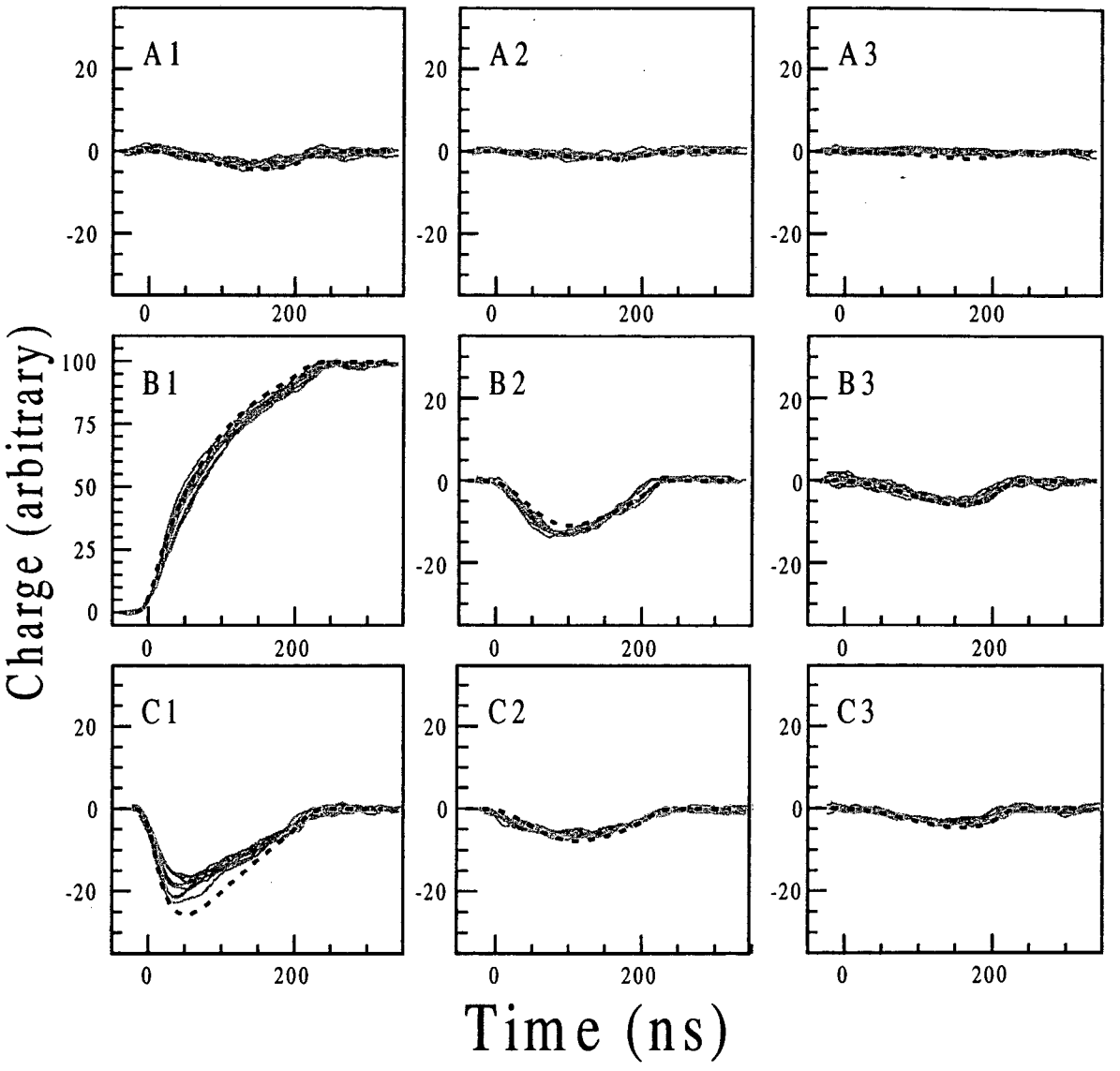

Figure 3.8: Six measured (solid traces) pulse shapes and the corresponding calculated (dashed trace) pulse shape at a position of X=18, Y=1.5, and Z=1 mm for segments A1-3, B1-3, and C1-3. The largest discrepancies are seen in segments B1, B2, and C1.

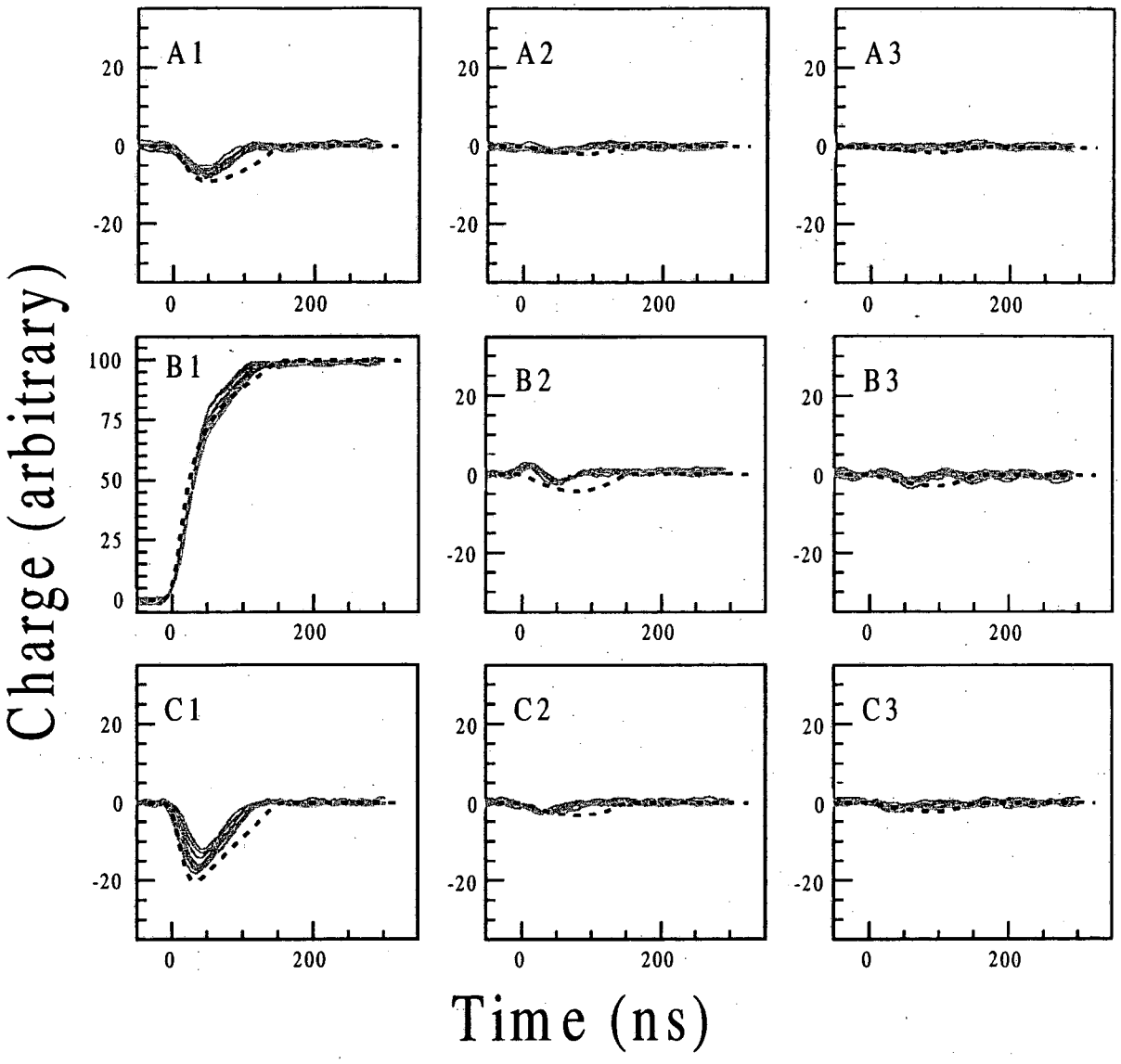

Figure 3.9: Six measured (solid traces) pulse shapes and the corresponding calculated (dashed trace) pulse shape at a position of X=6, Y=1.5, and Z=1 mm for segments A1-3, B1-3, and C1-3. Significant discrepancies are seen in segments A1, B1-2, and C1-2.

To illustrate the comparison between the calculations and experiment in the larger segment B4, Figure 3.10 shows both calculated and experimentally measured pulse shapes from the location of X = 22, Y = 4.5, and Z = 34.5 mm. Again, pulse shapes from the eight neighboring segments in addition to the charge-collecting segment (e.g. B4) are shown. The interaction in this case takes place close to segments C4 and B3. This means

that the values of the weighted electric fields for these segments, over the drift path of the charge carriers, were larger than in the other neighboring segments and thus resulted in pulses with larger absolute amplitudes.

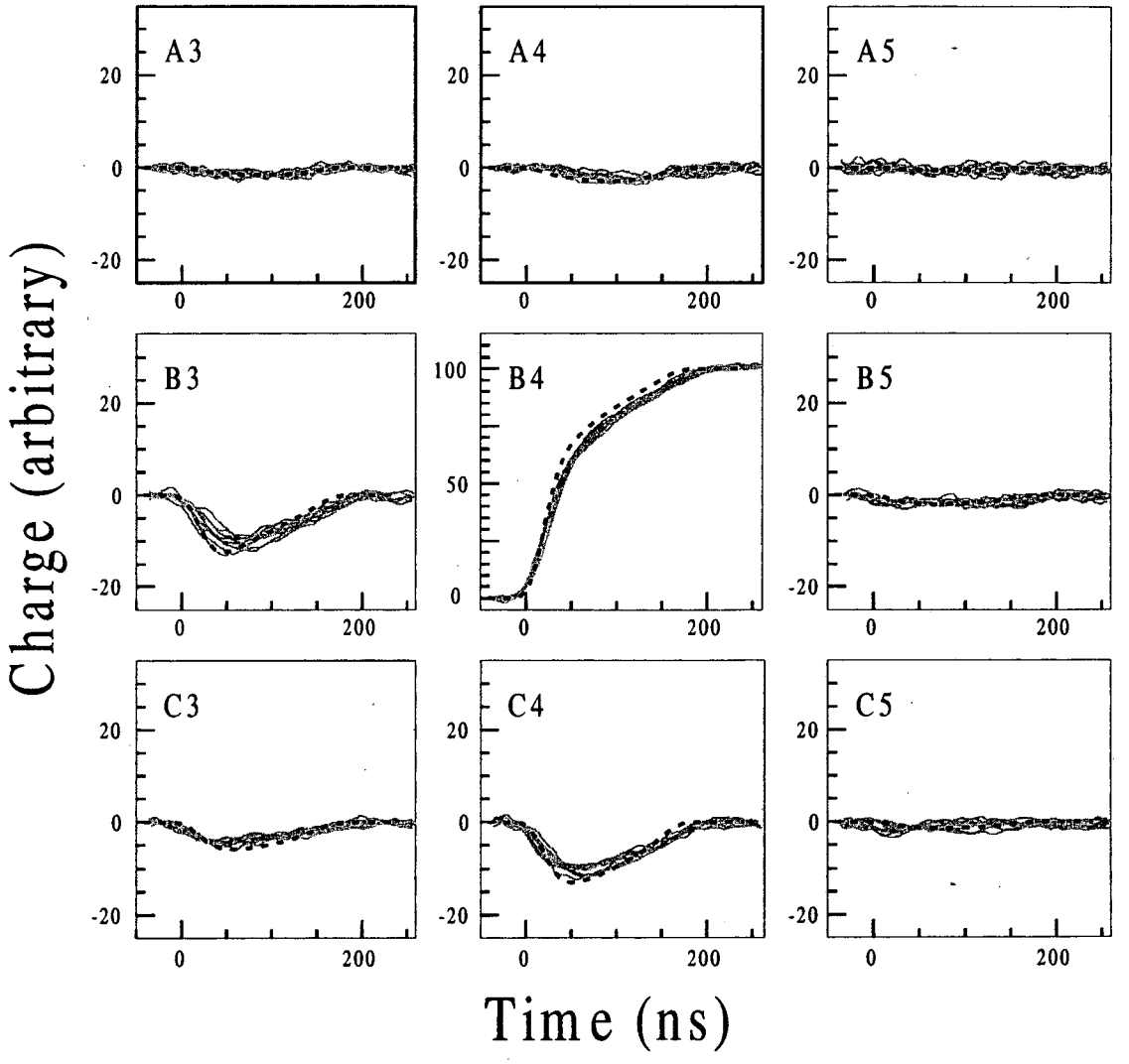

Figure 3.10: Six measured (solid traces) pulse shapes and the corresponding calculated (dashed trace) pulse shape at a position of X=22, Y=4.5, and Z=34.5 mm for segments A3-5, B3-5, and C3-5. The largest discrepancies are seen in segments B3, B4, and C4.

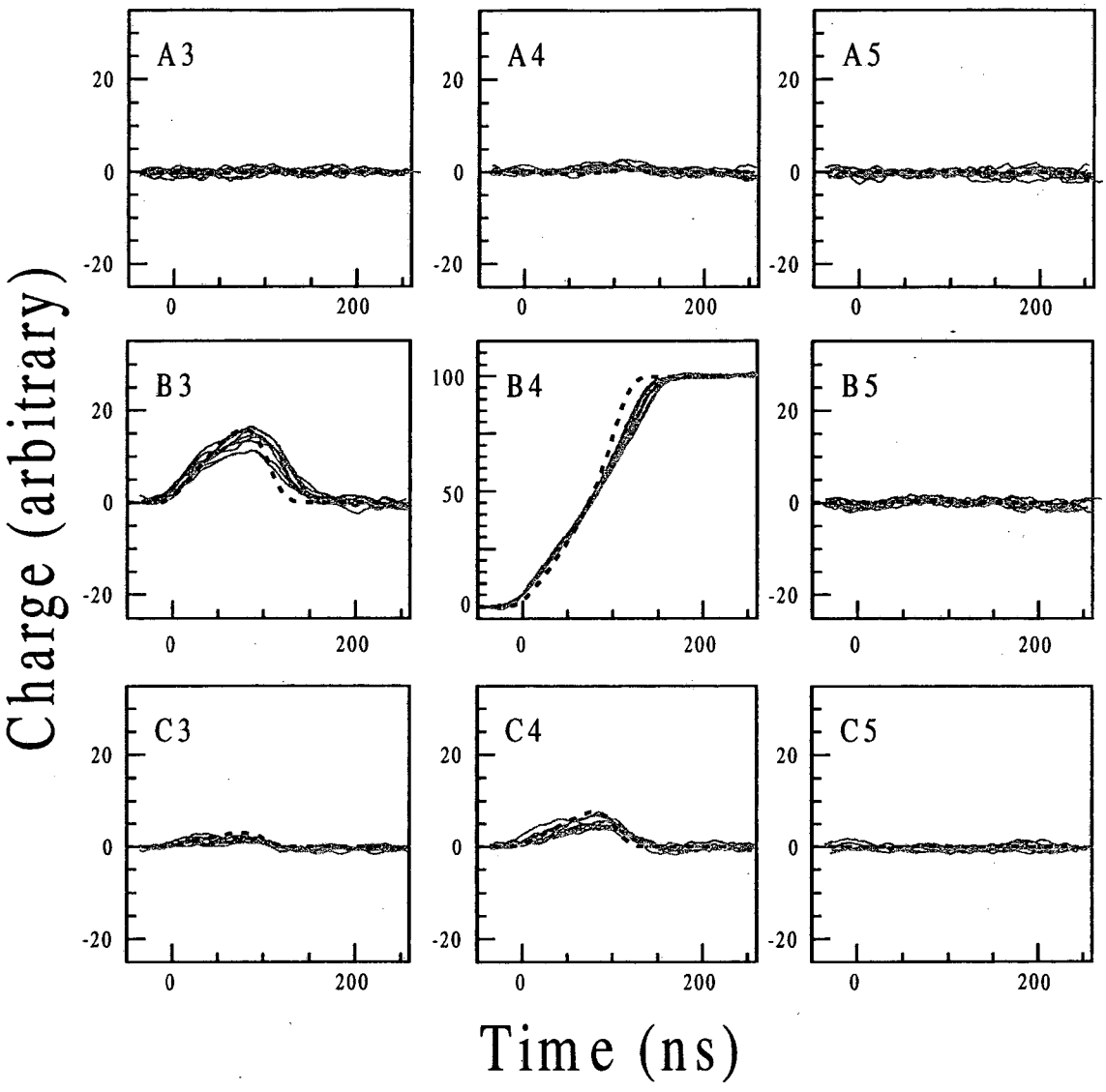

Figure 3.11: Six measured (solid traces) pulse shapes and the corresponding calculated (dashed trace) pulse shape at a position of X=14, Y=4.5, and Z=34.5 mm for segments A3-5, B3-5, and C3-5. The largest discrepancy is seen in segment B4.

To examine a change in position within segment B4, Figure 3.11 shows calculated and experimental pulse shapes at the location of X = 14, Y = 4.5, and Z = 34.5 mm. Again, the interaction takes place close to segments C4 and B3, thus, the resulting pulse shapes have the largest amplitudes in these segments. However, the polarity of the pulses

has changed relative to those seen in Figure 3.10. This stems from the fact that the interaction is now closer to the central electrode and the individual contributions to the induced charge from the drift of the electrons and holes has changed. To illustrate this in detail, Figure 3.12a shows the weighted potential for segment C4 in a portion of a cross section through the XY plane in segments B4 and C4. Overlaid on the figure is the interaction location (★) of X = 22, Y = 4.5, and Z = 34.5 mm (pulse shapes in Figure 3.10), the drift path marked by the dashed line to the left and right for the electrons and holes, respectively, and the weighted electric field vector (E_w) for segment C4 at several locations along the drift path. In the early stages of the charge carrier drift, close to the interaction, the angle between the electron drift velocity and E_w is greater than 90° and the angle between the hole drift velocity and E_w is less than 90°. This results in an initial negative induced charge contribution from both the electrons and holes. Figure 3.12b shows the separate contributions of the electrons and holes to the charge induced at segment C4 as well as the total. In the early stages of pulse development (times less than ~75 ns) the induced charge from both the electrons and holes are negative. At later times, the holes have reached the B4 electrode (i.e. $\Delta Q_{holes} = 0$) and the angle between the electron drift velocity and E_w is now less than 90° (i.e. $\Delta Q_{electrons}$ is positive). The electrons continue to drift until reaching the central electrode at which point their positive contribution to the total induce charge at C4 results in a total charge of zero.

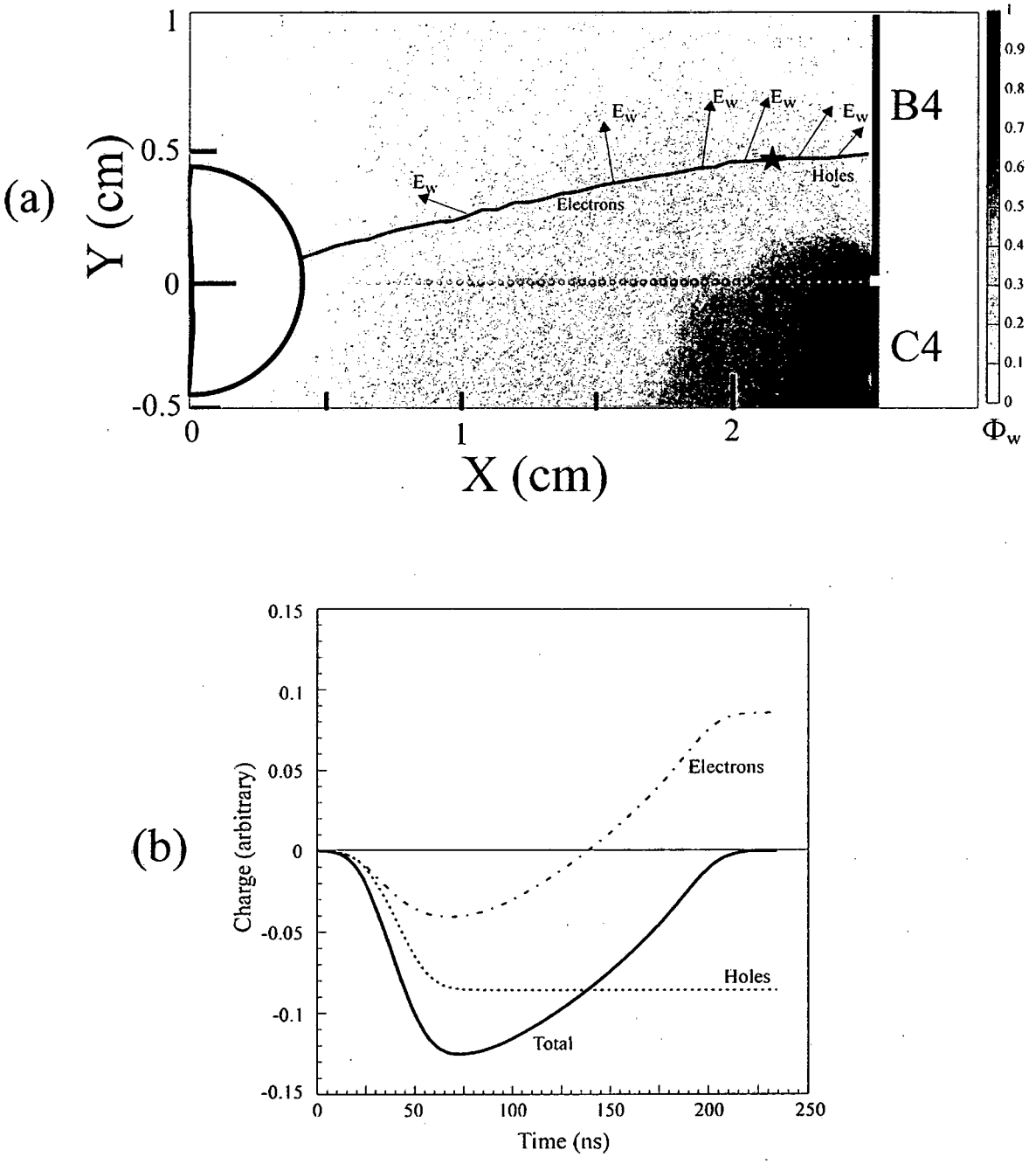

Figure 3.12: (a) XY cross section through a portion of the detector crystal showing the weighted potential (Φ_w) for segment C4 and the drift path of the electrons and holes for an interaction location of X=22, Y=4.5 and Z=34.5 mm. The weighted electric field vector (E_w) for segment C4 is shown at several locations along the drift path. The white dashed line indicates the boundary between segment B4 (charge-collecting electrode) and segment C4. The calculated pulse shape for segment C4 with separate electron and hole contributions is shown in (b).

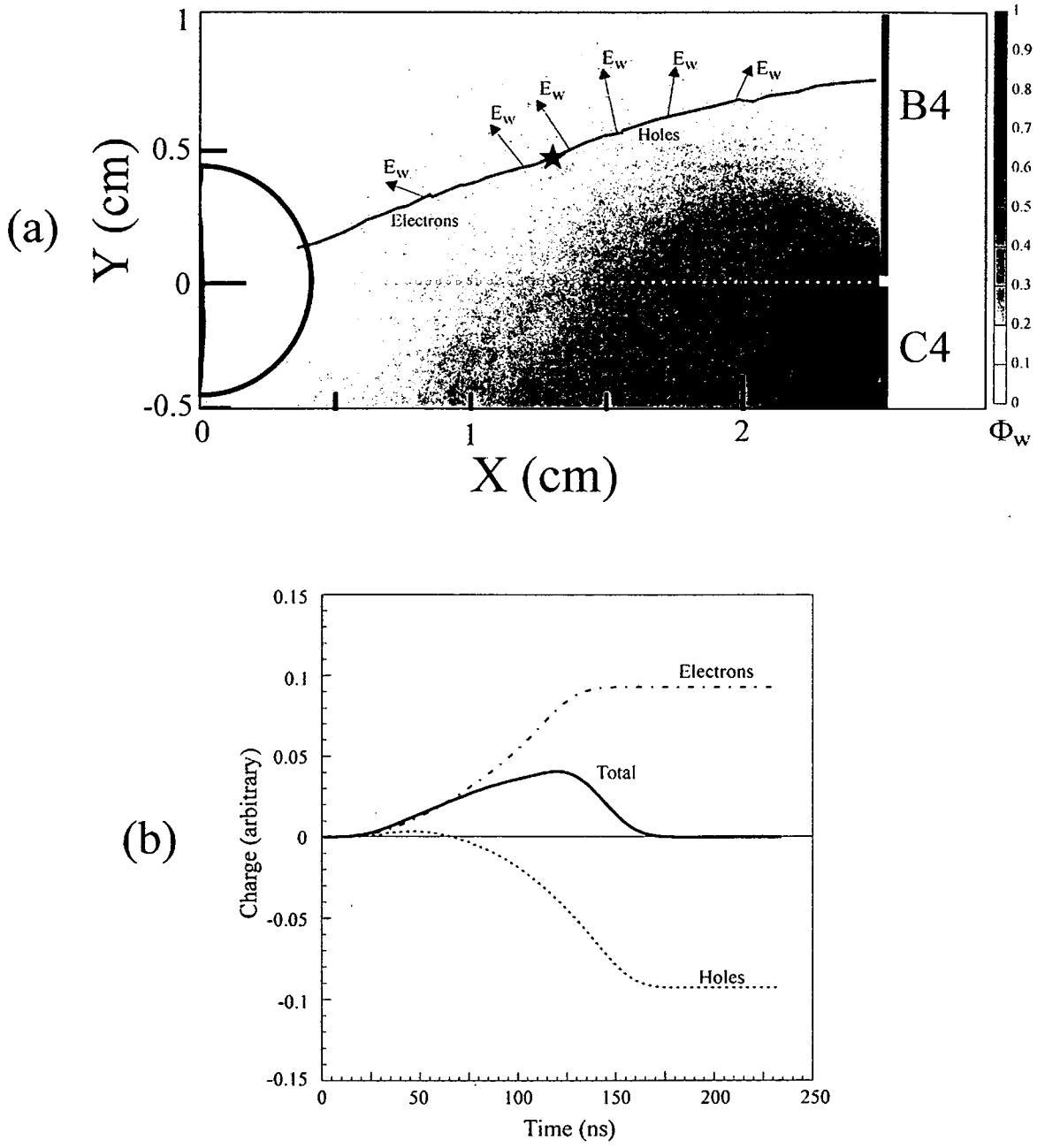

Figure 3.13: (a) XY cross section through a portion of the detector crystal showing the weighted potential (Φ_w) for segment C4 and the drift path of the electrons and holes for an interaction location of X=14, Y=4.5 and Z=34.5 mm. The weighted electric field vector (E_w) for segment C4 is shown at several locations along the drift path. The white dashed line indicates the boundary between segment B4 (charge-collecting electrode) and segment C4. The calculated pulse shape for segment C4 with separate electron and hole contributions is shown in (b).

To illustrate the polarity change of the pulse shape at electrode C4, Figure 3.13a and b is the same as Figure 3.12 but for the interaction location X = 14, Y = 4.5, and Z = 34.5 mm (pulse shapes in Figure 3.11). In this case, the angle between the hole drift velocity and E_w is initially greater than 90° and that of the electron drift velocity and E_w is less than 90°, thus, contributing to a positive induced charge at C4. The positive contribution of the electrons to the induced charge is dominant until their collection at which point the negative contribution of the holes to the induced charge returns the total induced charge to zero. This results in a positive maximum in the pulse shape. A similar example can be illustrated in the Z-direction for the induced pulse shapes induced at electrode B3. In both cases, these features are well reproduced in the model, again, suggesting reasonable representation of weighted electric fields and charge carrier transport in the modeling.

3.2.3 Discussion

In general, the calculated and experimentally measured pulse shapes from the select regions investigated are in good agreement. There are, however, significant deviations between the two in some cases. This section will provide a general discussion of the factors effecting the ability of the model to accurately represent experimentally measured pulse shapes. The focus will be on factors related to the modeling process itself rather than those of the experimental arrangement. Factors inherent to the modeling process are of much more fundamental importance than those specifically related to the experimental arrangement used for the current measurements (i.e. the overall alignment of the collimation system on the order of 1 mm and the finite volume allowed for

interactions ~3 mm^3). Experimental conditions can be changed to provide greater accuracy in confining the position of a single interaction. However, improvement in the modeling requires the understanding and incorporation of additional physical phenomena, which may not be so straightforward. This may pose a limit on the ability of the model to reproduce experimental measurements and ultimately may translate into limitations on the position resolution that can be achieved (see Section 3.3.3). Here, the discussion is limited to modeling of pulse shapes.

Factors effecting the agreement between the modeled and experimentally measured data can be separated into two general classes. The first class contains those factors involved in signal generation (i.e. charge-carrier generation and collection). The second class contains factors that define the electric fields in the detector, including impurity concentrations and electrode surfaces.

The signal generation process incorporated in the model is rather simple. Energy deposition and charge carrier production is assumed to take place at a single point. In reality, these processes occur over a finite range. As discussed in Section 2.2.3, the primary electron transfers its energy primarily through direct and indirect ionization and other excitations in the germanium crystal. In addition, the trajectory of the electron is not linear [35]. This results in three-dimensional spatial distributions of charge that vary from interaction to interaction for the same total energy deposited. Thus, for example, the actual pulse shapes generated by a 1 MeV primary electron will produce a distribution of tracks with sizes on the order of 1 mm^3 [36]. Furthermore, as the charge carriers drift, diffusion will lead to additional spreading of the distribution. However, this effect is small relative to the initial size of the distribution. The spreading for both electron and

hole distributions has been shown to be approximately 65 μm/cm of drift distance in germanium [37]. Additionally, the charge carrier drift velocities depend on the electric field strength, temperature, and crystal orientation relative to the drift direction and the effects of the later two have not been included in the present model.

The electronic characterization of the detector crystal also plays an important role in modeling pulse shapes. As stated in Section 3.1, the model uses an approximation for the distribution of impurities throughout the detector crystal that varies linearly in the Z-direction. However, variations in the impurity concentration can distort the local electric fields [38,39]. These fluctuations in electric field values can alter the drift paths of the charge carriers and ultimately change the pulse shape compared to that predicted with uniform impurity concentrations. Additionally, the model assumes that the passivated back face and surfaces between adjacent electrodes are perfect surfaces. In this way, Neumann boundary conditions are used in the solution of the electric fields (i.e. $\delta\Phi/\delta r = 0$ at the surfaces). However, the true characterization of these surfaces is not well known, and thus they may have an effect on the local electric fields and resulting pulse shapes. Each of these factors lead to uncertainties in the modeling process and may ultimately contribute to discrepancies between the calculated and experimental pulse shapes.

3.3 Position Sensitivity

As discussed in Chapter 2, the changes in the detailed signal shapes from the detector is the fundamental means by which one can resolve interaction locations to better than the segmentation size. A rough feel for the sensitivity of pulse shapes to the change in interaction location can be seen from the results shown in Figures 3.10 and 3.11 where a change in location of 8 mm in the X-direction produced a change in polarity of the induced pulse shapes at electrodes C4 and B3.

As will be derived here, the position sensitivity relates the difference between pulse shapes, as a function of γ-ray interaction location, to the signal uncertainty due to noise. This relationship will be used to approximate the dimension at which changes in pulse shape becomes distinguishable over noise. The sensitivity will be examined as a function of segment size, location within each segment, and directionally (i.e. changes in X, Y, and Z). In Section 3.3.1, position sensitivity is derived and examined for single γ-ray interactions at locations throughout the detector. For such an extensive examination, calculated pulse shapes are utilized. However, as a means of justifying such an approach, position sensitivities derived from experimentally measured pulse shapes are shown and compared to those obtained from the model calculations. In Section 3.3.2, the process is extended to examine two interactions occurring in a single segment.

It is important to stress the use of the term position sensitivity rather than position resolution. Position resolution implies that the absolute position of one or more interactions can be determined to a given accuracy. Position sensitivity, however, only quantifies the point at which differences in pulse shapes become distinguishable over the

noise. Many of the factors discussed in the previous section, such as the finite range of the primary electron, have an impact on and may be limiting factors in the position resolution that can be achieved. An important factor, which will be addressed by examining the position sensitivity, is the geometry and segmentation size of the detector electrodes.

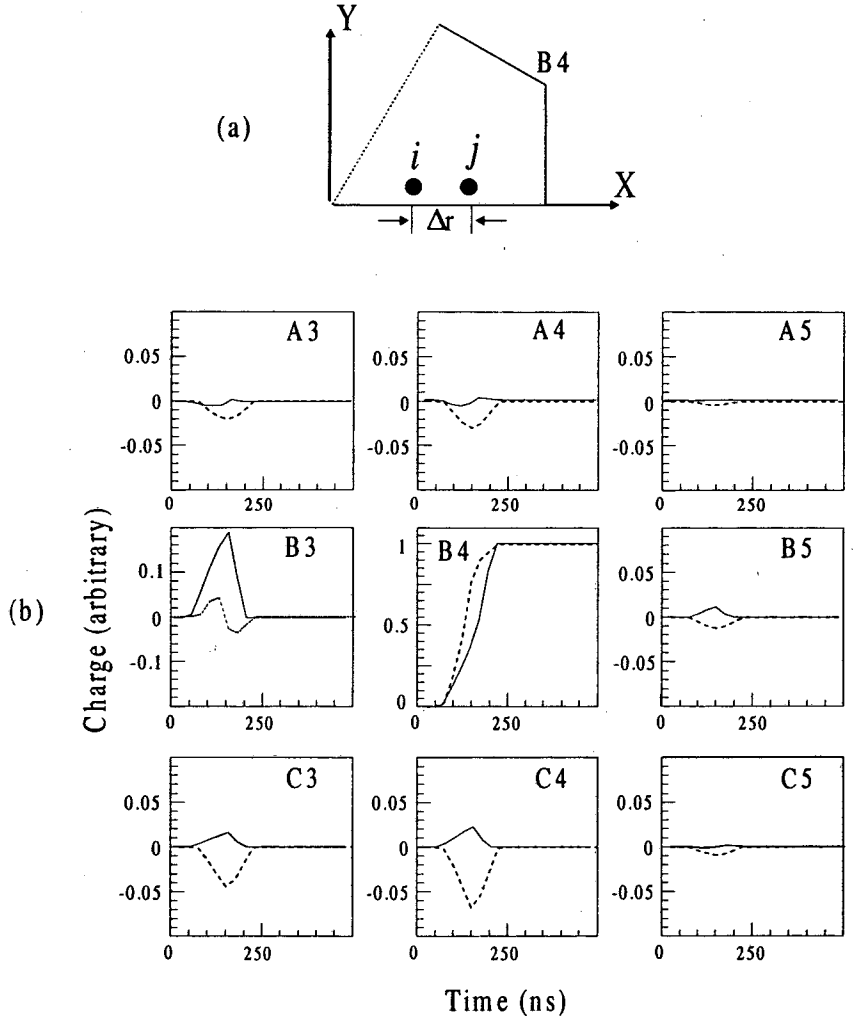

Figure 3.14: (a) Positions *i* and *j* separated by Δr = 2 mm shown in a XY cross section of segment B4. (b) Calculated pulse shapes for an interaction at *i* (solid trace) and *j* (dashed trace) in segments A3-5, B3-5, and C3-5.

3.3.1 Single-Interaction Position Sensitivity

The modeled pulse shapes provide an excellent means for deriving position sensitivity because they have no statistical fluctuations (i.e. noise). Therefore, differences in their shape can be derived solely on the basis of a change in interaction position. To illustrate this, Figure 3.14a shows a cross section through the detector and two positions labeled *i* and *j* separated by a distance of $\Delta r = 2$ mm. Figure 3.14b shows the calculated pulse shapes, in nine neighboring segments, resulting from separate interactions occurring at positions *i* and *j*. In order to distinguish a single interaction occurring at position *i* from one at *j* the overall difference in signal shape (i.e. amplitude differences, $q_i(t)$-$q_j(t)$) must be greater than that caused by the random fluctuations or the noise level σ_n that would be present in experimentally measured pulse shapes. It is important to point out that σ_n, as discussed here, reflects not only statistical fluctuations in the signal generation process itself (i.e. those intrinsic to the detector crystal) but also electronic noise from the amplification and digitization of the pulse shapes. The difference in induced charge as a function of time for the pulse shapes illustrated in Figure 3.14b is shown in Figure 3.15. In order to relate the pulse shape difference to the noise, the quantity χ_{ij} is defined as:

$$\chi_{ij}^2 = \sum_{m=1}^{36} \left[\frac{\int_0^{t_c} \left(q_i^m(t) - q_j^m(t) \right) dt}{\sqrt{2}\sigma_n} \right]^2, \qquad (3.2)$$

where $q_i^m(t)$ and $q_j^m(t)$ are the induce charges at electrode m for a single interaction occurring at position i and j, respectively. For practical purposes, the integral in Equation 3.2 is evaluated at fixed time intervals, Δt = 2 ns, because in both the calculated and experimentally measured pulse shapes presented in the previous sections the induced charge is recorded every 2 ns. It is assumed that the noise level is not position dependent (i.e. $\sigma_i=\sigma_j=\sigma_n$). Therefore, comparing the two pulse shapes at i and j yields a total noise contribution of $\sqrt{2}\,\sigma_n$. Both $q(t)$ and σ_n are in units of potential and thus χ_{ij} is dimensionless. It is important to note that χ_{ij}^2 has a form very similar to a merit function used in general least squares minimization [40], which is utilized in the signal decomposition process described in Chapter 4. Given χ_{ij}, the position sensitivity S_{ij} is defined as:

$$S_{ij} = \frac{\Delta r_{ij}}{\chi_{ij}}. \tag{3.3}$$

This relationship can be used to approximate the dimension at which the change in pulse becomes distinguishable above the noise. As an example, for a given Δr_{ij}, if χ_{ij} =1 then the difference between the two pulse shapes is exactly the same level as the total noise contribution. This results in $S_{ij} = \Delta r_{ij}$ indicating that in the region around i and j pulse shapes from single interactions become distinguishable from one another at the dimension given by Δr_{ij}. However, if χ_{ij} is less than 1 (i.e. the noise level is larger than the pulse shape difference for the given Δr_{ij}) the resulting S_{ij} will be greater than Δr_{ij}. For instance, if the noise level is twice that of the pulse shape difference (i.e. χ_{ij} = 0.5) the

resulting S_{ij} will be twice the dimension of Δr_{ij}. Assuming the change in pulse shape is proportional to the separation distance, the S_{ij} of $2\Delta r_{ij}$ represents the dimension by which i and j would have to be separated to be distinguishable from one another. The opposite is true for a χ_{ij} greater than 1 and the resulting S_{ij} would be less than Δr_{ij}. In the case illustrated in Figure 3.14a, positions i and j are separated in the X-direction. However, this calculation can be performed in each of the coordinate directions yielding separate position sensitivities in each direction (e.g. S_x, S_y, and S_z).

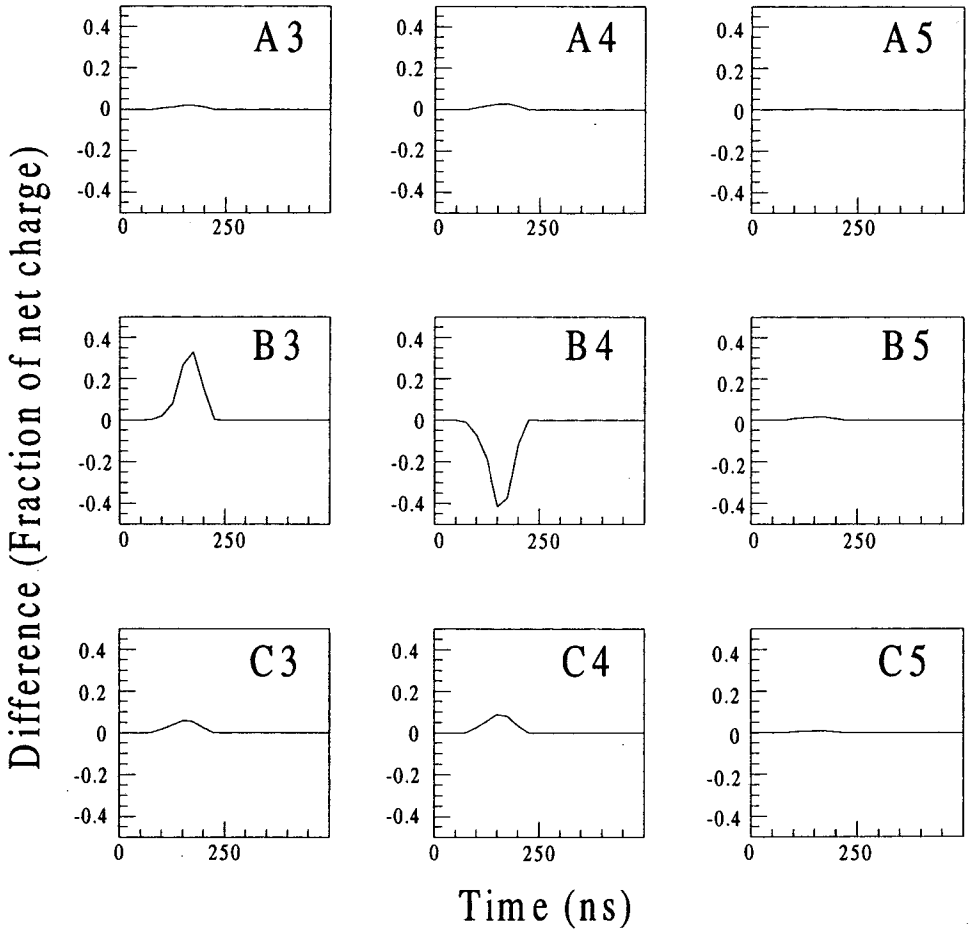

Figure 3.15: Difference, as a fraction of the net charge in segment B4, between pulse shapes i and j shown in Figure 3.14.

In order to examine the position sensitivity in each of the prototype detector segments pulse shapes were generated at locations separated by 1 mm in each coordinate direction throughout the volume of the detector crystal. Using pulse shapes from neighboring locations yields a Δr_{ij} = 1 mm in each coordinate direction. A σ_n of 5 keV was used in accordance with the results reported in reference [41]. The energy deposited at each location was chosen to be 662 keV. At each location in the detector, the position sensitivity was calculated in accordance with Equations 3.2 and 3.3 for each coordinate direction. The total sensitivity S_T for each position was then defined as:

$$S_T = \sqrt{\frac{S_x^{\,2} + S_y^{\,2} + S_z^{\,2}}{3}}. \tag{3.4}$$

By grouping positions according to the segment in which the interaction occurred, distributions of sensitivity values were generated.

Figure 3.16a and b show the distributions of calculated sensitivities, in each direction, for positions in segments 1-6 (no letter is used due to the symmetry of the segments). The mean $\overline{S}_T$ and RMS deviation $< S_T^{\,2} >^{1/2}$ are indicated for each distribution. There are several noteworthy features illustrated by the distributions. Foremost, all the mean sensitivity values are less than the Δr_{ij} value of 1 mm. This indicates that the change in pulse shape throughout the majority of the detector is larger than the noise for energy deposition of 662 keV. Secondly, the mean value of S_z in segments 2-5 increases with segment size. This is due to the fact that in larger segments there is greater separation between neighboring segments in the Z direction. As

described in Chapter 2, the symmetry of the pulse shape in the Z direction is broken by the induced signals on the neighboring electrodes. The greater the distance of an interaction from these electrodes the smaller the induced signals and thus χ is decreased and S_z increased.

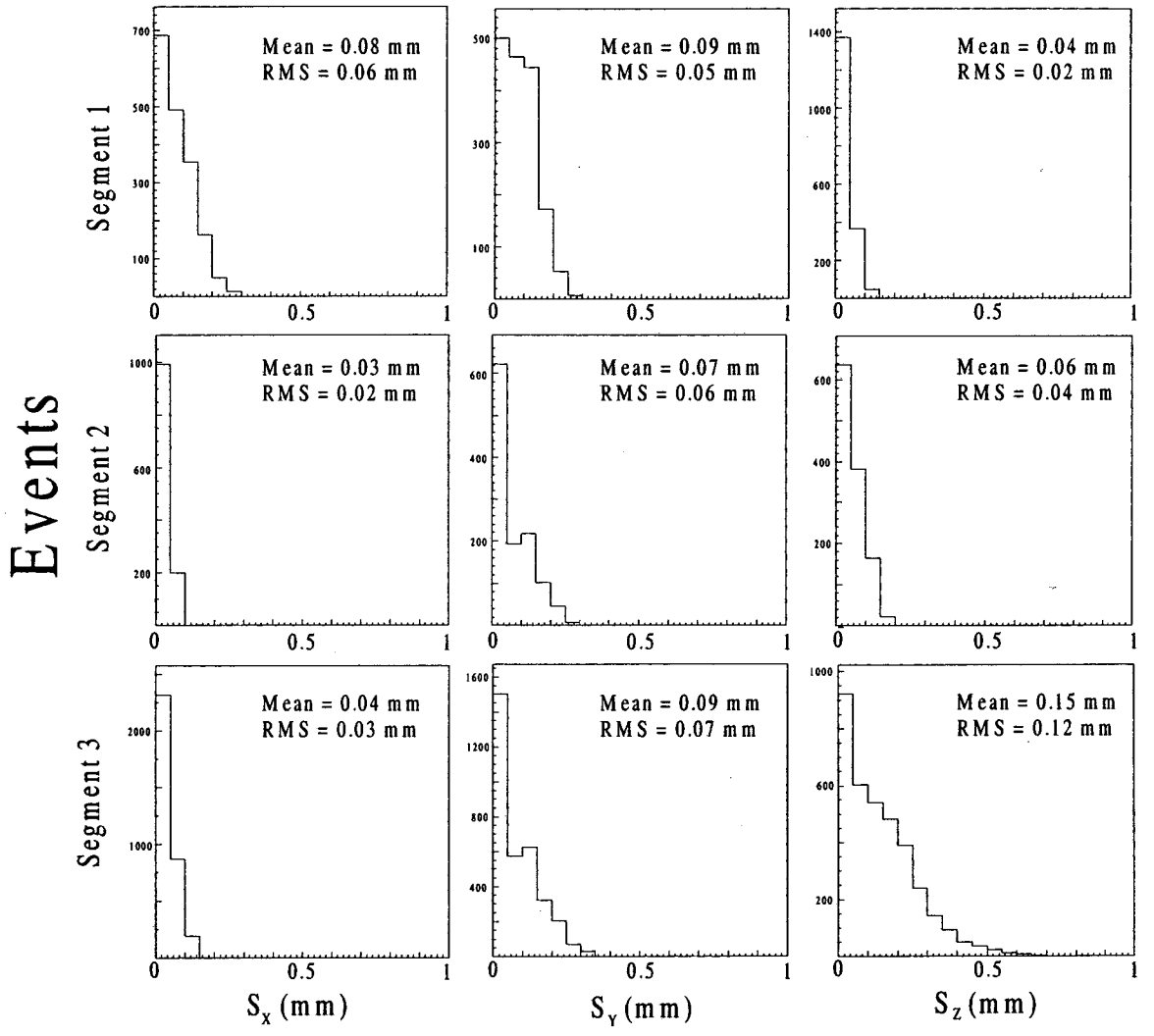

Figure 3.16a: Distributions of the single-interaction sensitivities in the X-, Y-, and Z-directions for energy deposition of 662 keV for segments 1-3. The mean and RMS values are given for each distribution.

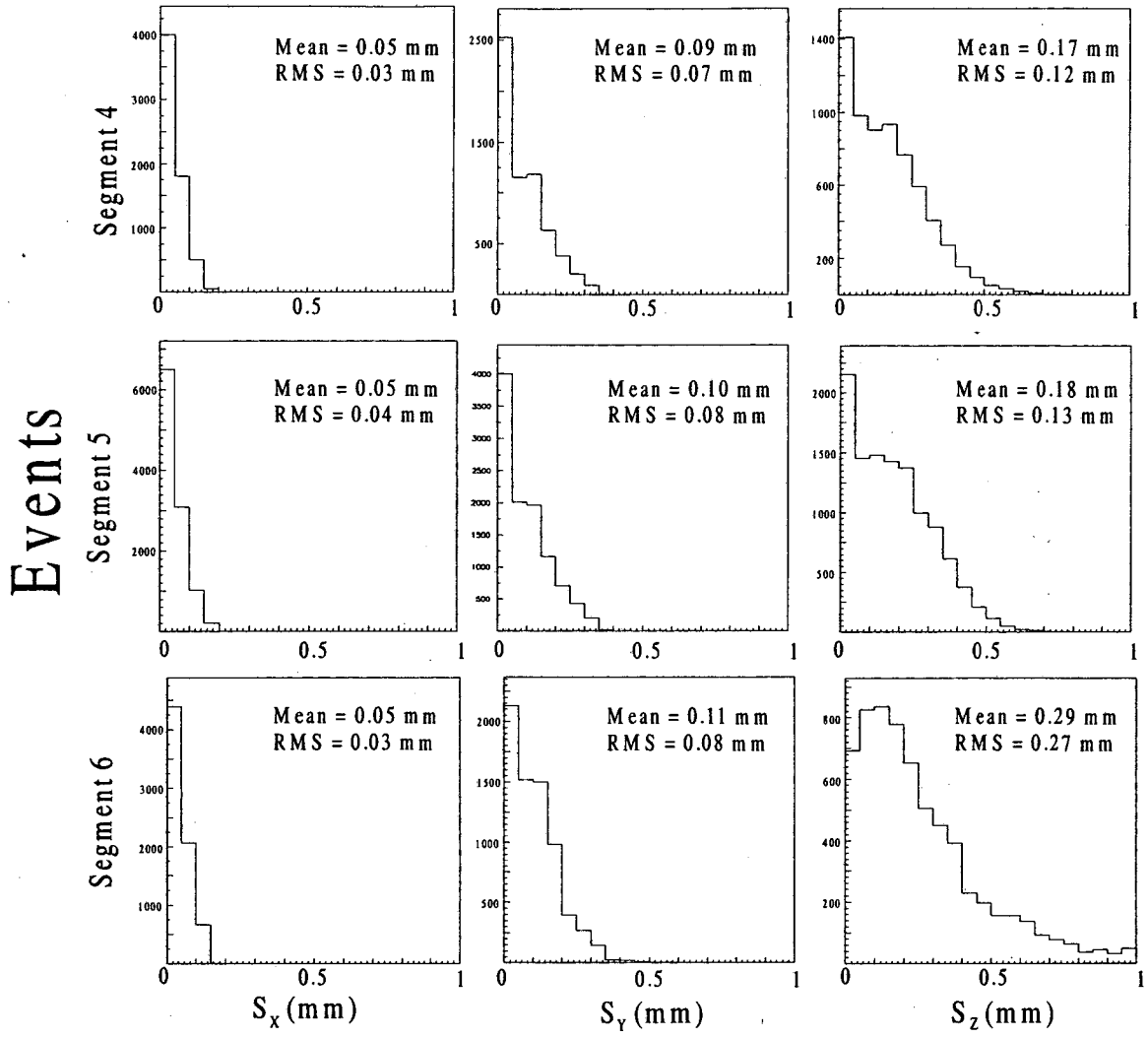

Figure 3.16b: Distributions of the single-interaction sensitivities in the X-, Y-, and Z-directions for energy deposition of 662 keV for segments 4-6. The mean and RMS values are given for each distribution.

The mean value of S_z in segment 6 is greater than segment 5 despite the fact that it is a smaller segment. This is due to the fact that segment 6 has only one Z neighboring electrode. The smallest S_z mean value is seen in segment 1. This arises because the electrodes of the first segments cover the front face of the detector. This gives them unique electric field characteristics and makes them more sensitive to changes in

interaction location in the Z-direction (very similar to a position-sensitive germanium detector of the planar geometry described in reference 42). Additionally, the mean values of S_x remain very similar despite the size of the segments. This is because in segments 2-6 the X direction is very similar to that along the direction of the charge-carrier drift path (see Figure 3.1). Therefore, changes in interaction location in this direction result in variations in drift time of the electrons and holes, thereby changing the pulse shape on the charge-collecting electrode. Here, the pulse shape from the charge-collecting electrode provides the majority of position information in the X-direction rather than the neighboring electrodes. This is very similar to the method by which one-dimensional position information is extracted from a non-segmented coaxial detector (references 17,30, and 31).

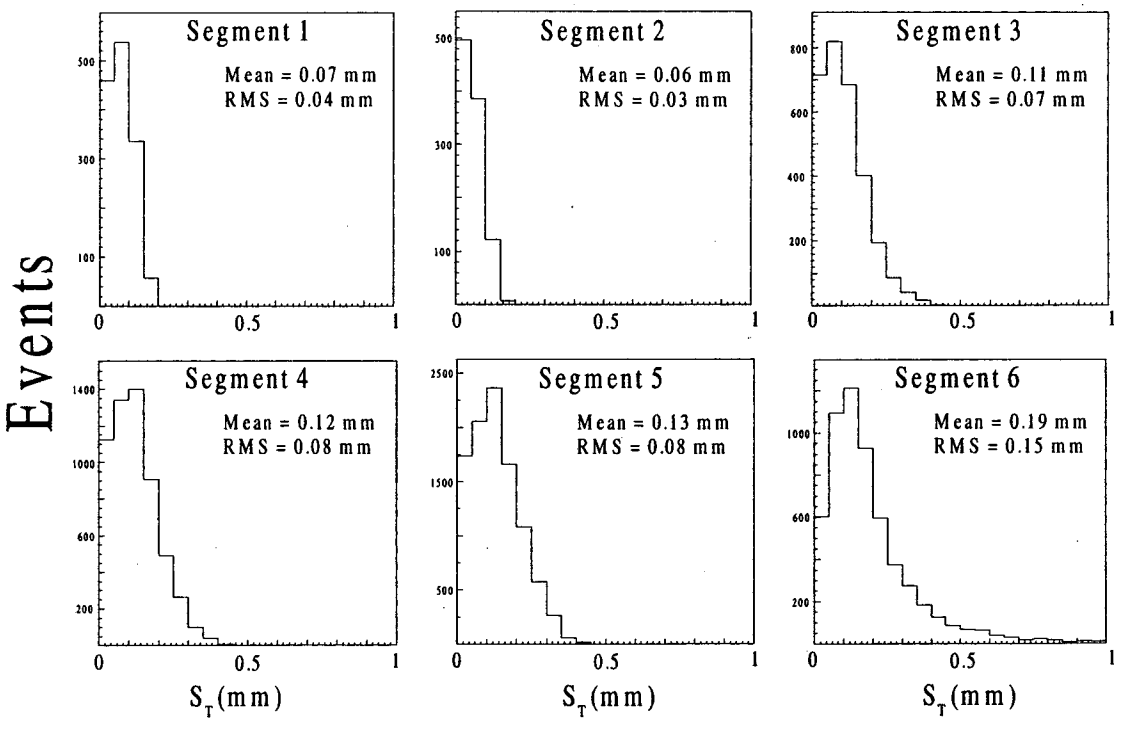

Figure 3.17: Distributions of the total single-interaction sensitivities for energy deposition of 662 keV for each of the segments. The mean and RMS values of each distribution are shown.

Distributions of the total sensitivity S_T, by segment, are shown in Figure 3.17. The values of $\overline{S}_T$ follow with the segment size (i.e. larger segments have greater $\overline{S}_T$) with the exception of segment 6 which lacks one set of Z neighbors. For future comparison to the signal decomposition results presented in Chapter 4, it is important to point out the regions in the detector with the S_T values substantial larger than the mean. These are regions in which it may be more difficult to accurately determine the location of an interaction. Figure 3.18 shows the distribution of S_T throughout the entire detector having a mean value of 0.134 mm.

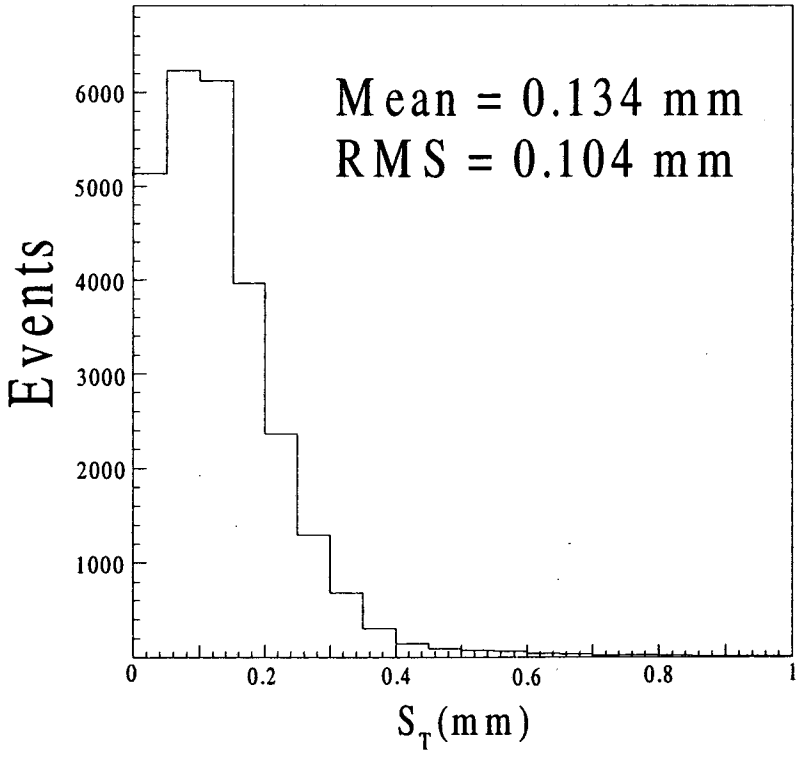

Figure 3.18: Total single-interaction sensitivity distribution for energy deposition of 662 keV.

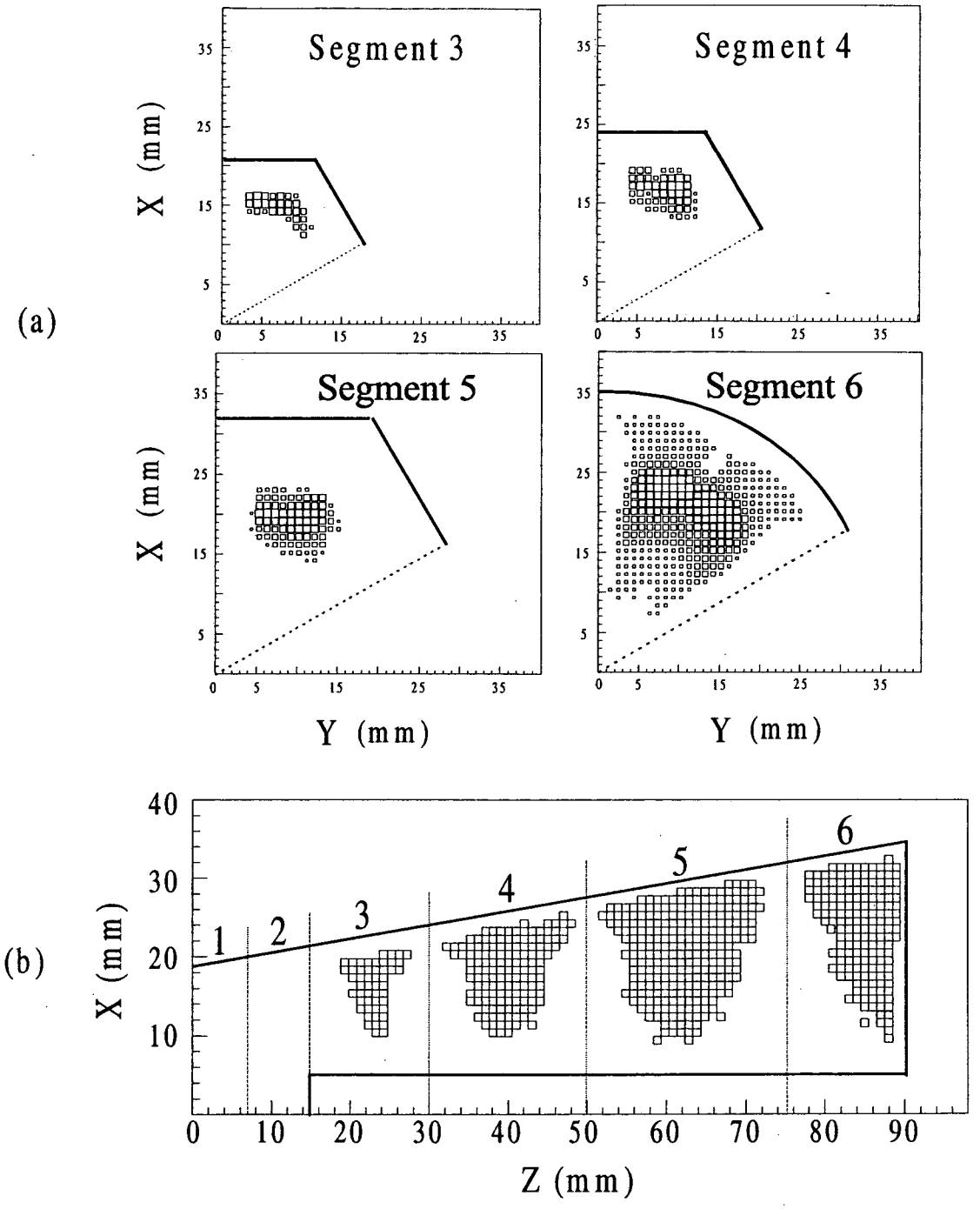

Figure 3.19: Distributions in the XY (a) and XZ (b) projections of positions having a total sensitivity greater than 0.5 mm. Note that the dashed lines show the segment boundaries and the size of the box indicates the relative intensity in (a).

Figure 3.19a and b show cross sections of segments 3-6 in XY projections and 1-6 in the XZ projection, with open boxes marking the positions that have a S_T greater than 0.5 mm. In the XY distributions, the relative size of the box indicates the intensity in that region. Clearly, the effect of segment size is evident. Namely, the regions with S_T greater than 0.5 mm only appear in the 4 largest segments and, out of these, the areas become more widespread the larger the segment size. The regions of large S_T tend to be located near the center of each segment volume. In these regions, the weighting potentials are rather small for all of the neighboring segments and thus the induced signals are relatively small. This reduces the amount of position information (i.e. pulse shape difference) which can be extracted relative to the noise level and leads to an increase in S_T.

Thus far, the examination of position sensitivity has been carried out using calculated pulse shapes. In order to validate these findings, a comparison was made using the experimentally measured pulse shapes presented in Section 3.2. However, the experimental pulse shapes contain noise that is not present in the calculated pulse shapes. The position sensitivity was derived to examine pulse shape differences (in Equation 3.2) based solely on a change in interaction position, not including that of statistical noise. In order to greatly reduce the statistical fluctuations due to noise and allow the experimentally measured pulse shapes to be analyzed in the same fashion as those calculated, the distribution of pulse shapes recorded at each position (see Figure 3.7) were averaged. By averaging the pulse shapes, a single pulse shape was obtained at each location representing the mean of each distribution. In the process statistical fluctuations are reduced and a noise level approximately 50 times lower (dependent upon the number

of pulse shapes recorded at a given location) than the measured level of 5 keV was achieved. The mean pulse shapes were then used in Equations 3.2 and 3.3 to calculate position sensitivities between all combinations of measured positions. The spacing between the centroid of adjacent positions (Δr_{ij} in Eq. 3.3) varied dependent upon direction. Positions were separated by 4 mm in the X-direction, and 3 mm in both the Y- and Z-direction. For comparison, the procedure was repeated using calculated pulse shapes resulting from a single γ-ray interaction of 374 keV at the centroid of each position. Again, a noise level σ_n of 5 keV was used.

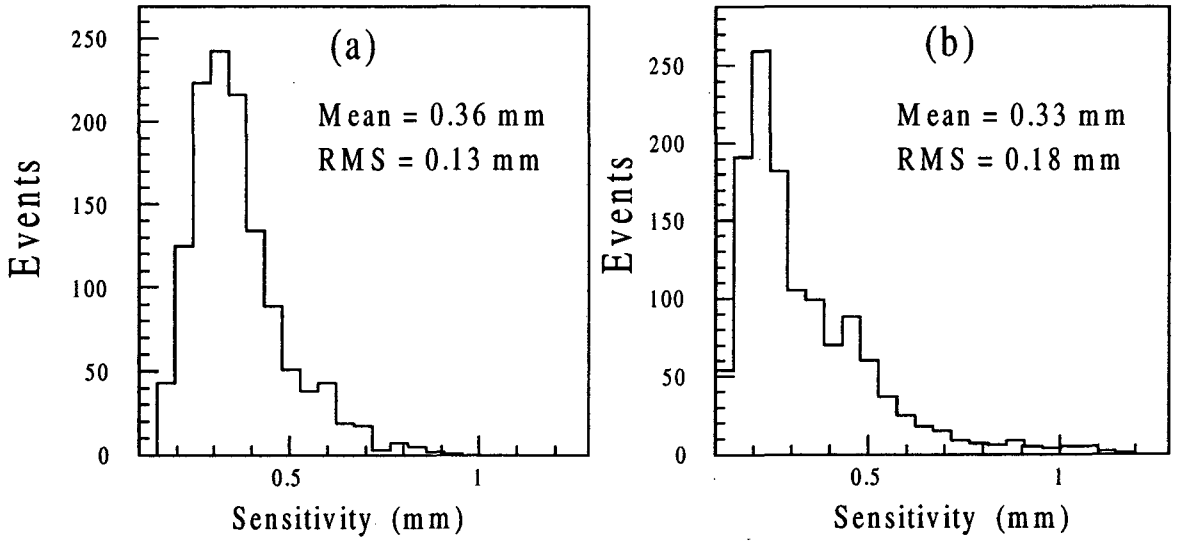

Figure 3.20: (a) Distribution of position sensitivities calculated from experimentally measured pulse shapes from single interactions with energy deposition of ~374 keV. (b) Position sensitivity distribution calculated using modeled pulse shapes at the same positions as those measured.

Figure 3.20a and b show the distributions of total sensitivities calculated from experimentally measured and calculated pulse shapes, respectively. The mean values of 0.36 mm for the experimental pulse shapes and 0.33 mm for the calculated pulse shapes are in excellent agreement with one another. The similarities in RMS deviations indicate that the shapes of the distributions are in good agreement as well. This further accentuates the ability of the model to reproduce experimental pulse shapes. Additionally, the effect of the decrease in energy to 374 keV, relative to the previous examination at 662 keV, is evident in the increase in mean sensitivities shown in Figures 3.20a and b as compared to Figure 3.18.

3.3.2 Multiple-Interaction Position Sensitivity

In the energy range of interest, a γ ray incident on the prototype detector will most likely undergo multiple interactions in the detector crystal. In such cases, the resulting pulse shape at each segment electrode will be the sum of the individual electron and hole components from each of the interactions [43]. Modification of Equation 3.1 to allow for multiple interactions yields:

$$\Delta Q_j = \sum_{p=1}^{N} \frac{q_p}{V_o} \left(\left(E_j(r_e) \bullet v_e \right)_p + \left(E_j(r_h) \bullet v_h \right)_p \right) \Delta t \,, \tag{3.5}$$

where ΔQ_j is the induced charge on electrode j, over the time interval Δt, from the N interactions and q_p represents the charge deposited at each interaction p. The individual electron and hole components for each interaction are separated, such that $E_j(r_{e,h})$

represents the weighted electric field for segment j at the location of the electrons or holes along their drift path for interaction p. Equation 3.5 clearly illustrates that the total pulse shape is the superposition of the individual pulse shapes from each interaction.

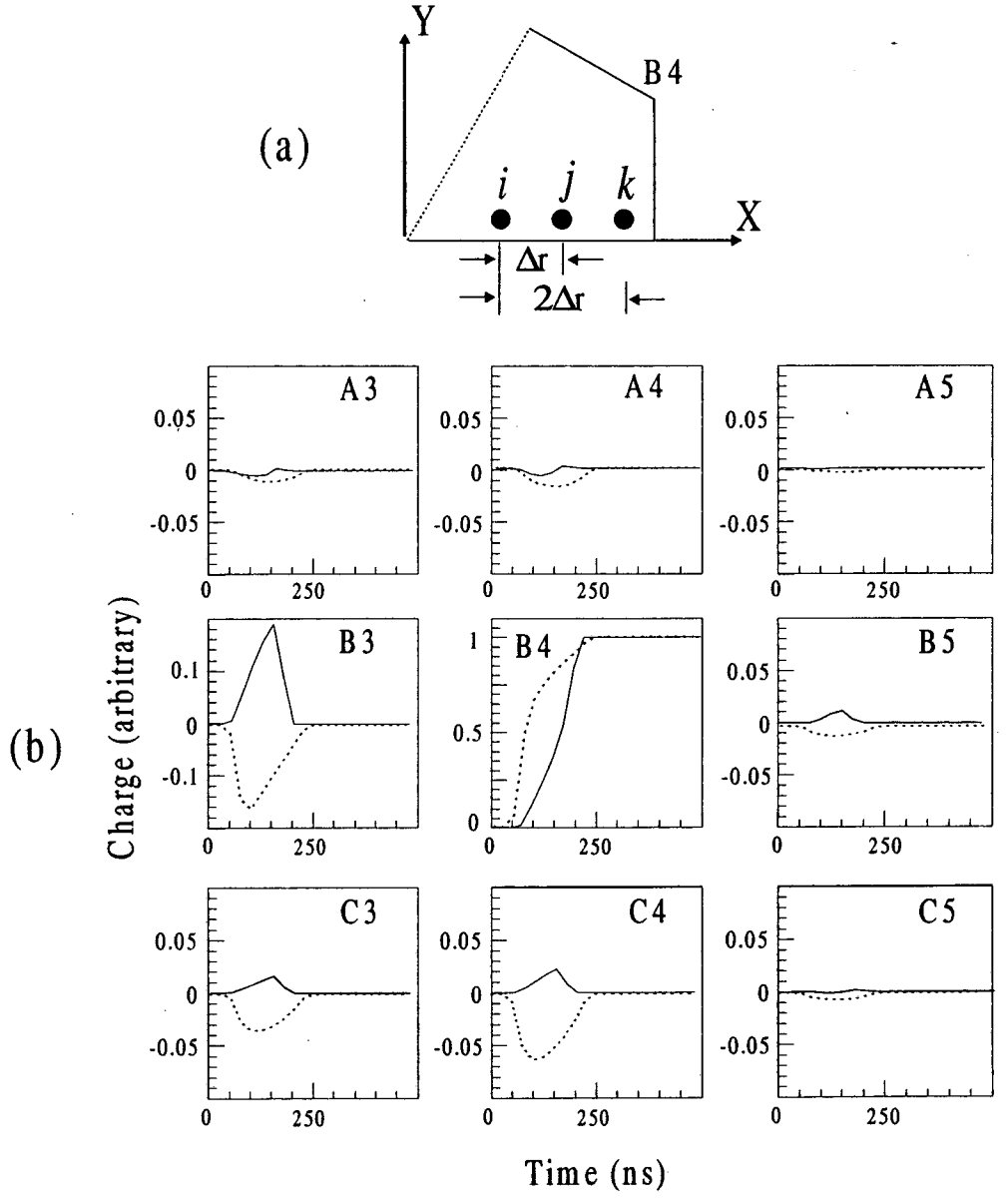

Figure 3.21: (a) XY cross section of segment B4 showing positions i, j, and k with $\Delta r = 2$mm. (b) Calculated pulse shapes for an interaction at i (solid trace) and k (dashed trace) in segments A3-5, B3-5, and C3-5.

In principle, the position sensitivity can be expanded to examine pulse shapes from any number of interactions. Here, however, the study will be limited to two interactions of equal charge deposition. This position sensitivity will provide a measure of the distance between two interactions needed to distinguish their resulting pulse shape from that of a single interaction occurring at a position halfway between the two. To illustrate this, Figure 3.21a shows a cross section through the detector and three positions labeled i, j, and k each separated by a distance Δr = 2 mm. The calculated pulse shapes for individual interactions occurring at positions i and k are shown in Figure 3.21b. According to Equation 3.5, the pulse shape resulting from a γ ray undergoing interactions at positions i and k will be the superposition of the individual pulse shapes. Figure 3.22 illustrates the pulse shapes of a single interaction at position j and that resulting from two interactions, one at i and one at k. The charge deposited in each case is normalized to one, such that $q_j = q_i + q_k = 1$ and $q_i = q_k = 0.5\ q_j$. In order to distinguish one another, the difference in pulse shape must be greater than the noise level σ_n.

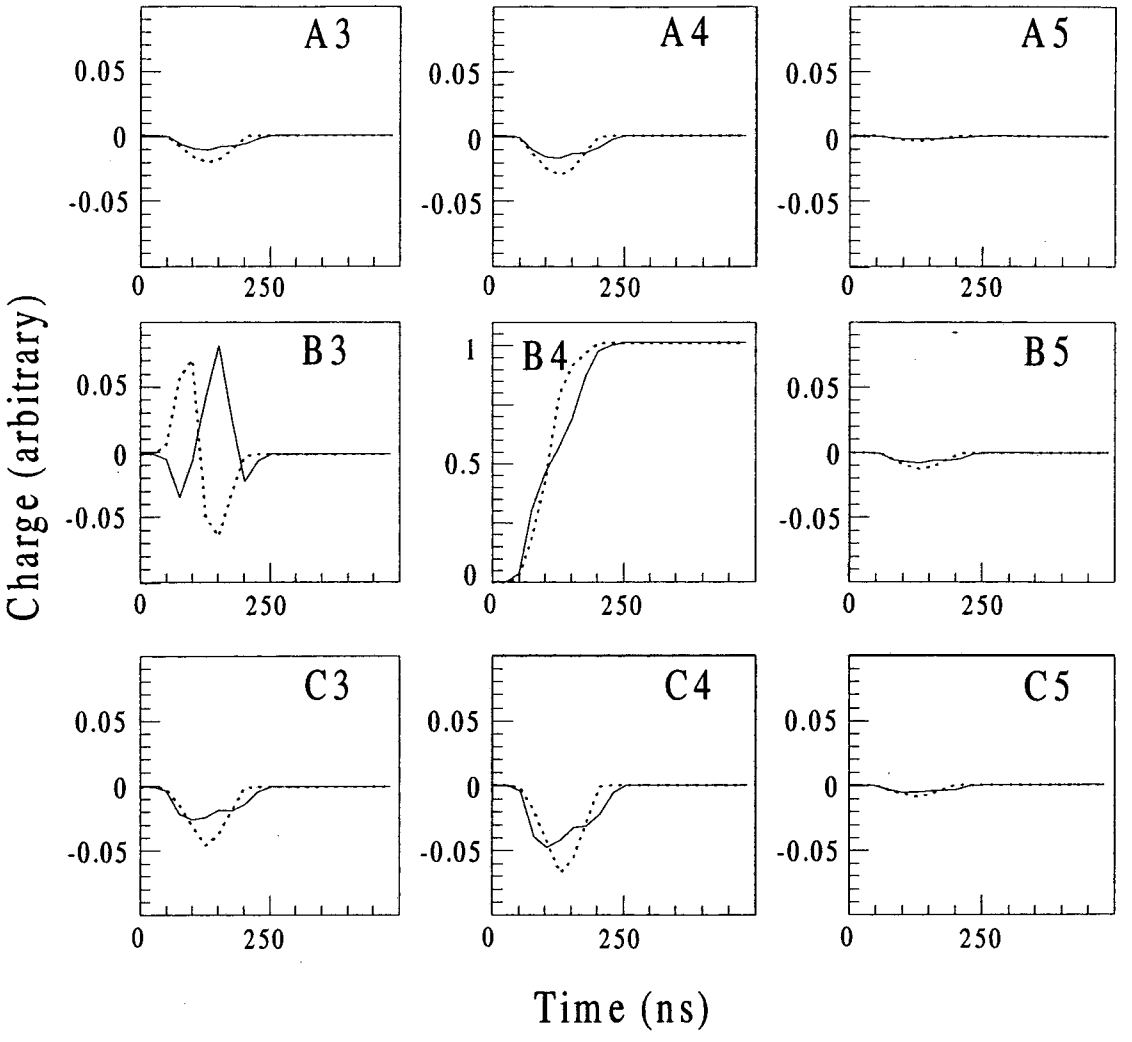

Figure 3.22: Calculated pulse shapes for two interactions at positions *i* and *k* (solid trace) and a single interaction at j (dashed trace) for segments A3-5, B3-5, and C3-5.

As a means of quantifying this difference, χ^2 is derived as described in Section 3.3.1 with the exception that the total noise level, σ_t, must take into account contributions from all three pulse shapes which add in quadrature according to each pulse shapes relative amplitude such that:

$$\sigma_t^2 = \left(\tfrac{1}{2}\sigma_i\right)^2 + \left(\tfrac{1}{2}\sigma_k\right)^2 + \left(\sigma_j\right)^2 . \tag{3.6}$$

Again, the noise level is considered to be independent of position, therefore, $\sigma_i=\sigma_k=\sigma_j=\sigma_n$. This gives a total noise level of $\sqrt{\frac{3}{2}}\,\sigma_n$ and $(\chi_{ijk})^2$ is now defined as:

$$\chi_{ijk}^2 = \sum_{m=1}^{36}\left[\frac{\int_0^{t_c}\left((q_i^m(t)+q_k^m(t))-q_j^m(t)\right)dt}{\sqrt{\frac{3}{2}}\sigma_n}\right]^2 . \tag{3.7}$$

The notation of m and t are the same as Equation 3.2. Using χ_{ijk}, the sensitivity for distinguishing the two interactions from a single interaction is defined as:

$$S_{ijk} = \frac{\Delta r^2}{\chi_{ijk}} . \tag{3.8}$$

In order to maintain a consistent solution between S_{ijk} and the total separation of i and k (i.e. $2\Delta r$) when χ_{ijk} =1 the Δr term in Equation 3.8 is squared. As an example, assume χ_{ijk} =1 for Δr = 2 mm. Therefore, the noise level is exactly equal to the pulse shape differences with i and k separated by 4 mm. This yields a S_{ijk} = 2 mm^2 in Equation 3.8 and thus corresponds a separation between i and k given by $2\sqrt{S_{ijk}}$ = 4 mm. However, if χ_{ijk} is less than 1, indicating that the difference in the pulse shapes is not above the total

noise level, the resulting S_{ijk} will be greater than Δr^2. Just as in the single interaction case derived in Section 3.3.1, the resulting S_{ijk} can used approximated the total separation distance required to distinguish the pulse shape of two interactions occurring at i and k from that of a single interaction at j. This is given by $2\sqrt{S_{ijk}}$ which will be greater than the $2\Delta r$. The opposite is true for a χ_{ijk} greater than 1 and the resulting $2\sqrt{S_{ijk}}$ will be less than $2\Delta r$. As in the previous section, the position sensitivity for two interactions can be examined in each coordinate direction at a given location with the total sensitivity given by Equation 3.4.

In order to examine the two-interaction position sensitivity in the prototype detector, calculated pulse shapes were utilized from locations separated by a Δr = 1 mm in each coordinate direction. The study was performed for a total energy deposition in the two interactions of 662 keV and a noise level σ_n of 5 keV. The pulse shape resulting from the two interactions (one at i and one at k) of equal energy deposition (331 keV each) was compared to a single interaction at j of 662 keV. The sensitivity, in each direction, was calculated using Equations 3.7 and 3.8. As in the previous section, the sensitivity values were grouped according to the segment collecting the charge. Figures 3.23a and b show the distributions of sensitivity values in the X-, Y- and Z-directions for each of the segments.

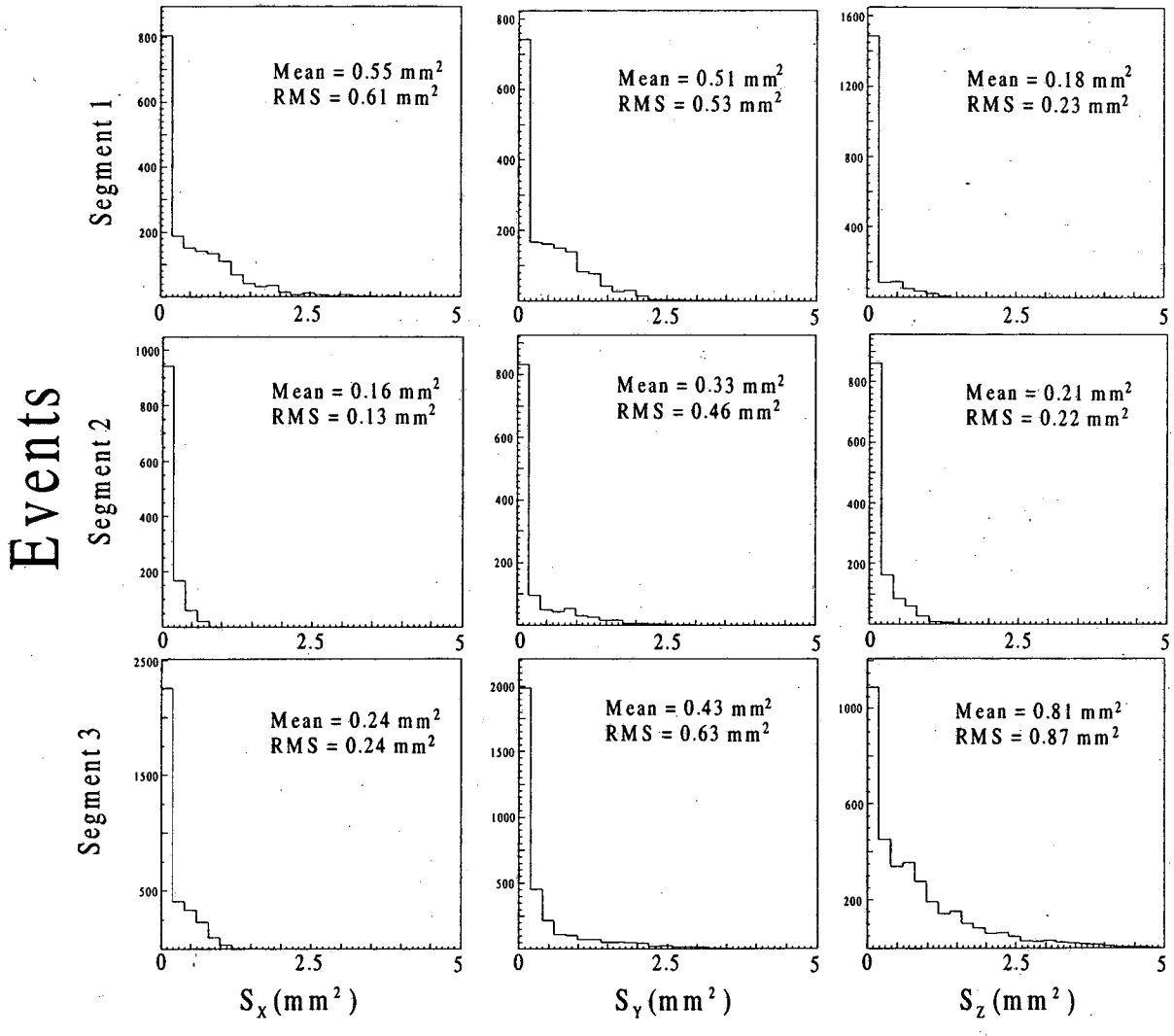

Figure 3.23a: Distributions of the two-interaction sensitivities in the X-, Y-, and Z-directions for energy deposition of 662 keV for segments 1-3. The mean and RMS values are given for each distribution.

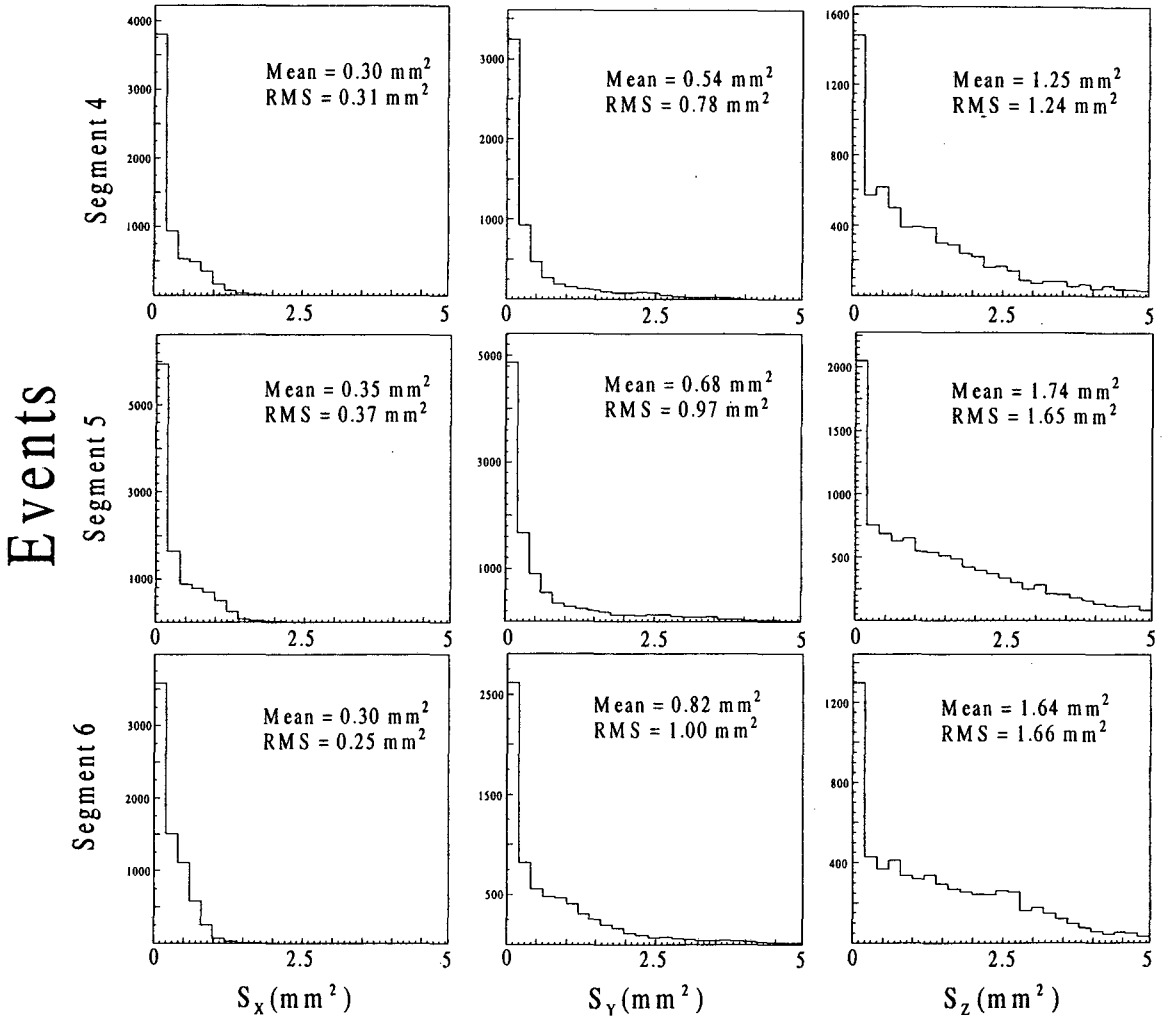

Figure 3.23b: Distributions of the two-interaction sensitivities in the X-, Y-, and Z-directions for energy deposition of 662 keV for segments 4-6. The mean and RMS values are given for each distribution.

In general, the same features arise as previously discussed for the single-interaction position sensitivity (see Section 3.3.1). However, in this case the mean values are substantially larger than before. Here, sensitivity values greater than 1 mm^2 are present in nearly every distribution for each of the segments. This means that there are areas in which the separation of the two interactions must be greater than 2 mm in order to distinguish the resulting pulse shape from the pulse shape of a single interaction between them. As in the single interaction study, the areas with highest sensitivity values occur in the regions away from segment boundaries. The distributions of the total sensitivity S_T for each segment are shown in Figure 3.24. The mean sensitivity $\overline{S}_T$ increases with increasing segment size and ranges from 0.26 mm^2 in segment 2 to 1.23 mm^2 in segment 5. The distribution of total sensitivity for all of the segments is illustrated in Figure 3.25. The $\overline{S}_T$ of 1.01 mm^2 indicates that on average the two equal energy interactions from a 662 keV γ ray must be separated by about 2 mm in order to be distinguished from a single interaction between them. The impact of this relative to the ability to extract the location of γ-ray interactions from pulse shapes will be discussed Chapter 4.

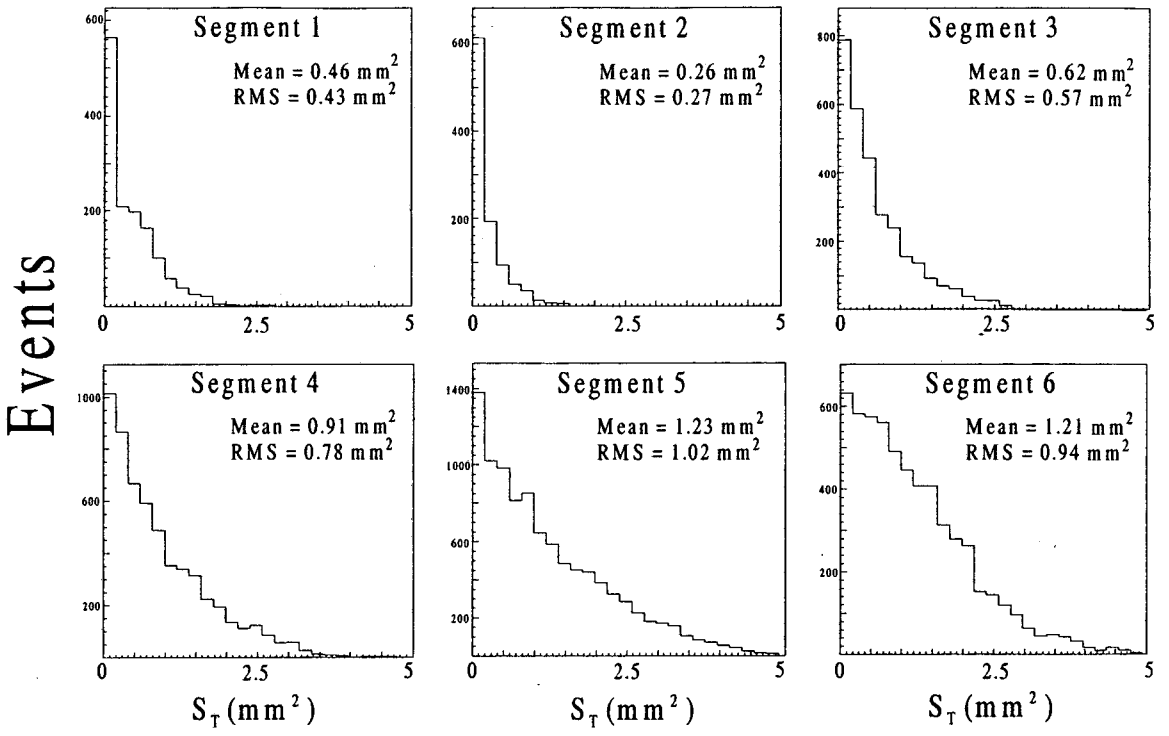

Figure 3.24: Distributions of the total two-interaction sensitivities for energy deposition of 662 keV for each of the segments. The mean and RMS values of each distribution are shown.

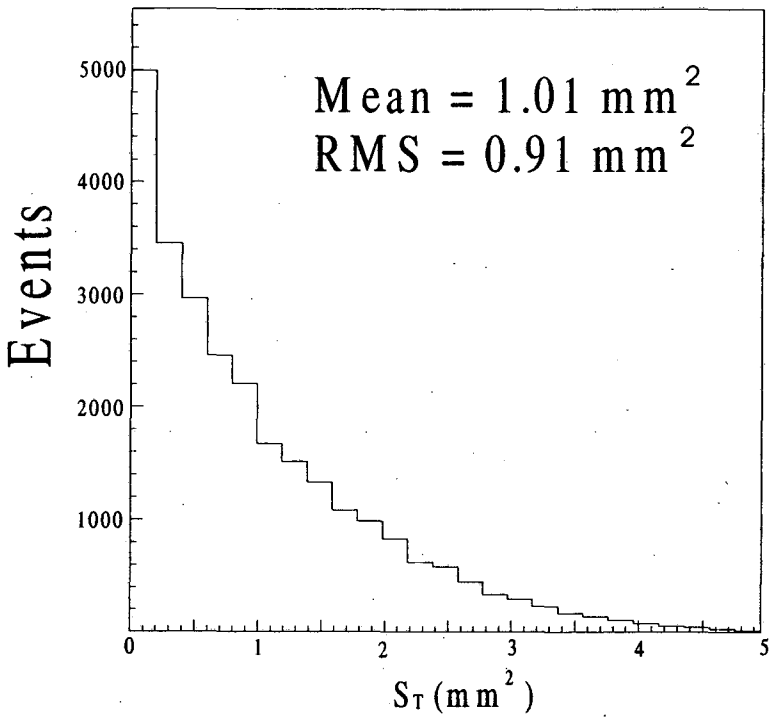

Figure 3.25: Total two-interaction sensitivity distribution for energy deposition of 662 keV.

3.3.3 Discussion

In the case of a single interaction with energy deposition of 662 keV, the mean position sensitivities obtained using calculated pulse shapes from each segment ranged from 0.06 to 0.19 mm with the larger segments having the greater sensitivity values. Additionally, it was found that the areas with greater sensitivity values lie in the central regions of the segments, away from segmentation boundaries. This indicates that reducing the size of the segmentation increases the change in pulse shape relative to a change in interaction location, thus improving the position sensitivity. Furthermore, the

study brought out the fact that the sensitivity of the pulse shapes is dependent upon direction. Interactions separated in the direction close to that of the charge carrier drift (i.e. the X-direction in segments 2-6 and Z-direction in segment 1) have lower values of position sensitivity and thus greater differences in pulse shape. Using experimentally measured pulse shapes it was shown that very similar results are found indicating good agreement with the modeling.

The results of the single-interaction position sensitivity study at 662 keV as well as the limited examination at 374 keV show sensitivities well below that of the desired position resolution of ~2 mm. This indicates that factors such as the range of the primary electron, the finite size of the charge-carrier distribution, and electronic characterization of the detector crystal discussed in Section 3.2.3 may ultimately limit the ability to localize a single γ-ray interaction rather than the current segmentation size. However, extending the examination to allow for multiple interactions in a single segment leads to a very different conclusion. The investigation of the two-interaction position sensitivity, at an energy of 662 keV, yielded mean sensitivities ranging from 0.26 to 1.23 mm^2 for the special case examined (e.g. equal energy deposition in each interaction). In the larger segments of 4 and 5, there are regions in which the separation needed to distinguish two interactions from that of a single interaction is considerably larger than 2 mm. In some cases, the position sensitivity is in excess of 2 mm^2 requiring a separation of 4 mm to distinguish the two. Because 662 keV γ rays incident on a detector of this size will likely undergo multiple interactions with a substantial portion of these interactions separated by less than about 3 mm, differentiating them may prove to be difficult especially in the

larger segments. This issue will be addressed further in the Chapter 4 which contains a description of the method utilized to determine interaction locations.

Chapter 4

IMPLEMENTATION AND ASSESSMENT OF THE SIGNAL DECOMPOSITION ALGORITHM

The position sensitivity studies, presented in the previous chapter, provide the theoretical basis for separating interactions based on pulse shapes differences. However, the ability to determine positions and energies of one or more interactions requires the use of algorithms designed to analyze the detector pulse shapes. The fact that each pulse shape can be the result of multiple interactions at various locations, each with different energy deposition, increases the complexity of the problem. Therefore, the algorithm must separate (or "decompose") a pulse shape resulting from one or more interactions into the individual components of each interaction in order to furnish the desired information. Hence, the process is generally referred to as "signal decomposition". Examples of simple signal decomposition are the analytical methods, described in reference [17, 30, and 31], implemented to extract the drift time of the charge carriers from the pulse shape and deduce one-dimensional position information. However, these existing analytical methods do not provide the desired accuracy or the ability to handle the added complexity of pulse shape formation in a segmented detector.

A signal decomposition algorithm developed specifically for determining the positions and energies of one or more interactions in the prototype detector is presented

in this chapter. The algorithm utilizes a general least squares minimization approach, whereby the input pulse shape is compared to a set of "basis" pulse shapes representing single interactions throughout the volume of the detector. The basic concept of the algorithm is described in the following section. Although the algorithm takes a rather simple approach, the complexity of the current problem led to significant difficulties in its implementation. In Section 4.2, simulations to assess the algorithm's performance using calculated pulse shapes are presented. These include the implementation of the algorithm when only one interaction per detector segment was allowed as well as when two interactions per segment were permitted. The difficulties that arose and their implications with respect to the position sensitivity studies discussed in Chapter 3 are addressed in this section. Finally, Section 4.3 contains a discussion of the finds and the impact relative to the tracking process not only for the single prototype detector but also for GRETA.

4.1 Algorithm Description

As is the case with most scientific data, it is necessary to fit a set of observations to a theoretical expression or an approximate model that depend on adjustable parameters in order to estimate the parameters of interest. This is true for the signal decomposition process. Here, the observed data are the digitized pulse shapes resulting from energy deposition within the detector crystal for each of the 36 segment electrodes. In the fitting process, the theoretically calculated "basis" pulse shapes are assumed and the adjustable

parameters are the number, locations, and energies of all interactions needed to reproduce the digitized pulse shape with reasonable fidelity.

There are many mathematical methods that have been developed for fitting data to a model. The signal decomposition algorithm developed here utilizes one of the most basic methods based on general linear least squares fitting. Other possible approaches utilizing algorithms that are more complex will be discussed in Section 4.3. Here, the fitting procedure will first be discussed in a general context and then in its specific implementation for signal decomposition.

The primary approach in general least squares fitting is to design a "merit function" that provides a measure of the agreement between the data and model given a particular choice of parameters. As a generic example, assume that a set of observed data points (x_i, y_i) is to be fit by a model that is a linear combination of any M specified functions of x. The general form of the model is then given as:

$$y(x) = \sum_{k=1}^{M} a_k X_k(x), \tag{4.1}$$

where $X_1(x),\ldots, X_M(x)$ are fixed functions of x, called "basis functions". In general, the basis functions can be nonlinear functions of x. The term "linear" refers to the model's dependence on the adjustable parameters a_k. The merit function is defined as:

$$\chi^2 = \sum_{i=1}^{N} \left[\frac{y_i - \sum_{k=1}^{M} a_k X_k(x_i)}{\sigma_i} \right]^2 . \qquad (4.2)$$

Here, the merit function is summed over the N individual measured data points. Since observed data are subject to measurement error, generally they do not exactly fit a model even when the model "exactly" represents the physical problem under consideration. This is taken into account by including the parameters σ_i, which represent the standard deviations distribution function for the ith data points. The merit function is arranged such that small values represent close agreement between the data and model.

The parameters of the model must be adjusted to bring about a minimum in the merit function. This can prove to be a complex problem given several parameters with large dimensions. There are several techniques available for adjusting parameters and finding the minimum such as solution by normal equations, adaptive grid search, singular value decomposition (SVD), and sequential quadratic programming (SQP). They differ by the amount of computation each requires and accuracy to which the parameters are returned. However, each of these processes will yield a set of so called "best-fit parameters" which provide a minimum in the merit function. It is important to point out that the parameters represent a minimum achieved in χ^2 and may not be the overall best solution. It is not uncommon in complex problems that χ^2 will have more than a single minimum. In most cases, the interest is in the absolute or global minimum rather than local minima that exist in the parameter space. Given a complex problem, finding the

global minimum can prove to be difficult with any minimization process. This feature will be discussed with respect to the signal decomposition process in Section 4.2.2.

The implementation of the general least-squares fitting into an algorithm for the signal decomposition is rather straightforward following the basic description above. The observed data (or simulated data, as will be discussed in Section 4.2) are each of the segment electrode's digitized pulse shapes for each event (one or more γ-ray interactions). Therefore, the data can be represented by the set $(t_i, q_i)_s$, where q_i is the charged measured on electrode s at time t_i. The pulse shapes calculated theoretically (see Section 3.1) will serve as the basis functions of the model by which the observed pulses are to be decomposed. Characterizing the model in terms of Equation 4.1 for an event with M interactions yields:

$$q(t)_s = \left(\sum_{k=1}^{M} E_k X_k(x_k, y_k, z_k, t) \right)_s , \tag{4.3}$$

where $q(t)_s$ is the calculated charge on segment electrode s at time t. The superposition property of the pulse shapes (see Section 3.3.2) allows the basis functions X_k, which represent the pulse shape resulting from energy deposition at a single location (x, y, z), to be summed over each interaction. This results in the total pulse shape for the M interactions. Since the amplitude of the basis functions in the charge-collecting electrode are normalized to one, E_k represents the fraction of the total energy deposited in interaction k. The adjustable parameters to be determined are the number of interactions M, the fraction of energy deposited E_k and position $(x, y, z)_k$ of each interaction. The merit function for the algorithm is defined by:

$$\chi^2 = \sum_{s=1}^{36} \sum_{t=t_o}^{t_c} \left[\frac{q_i(t_i) - \sum_{k=1}^{M} E_k X_k(x_k, y_k, z_k, t_i)}{\sigma_i} \right]^2 . \quad (4.4)$$

The merit function is summed over the 36 segment electrodes s from the beginning t_o until the end of the pulse t_c. σ_i represents the measurement error or noise (i.e. 5 keV as discussed in Section 3.3.1). The difference between the observed charge q_i and that given by the model is evaluated at each time sample. Therefore, the sampling frequency of the modeling must match that at which the observed pulse was recorded (i.e. for a 500 MHz ADC the charge is recorded every 2 ns).

The minimization of the merit function via the adjustment of the previously mentioned parameters is a multi-step process. At the heart of the process is a SQP routine that is part of the NAG FORTRAN library [44]. The SQP method itself is a rather complex iterative process and a detailed description is provided in references 45-49. The SQP routine is designed to minimize an arbitrary function, in this case χ^2, subject to both linear and nonlinear constraints on the functions parameters. Constraints are placed on E_k to conserve total energy, e.g.,

$$\sum_{k=1}^{M} E_k = 1, \quad (4.5)$$

and $0 < E_k \leq 1$. Both linear and nonlinear constraints are placed on x, y, and z to restrict them to the physical boundaries of the detector crystal. Ideally, constraints would not be placed on the number of interactions k since it can range from 1 to M for any particular event. However, evaluation of the algorithms performance will be conducted by limiting

$k = 1$ and $k = 2$ interactions for each segment which measures net charge. This is done to limit the complexity of the problem and prevent breakdown of the SQP routine, as will be discussed in Section 4.2.2.

For simplicity in describing the steps the algorithm takes to return the best-fit parameters, assume that a single interaction takes place in the detector and the parameter k is limited to one in the SQP routine. In addition, assume that the acquisition system employed to digitize the pulse shape has the ability to extract the value of total energy deposited, E_T, in the event. The system employed for the experimental measurements presented in Chapter 5 and described therein has this ability. First, the parameters to be determined are declared in the algorithm. In this case, k is constrained to 1 and according to Equation 4.5, $E_1 = 1$. Therefore, the only adjustable parameters are the x, y, and z coordinates of the interaction. An initial guess to the solution is then made in the algorithm. Because it is easy to determine the segment collecting charge (e.g. the segment in which the interaction takes place) by the pulse shape, the center of this segment serves as the initial guess for x, y and z. Equation 4.3 is evaluated given the initial guess and the modeled basis pulse shape is returned. Next, the merit function is calculated via Equation 4.4. The values of the parameters as well as the merit function are supplied to the SQP routine. The routine makes the necessary adjustments to the parameters, Equations 4.3 and 4.4 are reevaluated and the merit function is supplied back to the SQP routine. This iterative process continues until a minimum in the merit function is found and the x, y, and z coordinates are returned.

In principle, the algorithm can be extended to allow for any number of interactions and its solution process would be the same as that outlined in the previous

example. The following section contains results from simulations performed to access the algorithm's performance allowing both one and two interactions in a single segment. Simulations allowing one interaction provide comparison to the results obtained in the single-interaction position sensitivity studies presented in Section 3.3.1. The added complexity and problems that arise when the algorithm is extended to allow two interactions in a single detector segment will be discussed in relation to the multiple-interaction position sensitivity results of Section 3.3.2.

4.2 Simulations and Results of Signal Decomposition

4.2.1 Single Interaction

In order to perform a first order assessment of the algorithm, the simplest decomposition scenario was chosen. This entails supplying the algorithm with a pulse shape from a single interaction and constraining the search by the algorithm to a single interaction. In order to perform an extensive examination throughout the volume of the detector, simulated pulse shapes were employed. These consisted of the theoretically calculated pulse shapes with the addition of random noise to simulate that of an actual experimental measurement. The noise added to the charge at each time sample of the pulse had a Gaussian distribution with a full-width at half-maximum of 5 keV. The energy deposition was assumed to be 662 keV. The simulated charge q_s at time sample t is defined by the equation:

$$q_s(t) = q(t) + S_R\left(\sqrt{-2 * \ln(R_1)} * \cos(2\pi * R_2)\right), \tag{4.6}$$

where $q(t)$ is the theoretically calculated charge at time sample t, S_R is the signal-to-noise ratio (i.e. 5 keV/662 keV), and both R_1 and R_2 are random numbers between zero and one.

Simulated pulse shapes were input into the decomposition algorithm at locations separated by 2 mm in the x-, y-, and z-directions throughout the volume of the detector. In each case, the algorithm decomposed the simulated pulse shape using the basis functions, thus returning the x, y, and z position determined to minimize the merit function. Figure 4.1 shows an input simulated pulse shape (solid traces) from an interaction position of x = 16, y = 2, and z = 11 mm and the basis pulse shape (dashed traces) at the location x = 16.01, y = 2.08, and z = 11.09 mm returned by the algorithm. The pulse shape is shown for B2 (charge-collecting electrode) as well as the eight neighboring electrodes. This example illustrates the algorithm's accuracy in returning the interaction position even in the presence of signal noise.

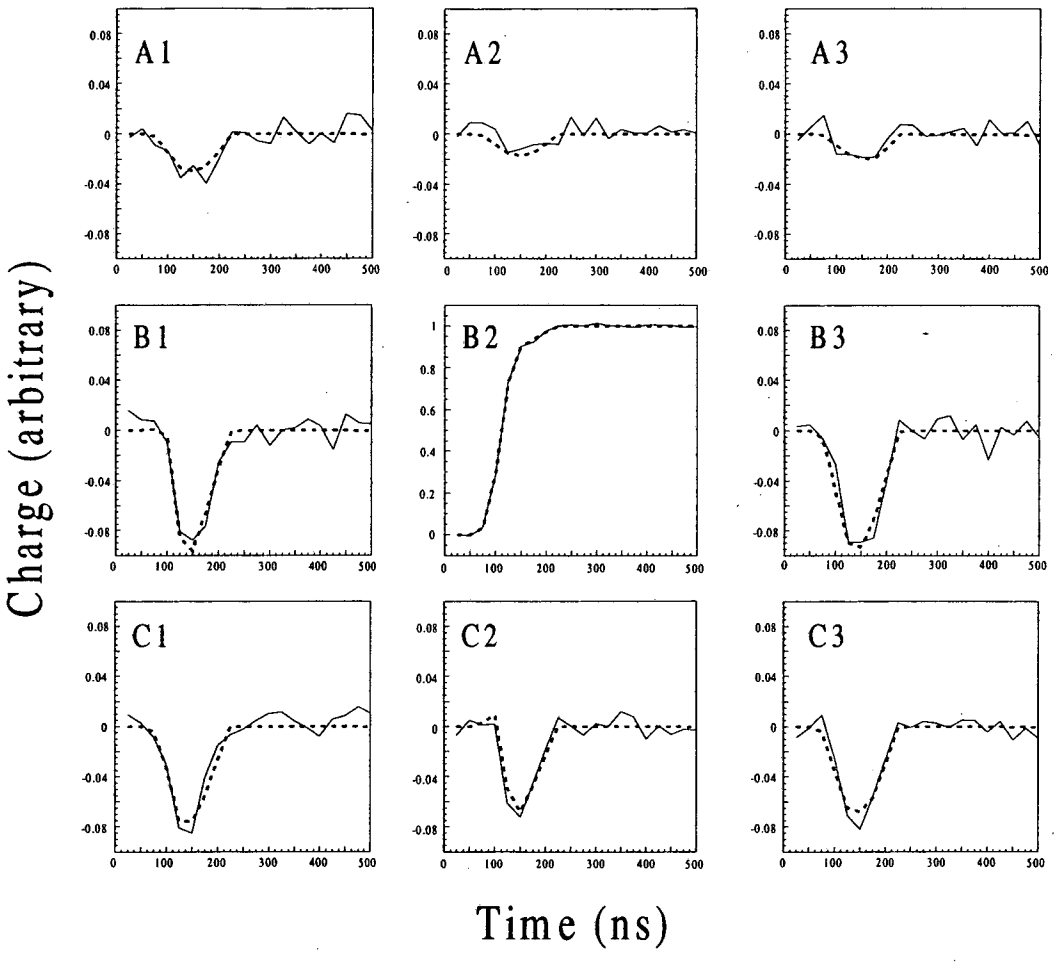

Figure 4.1: Simulated input pulse shape (solid trace) from a single interaction at position x = 16, y = 2, z = 11 mm and the basis signal (dashed trace) at position x = 16.01, y = 2.08, z = 11.09 mm return by the decomposition algorithm. Pulses are shown in segments A1-3, B1-3, and C1-3.

In order to draw a comparison between the single-interaction position sensitivity study, locations were grouped according to the segment in which the interaction occurred. Deviations (D_X, D_Y, and D_Z) between the input pulse shape position and the position returned by the algorithm were then calculated in each of the coordinate directions. Figure 4.2a and b show the distributions of the deviations, in each direction, for positions in segments 1-6. The mean and RMS deviations are indicated for each distribution. Several features arise in the examination of these distributions that were also present in

the position sensitivity study (see Figure 3.16a and b). For the same reasons described in Section 3.3.1, the mean value of D_z in segments 2-6 increases with segmentation size and the smallest mean value of D_z is seen in segment 1. Additionally, the mean values of D_x remain the same despite segment size, as in the case of S_x. The mean deviations of each distribution are of the same order as those of the position sensitivity.

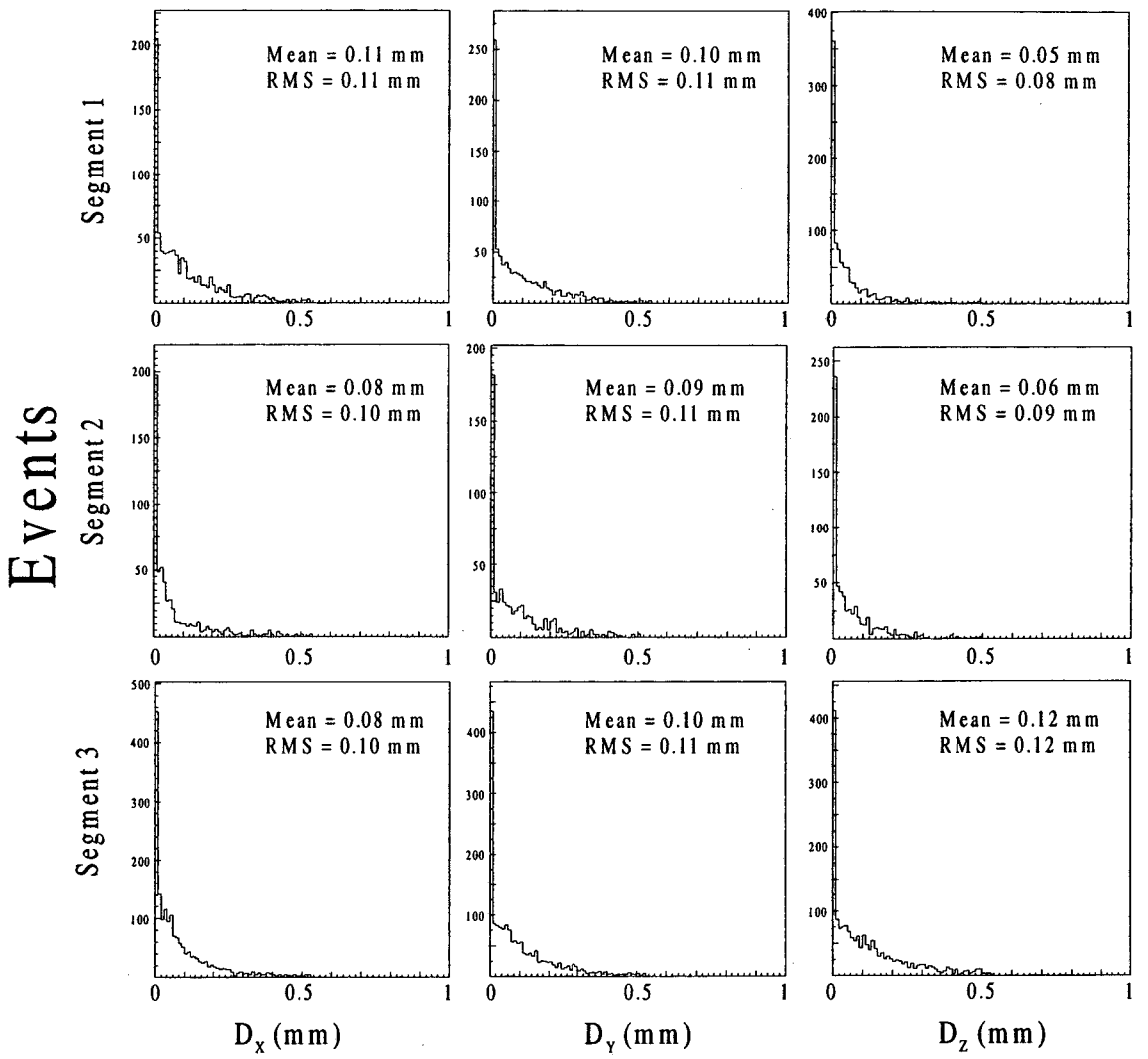

Figure 4.2a: Distributions of the deviation between the location of the input single interaction and that returned by the algorithm in the x-, y-, and z-directions at an energy of 662 keV for segments 1-3. The mean and RMS deviations are given for each distribution.

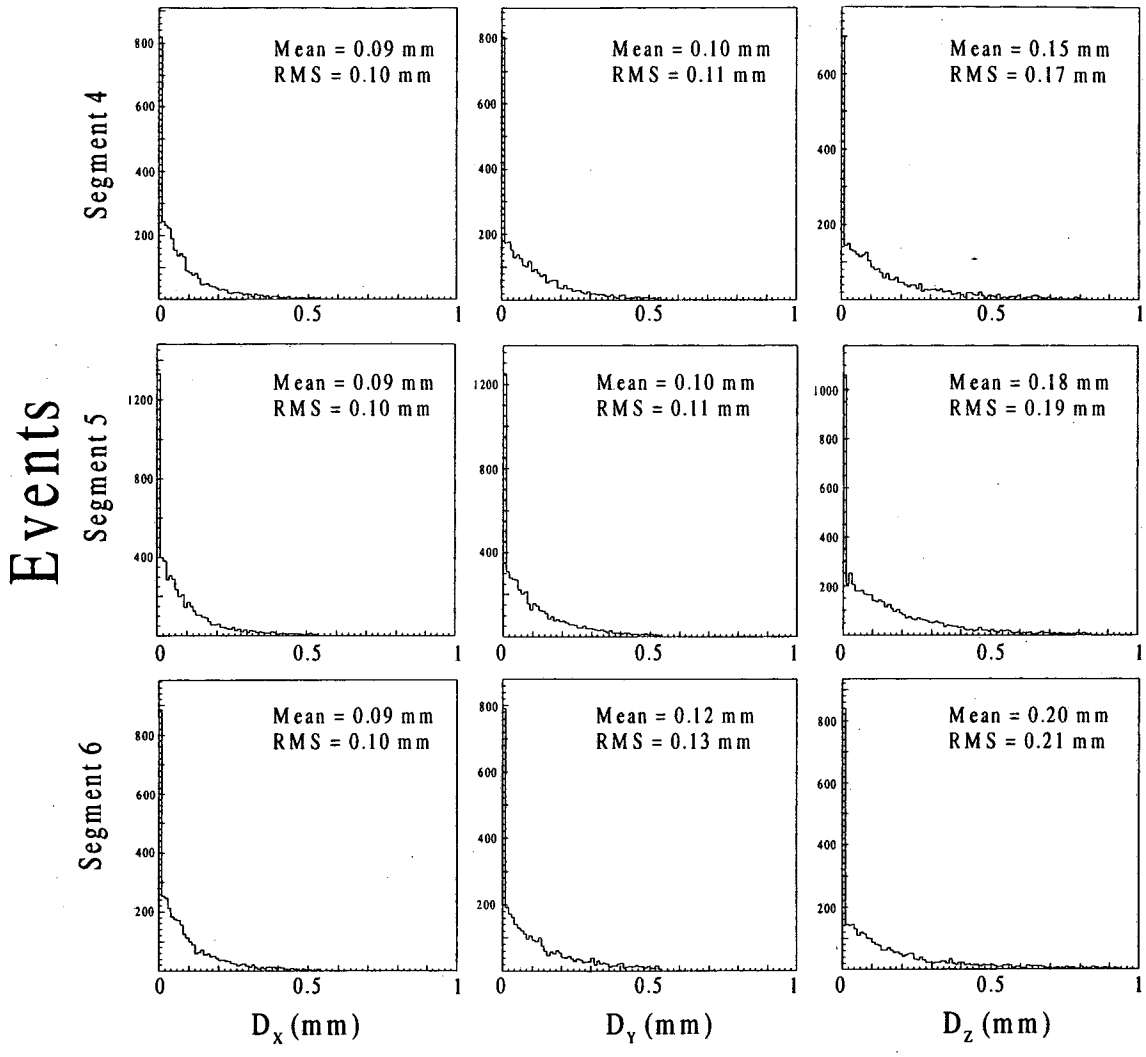

Figure 4.2b: Distributions of the deviation between the location of the input single interaction and that returned by the algorithm in the x-, y-, and z-directions at an energy of 662 keV for segments 4-6. The mean and RMS deviations are given for each distribution.

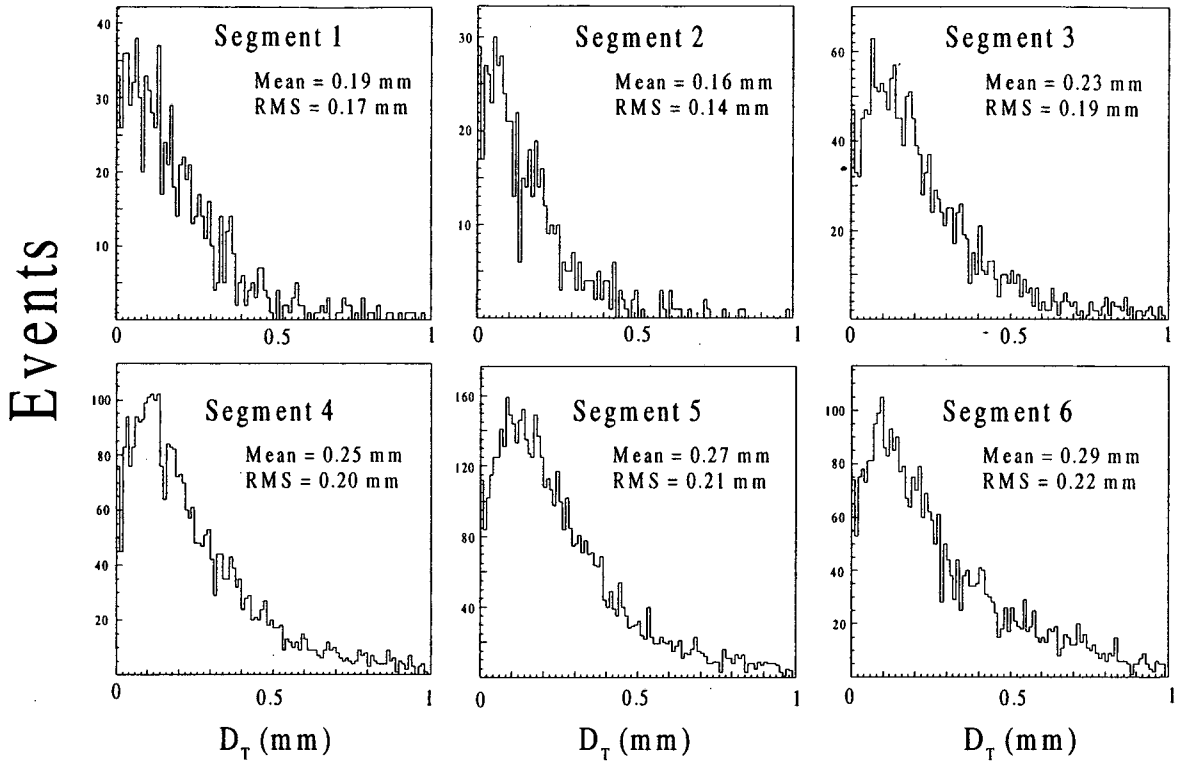

Figure 4.3: Distributions of the total deviation from a single interaction with an energy of 662 keV for each of the segments. The mean and RMS deviations of each distribution are shown.

The distributions of the total deviation D_T (i.e. $D_T = \sqrt{(D_X)^2 + (D_Y)^2 + (D_Z)^2}$), by segment, are shown in Figure 4.3. Again, an increase in the mean value is seen with segmentation size just as with S_T. The distribution of D_T throughout the entire volume of the detector is shown in Figure 4.4. The mean deviation of 0.248 mm is of the same order as the S_T mean of 0.134 mm, thus indicating that the algorithm does a good job of utilizing pulse shape differences to return the position of an interaction. To draw further comparison to the position sensitivity, Figure 4.5a and b show distributions, in the XY and XZ projections, of positions with D_T greater than 0.5 mm. As in the case of S_T (see

Figure 3.19a and b), the regions with $D_T > 0.5$ mm tend to be located near the center of the segment volume where the weighting potentials are rather small.

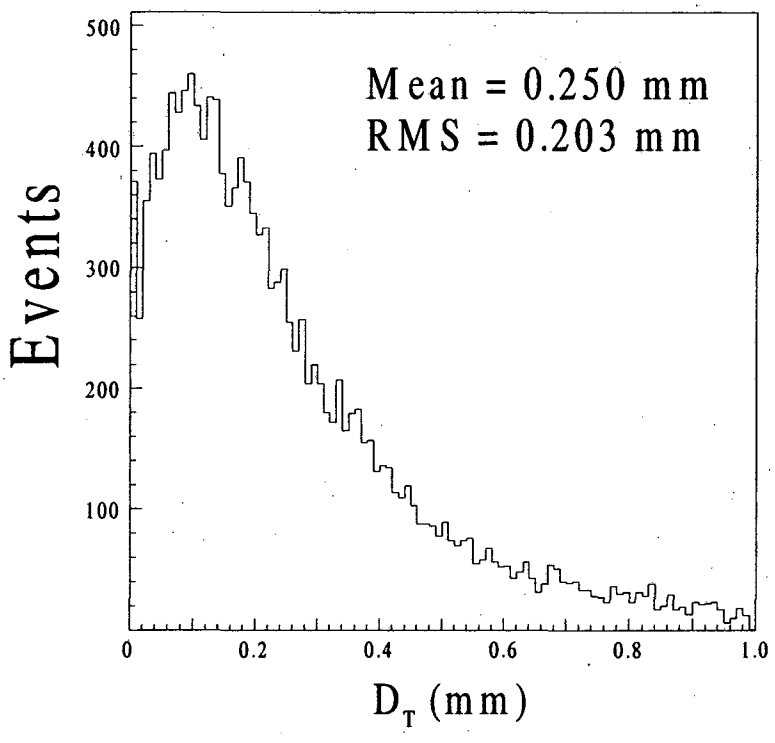

Figure 4.4: Distribution of the total deviation from a single interaction with an energy of 662 keV throughout the volume of the detector. The mean and RMS deviations of the distribution are shown.

In general, the algorithm's performance in locating a single 662 keV interaction is consistent with that predicted in the single-interaction position sensitivity study with a mean deviation substantially less than 1 mm. However, two important factors must be reiterated. First, the results were obtained by limiting the algorithms search to a single interaction. Secondly, simulated pulse shapes were used in the study not those of actual experimental measurements. Therefore, differences between simulation and experiment are not taken into account.

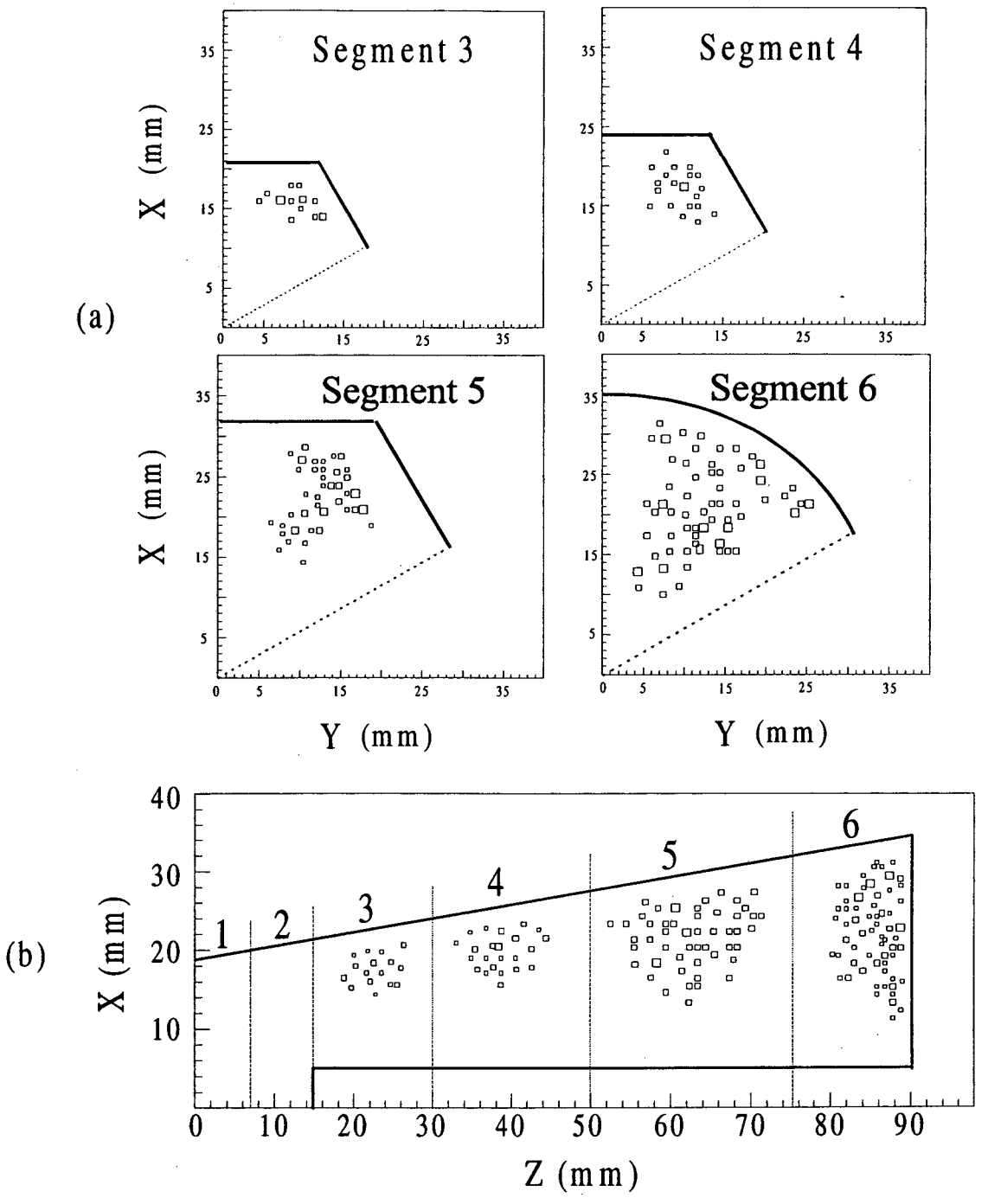

Figure 4.5: Distributions in the XY (a) and XZ (b) projections of positions having a total deviation greater than 0.5 mm. Note that the dashed lines show the segment boundaries and the size of the squares indicate the relative occurrence in the region.

4.2.2 Two Interactions

γ rays in the energy range of interest, which are incident upon the prototype detector, will most likely undergo multiple interactions. Therefore, it is necessary that the algorithm have the ability to decompose such events. This is achieved by simply increasing the value of k in the current algorithm. As an example, setting k = 2 requires the algorithm to search the parameters of two interactions (i.e. E_1, x_1, y_1, z_1 and E_2, x_2, y_2, z_2). It is important to point out that the algorithm will search for the best solution using the available parameters regardless of the actual number of interactions comprising the input simulated or experimentally measured pulse shape. This causes a problem because the number of interactions comprising an experimentally measured event is not known a priori. Obviously, if the input pulse shape was the result of more than the k interactions allowed there is no way that the algorithm could return the correct position and energy of all the interactions. However, if the input pulse shape was the result of less than k interactions the algorithm has the ability to return the correct solution. This would be achieved by returning zero for the energy of unneeded interactions (i.e. for a single interaction with k = 2 the correct solution would have E_2=0). One method to deal with such a problem would be to set the value of k much larger than is probable for the number of interactions. As will be discussed further at the end of this section, the added complexity due to the increased number of search parameters make this approach unfeasible and a compromise must be reached.

In order to access the algorithms performance in searching multiple sets of parameters, a simple scenario was again chosen. The same set of simulated pulse shapes as in 4.2.1 resulting from single 662 keV interactions throughout the volume of the

detector with the added noise were input to the decomposition algorithm. However, the number of interactions to be searched was increased to two. This allows for two possible outcomes of the decomposition process. One would be that the algorithm's solution is a single interaction. This is achieved when the fractional energy returned at that location equal to one. Conversely, both fractional energies may be nonzero, thus resulting in a solution with two interactions. Ideally, the algorithm should only return single interactions in this case. However, in reality both of the outcomes occur.

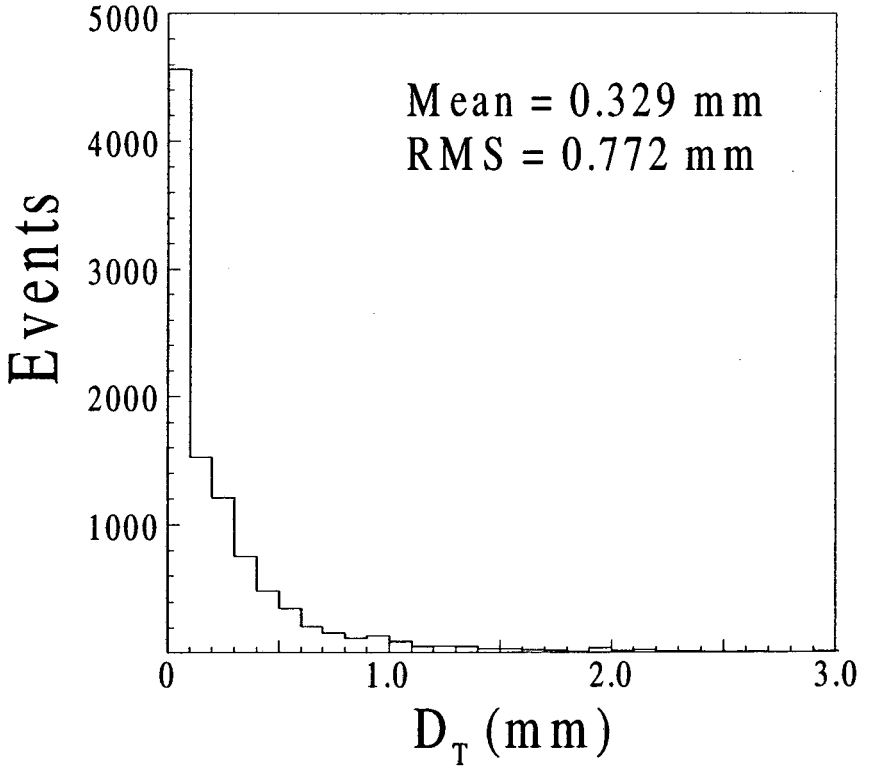

Figure 4.6: Distribution of the deviation between the input pulse shape position and that return by the algorithm for the cases in which a single interaction was returned. The mean and RMS deviation is indicated for the distribution.

For approximately 80% of the simulated events input, the algorithm returns a single interaction. Figure 4.6 shows the distribution of the total deviation (D_T) between the input pulse shape position and that return by the algorithm for the cases in which a single interaction was returned. The mean and RMS deviations are in fair agreement with those obtained when the algorithm search was limited to a single interaction (see Figure 4.4). This indicates that the accuracy with which the algorithm returns the position was not greatly effected by expanding the number of search parameters. What is effected, however, is the algorithm's ability to determine that a single interaction occurred.

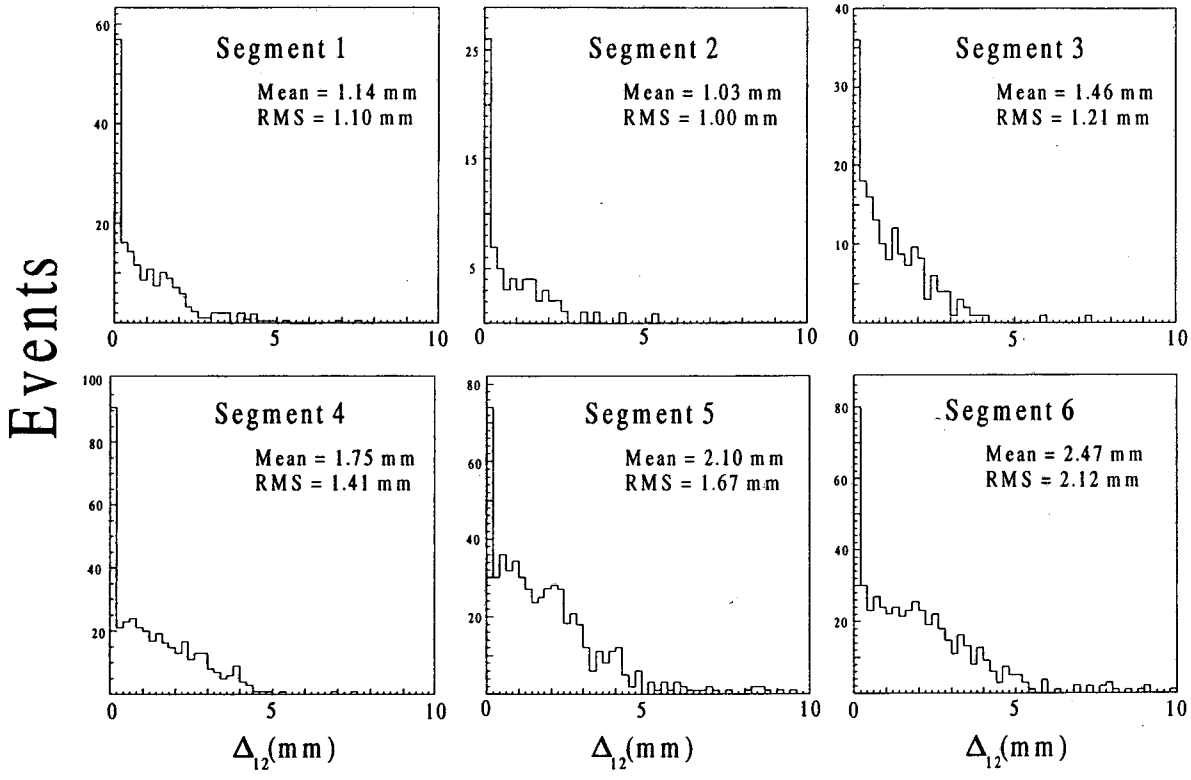

Figure 4.7: Distributions, grouped by segment, of the separation between the positions returned by the algorithm when two interactions were found. The mean and RMS deviations are indicated for each distribution.

By further examining the events in which two interactions were found, the reason for this failure was found to be related to the sensitivity of the pulse shapes rather than an intrinsic fault in the algorithm. Several factors lead to this conclusion. First, the frequency that the algorithm returns two interactions is related to the size of the segment. The percentage of these events range from about 14% in segment 2 up to about 23% in segment 6. This indicates that it is less likely to misinterpret the number of interactions in smaller segments where pulse shapes have greater sensitivity. Secondly, in nearly all failed events, the position of the actual single interaction lies somewhere between the two interaction positions returned by the algorithm. By examining the separation distance of the two returned positions a comparison can be made to the two-interaction position sensitivity study in Section 3.3.2. To illustrate this, Figure 4.7 shows distributions, grouped by segment, of the separation (Δ_{12}) between the positions returned by the algorithm when two interactions were found. The mean separation $\overline{\Delta}_{12}$ and RMS deviations are indicated for each distribution. As a means of comparing these results with those obtained in the position sensitivity study, Table 4.1 lists $\overline{\Delta}_{12}$ and the mean separation required to distinguish the two interactions totaling 662 keV obtained in the sensitivity study, $2\sqrt{\overline{S_T}}$. The values are in close agreement for each of the segments. This indicates that the algorithm's inability to distinguish the pulse shape resulting from two interactions with that of the single interaction is likely related to the sensitivity of the pulse shapes themselves.

Segment	$\overline{\Delta}_{12}$ (mm)	$2\sqrt{\overline{S}_T}$ (mm)
1	1.14	1.36
2	1.03	1.02
3	1.46	1.57
4	1.75	1.91
5	2.10	2.22
6	2.47	2.20

Table 4.1: Mean separation ($\overline{\Delta}_{12}$) between interactions when two are returned by the algorithm and the mean separation required to distinguish the two interactions totaling 662 keV obtained in the sensitivity study ($2\sqrt{\overline{S}_T}$) for each segment.

Additional features of the failed events are revealed when they are examined on an event-by-event basis. Figure 4.8 shows XY projections of segments 4 and 5 indicating four typical failed events (two in each segment). It is important to note that similar events occur with separations in the z-direction. The open square represents the actual position of the interaction and the two filled squares near each event show the positions returned with the corresponding E_1 and E_2. These events illustrate two features that are commonplace in the failed events. The first feature is that the failed events tend to be located near the center of the segments in regions where the pulse shapes are less sensitive. This further emphasizes the failure's relation to position sensitivity. The second is that the distance of each returned position from the actual position tends to be proportional to the fractional energy at that position (e.g. the position returned with the

larger value of E is closer the actual position of the interaction). This will be discussed further in the following section.

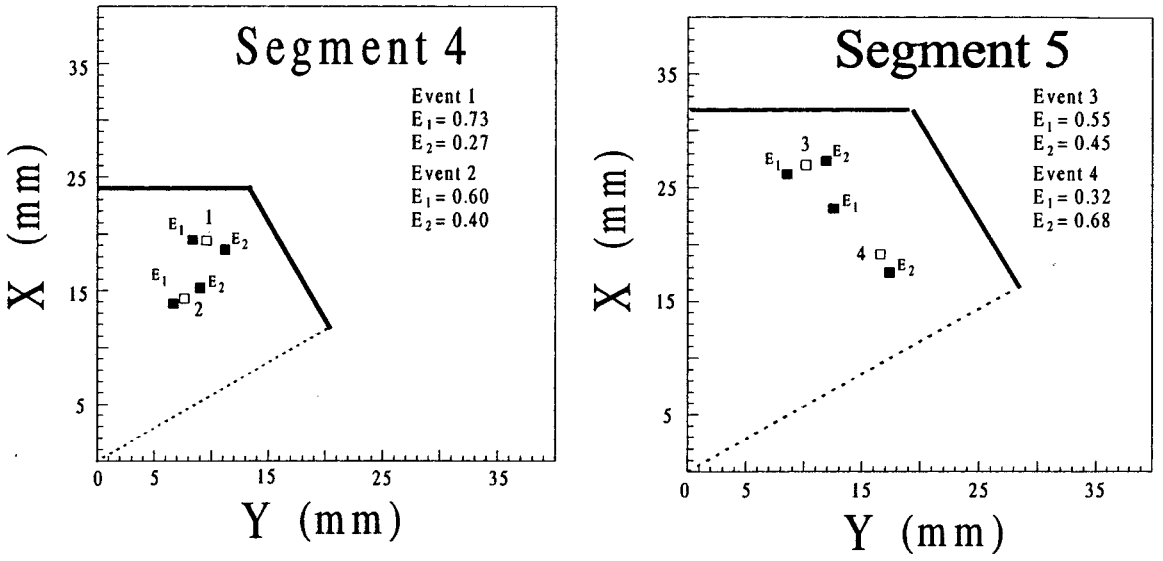

Figure 4.8: XY projections of segments 4 and 5 indicating four separate failed events (two in each segment). The open squares represent the location of the single interaction input and the solid squares nearby are the locations returned. The relative energy of the two interactions is indicated for each event.

Although the previous simulations were performed with pulse shapes from single interactions, the same features in the algorithm's performance are present when a pulse shape from two interactions occurring in a single segment is input. In this case, however, a failure results in the algorithm returning a single interaction at a location between the two actual interactions. Analysis of these simulations is much more complex. Here, the algorithm performance depends not only on the location of the two interactions but also

their energy ratio, separation distance and direction of separation. In general, the performance of the algorithm in simulation of two interactions occurring in a single segment of the detector is consistent with the two-interaction position sensitivity study. As an example, it is more likely for the algorithm to identify the two interactions totaling 662 keV in a segment if their separation is greater than the mean given in Table 4.1 for that segment. On the other hand, if the separation is less than the mean it is likely that a single interaction between the two will be returned.

4.3 Discussion

A signal decomposition algorithm utilizing a general linear least squares minimization approach was developed and tested using simulated 662 keV events. The algorithm's performance when both one and two interactions were allowed in the search was consistent with the position sensitivity studies discussed in Chapter 3. The inability, in some cases, of the algorithm to distinguish a single interaction from that of two nearby and vice versa was shown to be related to the sensitivity of the pulse shapes rather than a fault in the algorithm. While, on average, the single 662 keV events simulated were located to better than 1 mm this should not be taken as the position resolution. The simulation does not take into account important effects such as the range of the primary electron, or agreement between calculated and experimentally measured pulse shapes. As will be shown Chapter 5, discrepancies in the results obtained from experimental measurements and simulations are present.

While the algorithm itself is quite simple, the search method is rather computationally intensive. This is not of concern for the experiments performed with the single prototype detector presented in this dissertation, however, it will be for the full implementation of GRETA. Processing the large quantity of data expected from GRETA will require a signal decomposition algorithm with a minimal amount of computation. Other methods, utilizing wavelet transformations and artificial neural networks are currently being investigated in the hopes of decreasing the computation required.

Several issues must be discussed with regard to the algorithm's performance and its use in the experiments presented in the following chapter. Foremost is the number of interactions in which the algorithm can effectively search. For the tracking experiments present in Chapter 5, the algorithm will be limited to the search for two interactions per segment. This was done because it was found that increasing the search to three interactions greatly reduced the success rate in finding both one and two interactions in a single segment. In this case, single interactions could be misidentified as two or three and two interactions as one or three. This reduces the success rate of finding two interactions because even in cases where the two interactions were separated by distances greater than that given in Table 4.1, they could be misidentified as three. In such cases, the algorithm would return one interaction location close to one of the input locations and two surrounding the other interaction location. It is important to note that these results are for interactions occurring in the same segment. It was found that if the interactions occurred in separate segments the algorithm maintained approximately the same success rate, as presented in Section 4.2.2, for finding each of the interactions. This is due to the

fact that the pulse shapes on both charge-collecting electrodes contain a great deal of position information.

The second issue regarding the algorithm's implementation in the experiments addresses the misidentification of a single interaction with that of two. In order to increase the success rate of identifying single interactions, two interactions found by the algorithm that were separated by less than 2 mm are taken to be one. This distance was chosen because it is the upper limit of the desired position resolution for GRETA. Additionally, the findings of the previous section show that in cases where two interactions are separated by less than 2 mm, the algorithm is likely to misidentify the event as a single interaction located between the location of the two. Therefore, when two interactions are returned with a separation less than 2 mm the energy of the interaction is taken as the sum of the two. From the findings of the previous section, it was shown that the distance of each interaction from the actual location is approximately proportional to their energy. Therefore, the location of the single interaction is taken at a position between the two weighted by their relative energy. This increases the success rate for identifying single interactions to approximately 92% at an energy deposition of 662 keV. The algorithm with these modifications will serve to decompose both measured and simulated pulse shapes from tracking experiments performed with the prototype detector and presented in the following chapter.

Chapter 5

EXPERIMENTAL MEASUREMENTS AND MONTE CARLO SIMULATIONS OF THE TRACKING PROCESS

The signal decomposition process, described in the previous chapter, provides the first step in the tracking of γ rays. Following such a process, additional algorithms are needed to reconstruct the path of the individual γ rays. The algorithm utilized for the full GRETA array must have the ability to separate groups of interactions belonging to single γ rays (in most cases multiple coincident γ rays will interact in the array), distinguish between γ rays that deposit their full energy in the array and those that deposit partial energy, and determine the sequence of interactions. Here, the full tracking process including signal decomposition will be conducted with both experimentally measured and simulated data from the prototype detector. The main difference between the tracking process for GRETA and the one employed here is that the current process lacks the ability to separate groups of interactions belonging to different γ rays. This is of little concern for a single detector with relatively small volume because it is unlikely that multiple γ rays from the sources used (and/or environment) will interact in coincidence within the detector. Therefore, the group of interactions returned in the signal

decomposition is assumed to belong to a single γ ray. An algorithm that includes methods for separating groups of interactions belonging to coincident γ rays for implementation with GRETA has been investigated and is described in reference 50.

The following Section provides a description of the tracking process used in the analysis of the experimental and simulated data. The tracking process described here will only be implemented to increase the peak-to-total ratio obtained in the energy spectrum from the prototype detector. The method by which this is accomplished will be described in Section 5.1. In Section 5.2, the experimental measurements performed using three different radioactive sources are described. In addition, the results obtained by implementing the tracking process are presented. The simulations of radiation transport and signal generation performed to model the experiment are presented in Section 5.3. In addition, comparison is made between the simulation results and that of the experiment. Finally, a discussion of the results is included in Section 5.4.

5.1 Principle of the Tracking Process

The dominant interaction mechanisms for γ rays with energies up to about 5 MeV are Compton scattering and photoelectric absorption. Since the γ ray sources utilized in the studies with the prototype detector had energies within this range, the tracking process employed is based solely on these two mechanisms. The process of pair production is not included. However, it is currently being investigated for incorporation into the tracking process utilized for GRETA. In either case, the heart of the tracking

process is based on Compton scattering. In the Compton scattering process, the energy of the scattered photon is related to the energy of the incident photon by the scattering angle according to Equation 2.2. As a photon makes successive Compton scattering interactions the relation holds true, within the limitations set by the Compton profile, until the scattering is terminated. It is the goal of the tracking process to reconstruct the sequence of Compton scattering interactions to determine if the energy measured in the detector was the full-energy of the incident photon. In order to demonstrate how the process works, each step is presented, pointing out the known and unknown information as well as the assumptions made during the process.

In the case of GRETA, the γ rays of interest come from the target location at the center of the array (the position of which will be known to an accuracy of better than 1 mm). A γ ray from the source incident upon the detector may make 0 to N interactions, the probability of which depends on the photon energy. As an example, take the case of a single γ ray with unknown energy emitted from the source that undergoes N interactions in the detector. The first step in the tracking process is to determine the number of interactions along with the position and energy deposited in each interaction. This requires that the pulse shapes from the detector, following the N interactions, be digitally recorded and input into the signal decomposition algorithm described in the Chapter 4. This process will return the positions and energies of M interactions that reproduce the pulse shape observed from the detector. Ideally $M = N$, however, as discussed in the previous chapter this may not always be the case.

Once the M interactions are returned, several assumptions need to be made in order to determine if they comprised the full-energy of the incident γ ray. The first is to

assume that the incident γ ray originated from the known source location. Secondly, assume that the M interactions comprised the full energy of the γ ray (E_γ) such that:

$$E_\gamma = \sum_{i=1}^{M} E_i \,, \tag{5.1}$$

where $E_1, \ldots, E_M$ are the energies deposited in each interaction. Lastly, assume that the M interactions where comprised of (M-1) Compton interactions followed by one photoelectric interaction. With these assumptions, the group of interactions can be compared against the energy-angle relation of the Compton scattering formula. Up to this point the exact sequence of the interactions is not known (i.e. whether any one given interaction was the first, second, ..., M-1 Compton interaction or the photoelectric interaction). Therefore, there are $M!$ possible sequences to be examined.

In order to compare each of the possible sequences, a figure-of-merit function (*FM*) is constructed that compares the calculated scattering angles θ_c (based on the Compton scattering formula and the energies deposited at each interaction), to the scattering angles measured θ_m (based on the positions of the interactions). For illustrative purposes, suppose that $M = 3$ and the interactions are referred to as i, j, and k with corresponding energy depositions of E_i, E_j, and E_k, respectively. In this case, the number of possible sequences P is equal to six (*i-j-k*, *i-k-j*, *j-i-k*, ect.) and a figure-of-merit must be calculated for each. In the first possibility, *i-j-k*, the incident γ ray from the source would have made its first Compton scattering at i followed by a second at j and a

photoelectric interaction at *k*. The *FM* can be calculated mathematically for this sequence as follows.

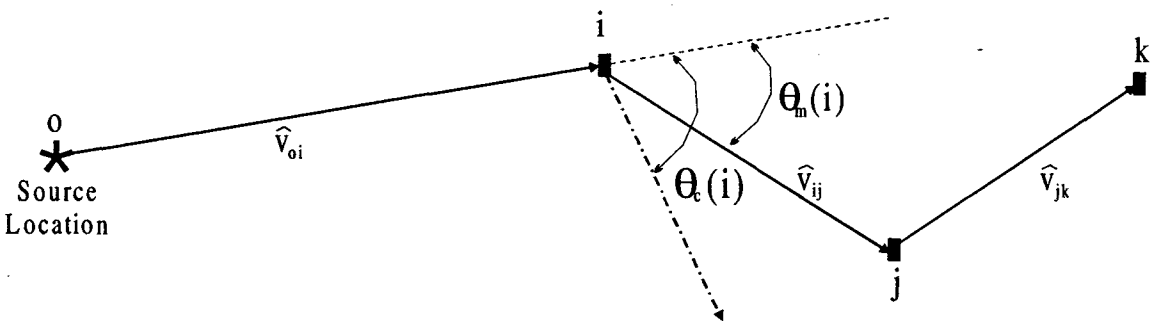

Figure 5.1: Schematic of the source location and interactions *i*, *j*, and *k*. The measured and calculated scattering angles at *i* are shown for the sequence *i*-*j*-*k* along with the relevant vectors.

First, the measured scattering angle θ_m at the first interaction in the sequence, *i*, is determined. This is found using the known source location and the locations of the first and second interactions in the sequence, *i* and *j*, determined in the signal decomposition process such that:

$$\theta_m(i) = \cos^{-1}(\hat{v}_{oi} \bullet \hat{v}_{ij}), \tag{5.2}$$

where $\hat{v}_{oi}$ is the vector from the source location to the first interaction *i* and $\hat{v}_{ij}$ is the vector from position *i* to the next interaction in the sequence *j*. Figure 5.1 illustrates the

location of each interaction and the respective vectors and scattering angles. Next, the calculated scattering angle θ_c at position i is determined using the energy deposited E_i returned in the signal decomposition in Compton scattering formula, whereby:

$$\theta_c(i) = \cos^{-1}\left(1 + \frac{m_o c^2}{E^*} - \frac{m_o c^2}{E^* - E_i}\right). \tag{5.3}$$

Here, $m_o c^2$ is the rest mass of the electron, E_i is the energy deposited in interaction i and E^* is the sum of the energy deposited in the interaction for which the scattering angle is calculated plus the remaining interactions in the sequence, $E^* = E_i + E_j + E_k$. The measured and calculated scattering angles are determined for each of the remaining interactions in the sequence, except for the last, in accordance with Equations 5.2 and 5.3. In this case, $\theta_m(j)$ is found using vectors $\hat{v}_{ij}$ and $\hat{v}_{jk}$, and $\theta_c(j)$ is calculated using E_j and $E^* = E_j + E_k$. The figure-of-merit for sequence *i-j-k* is defined as:

$$FM_{ijk}^{\ 2} = \sum_{i,j}\left(\theta_c - \theta_m\right)^2. \tag{5.4}$$

In general, the sum is performed over the first (M-1) interactions of the sequence using their respective θ_c and θ_m values.

This process is repeated to determine a FM_p for each of the six (M!) possible sequences (p = *ikj*, *jik*, ect.). The smallest FM_p, the smallest deviation between calculated and measured scattering angles, is chosen to represent the FM for the group of interactions. In a detector with perfect position and energy resolution, a γ ray from the

source that deposits its full-energy in the *M* interactions will have a *FM* of zero for the correctly associated sequence of interactions. In cases which the γ ray does not deposit all its energy in the detector, the sum energy of the *M* interactions will be less than its true energy and the Compton scattering formula will not be satisfied. In general, such events will have a non-zero *FM* allowing them to be separated from the full-energy events, thus, increasing the peak-to-total ratio of the detector.

In reality, a detector has a finite position and energy resolution. Therefore, even the correctly identified full-energy sequences will likely have a non-zero *FM*, and thus the separation of full- and partial-energy events is subject to some uncertainty. As an example, Monte-Carlo simulation of the radiation transport was performed for a 662 keV source located 12 cm from the front face of the prototype detector. For simplicity, the signal generation and decomposition were not included, but rather a 2 mm position resolution and 0.2% energy resolution for each of the Monte-Carlo simulated interactions occurring in the detector was assumed. The *FM*s where calculated for 10,000 events. Figure 5.2 shows the total distribution of *FM*s calculated for the events and the separate components of the full- and partial-energy events. As evident, the full-energy events are narrowly distributed at low *FM*s while the partial-energy events are distributed over a broad range of *FM*s. Therefore, placing a threshold on the *FM* can increase the ratio of full- to partial-energy events. However, there will be a trade off between the peak-to-total ratio and the fraction of full-energy events lost by placing the threshold. This relationship will be examined for both the experimental measurements and simulations presented in the following sections.

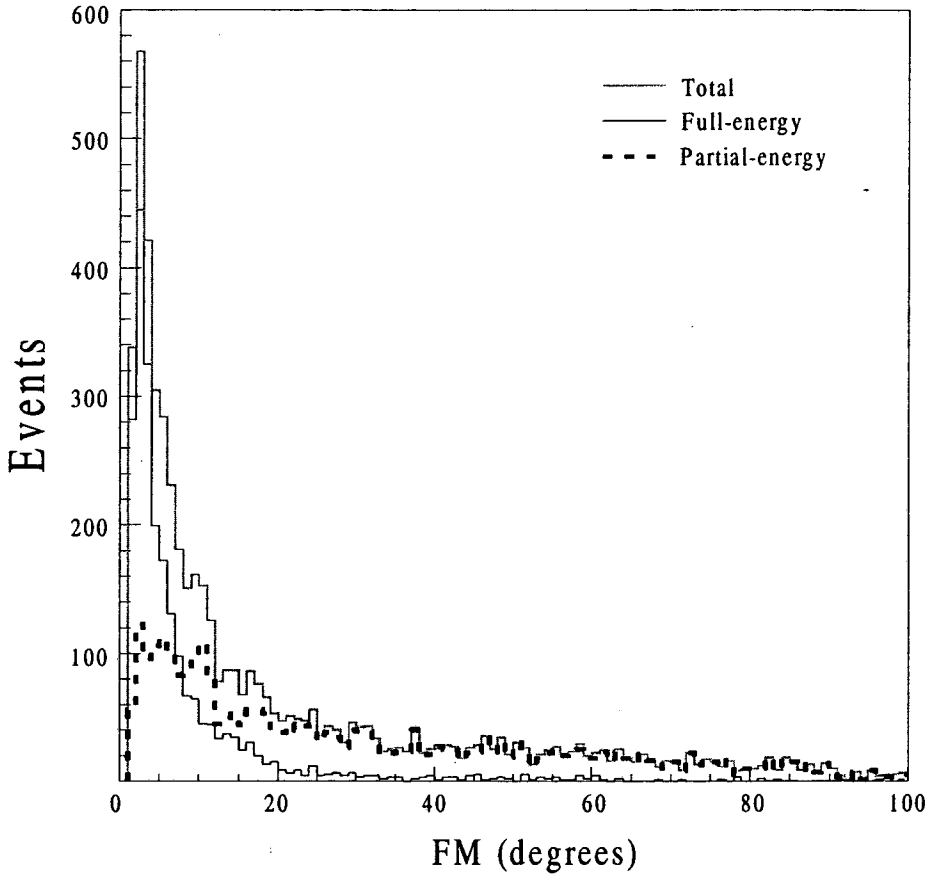

Figure 5.2: Distribution of FM's calculated from Monte Carlo simulation of 662 keV events with 2 mm position resolution and 0.2% energy resolution. The total distribution is separated into the full- and partial-energy components.

An additional point must be made in regards to the tracking process utilized in the following sections. For events in which a single interaction is found in the signal decomposition (i.e. $M = 1$) a *FM* clearly can not be constructed using this tracking process. Therefore, such events were considered to be Compton interactions (partial-energy deposition in the detector) and removed from the energy spectrum along with the events with *FMs* greater than the threshold value. Obviously, some of the full-energy

events will be lost having truly deposited their full energy in a single interaction. The fraction of these events depends on the γ-ray energy and at energies below about 200 keV this loss becomes more pronounced. This will be discussed further in the following sections.

5.2 Experimental Measurements with the Prototype Detector

5.2.1 Experimental Arrangement and Methods

Experimentally measured data were acquired from the prototype detector and analyzed for three different γ-ray sources (^{137}Cs, ^{60}Co, and ^{152}Eu). In each case, the arrangement used to acquire the detector pulse shapes and the methods of analysis were identical. The γ-ray sources were positioned 12 cm from the center of the detector's front face with an accuracy of about 1 mm. This distance was chosen because it represents the realistic target to detector distance for GRETA.

Several steps are required for full implementation of the tracking process following an event in the detector. First, the pulse shapes from each of the detector segments as well as the central-electrode must be digitally recorded following an event. To realize this, a 12 bit flash ADC system operating at 40 MHz manufactured by XIA was employed [28]. However, the system only provided digitization for 32 separate inputs. This did not pose a significant problem since five of the segments were not functioning properly at the time of the experiment (in addition to the three mentioned in Chapter 2, the preamplifier outputs of A6 and C6 were lost). Therefore, the central

electrode and 29 segment electrodes (A1-5, B1-6, C1-5, D1-5, E1-2, and F1-6) were chosen to be digitally recorded by omitting the nonfunctioning segments as well as some of their neighbors. The ADC digitizes the voltage at each of the inputs every 25 ns and stores the values in a memory buffer. The system is equipped with an internal trigger and following energy deposition in one or more of the input segments a 1.6 μs portion of the buffer, centered around the trigger time, is saved to a computer. In addition to providing the pulse shape itself, software included with the system allowed calibration and output of the energy measured at each of the inputs following an event. The digitized pulse shapes (as well as the energy) from each segment and central-electrode were recorded for each event.

Following acquisition of the pulse shapes, the data was sorted. The sorting process was necessary because the pulse shapes from all detector segments could not be digitized. This could lead to inaccuracies in the signal decomposition in the event an interaction takes place in a segment for which some of the neighboring segment pulse shapes are missing. In such cases, the valuable information in the transient pulse shapes would not be available. Therefore, only events in which the energy measured at the central contact (i.e. the entire crystal) matched that of the total-energy in segments A1-4, B1-5, C1-4, D1-2, E1, and F1-2 (i.e. those with neighboring segment pulse shapes) were taken. This, in effect, reduced the active volume of the prototype detector by about one half.

After the sorting process, the digitized pulse shapes from the segment electrodes were input into the signal decomposition algorithm. In order for the algorithm to accurately fit a set of modeled basis pulse shapes to those experimentally measured, the

two must be aligned in time. To ensure the alignment between the start-time of the experimentally measured and basis pulse shapes a constant fraction timing method was applied. This procedure is widely used for determining a reproducible start-time of a voltage signal and is well described in references 3 and 51-54. With the start-time determined, the experimental and basis pulse shapes could be aligned within the sampling time of 25 ns. This alignment will be discussed further in Section 5.4 with relation to errors arising in the signal decomposition. The experimental pulse shapes were then fit to the basis pulse shapes to return the positions and energies of one or more interactions. As discussed in the previous chapter, the algorithm had the ability to determine a maximum of two interactions for each segment in which energy was deposited. With the positions and energies of the interactions determined for each event, the remainder of the tracking process described in Section 5.1 was implemented to construct a *FM* for each event.

5.2.2 Results with ^{137}Cs Source

A ^{137}Cs γ-ray source was utilized in the experimental arrangement described in the previous section. In nearly all cases, decay of the source to ^{137}Ba is followed by the emission of a 661.7 keV γ ray. In addition, x-rays are emitted following internal conversion of ^{137}Ba with predominate energies of 32.5 and 36.5 keV. These x-rays, however, are well out of the energy range of interest for tracking and will be considered part of the background radiation. The full-energy of interest for this experiment will be only that of 661.7 keV.

Following the acquisition and sorting of numerous events, analysis was performed on approximately 12,000 events. As a means of comparison, a standard energy spectrum

for the events was constructed prior to the implementation of the tracking process. This was achieved by summing the energy deposited in the segments to obtain the total-energy deposited in each event. Therefore, this effectively represents the spectrum that would be produced by a standard non-segmented HPGe detector of equivalent size. Figure 5.3 shows the measured total-energy spectrum for all events. A peak at the full-energy of 661.7 keV is seen as well as two peaks at the x-ray energies of 32.5 and 36.5 keV atop the Compton continuum of partial-energy events. With this spectrum, the peak-to-total ratio (*P/T*) for the full-energy γ ray (i.e. 661.7 keV) is defined as:

$$P/T = \frac{N_p}{N_T}, \qquad 5.5$$

where N_p is the number of events in the full-energy peak and N_T represents the total number of events in the spectrum. Because the detector has a finite energy resolution, N_p is determined by integrating the number of events within a full-width at tenth-maximum (FWTM) of the full-energy peak. This yields a $P/T = 0.162 \pm 0.005$ for the 661.7 keV γ ray in the spectrum shown in Figure 5.3 (e.g. without any implementation of tracking).

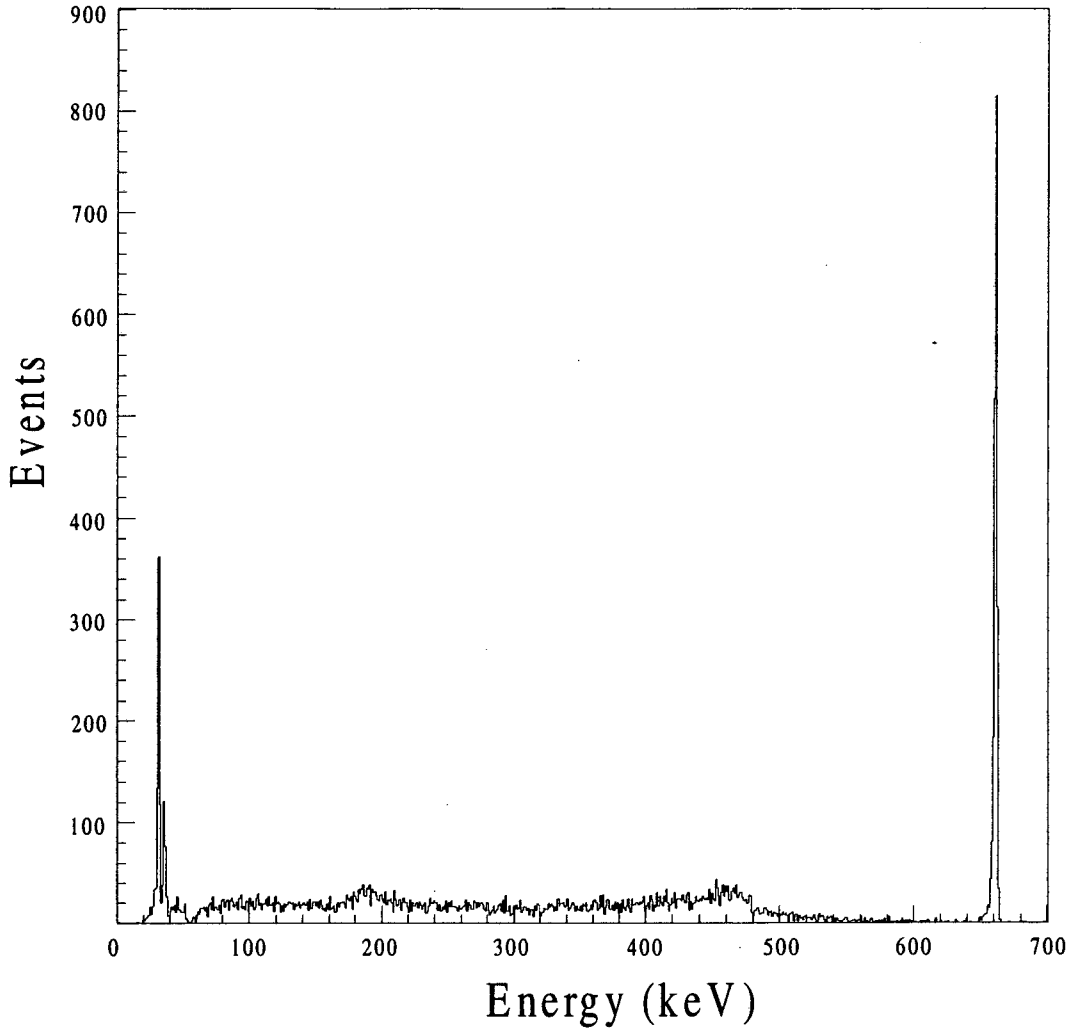

Figure 5.3: Total-energy spectrum for the 12,000 ^{137}Cs events. The two x-ray peaks at 32.5 and 36.5 keV can be seen along with the γ-ray full-energy peak at 661.7 keV.

The tracking process was implemented to construct *FM*s for the measured events. The goal, as discussed in Section 5.1, is to reject partial-energy events based on their *FM* and subsequently increase the *P/T* ratio. The distribution of *FM*s for the measured events is shown in Figure 5.4. The separate components for the full-energy and x-ray events (taken within a FWTM of each peak) are also shown. As expected the full-energy events

are concentrated at low *FM*s. The x-ray events, however, give rise to an increase in the *FM* distribution around *FM* = 55. The reason for this will be discussed later in this section.

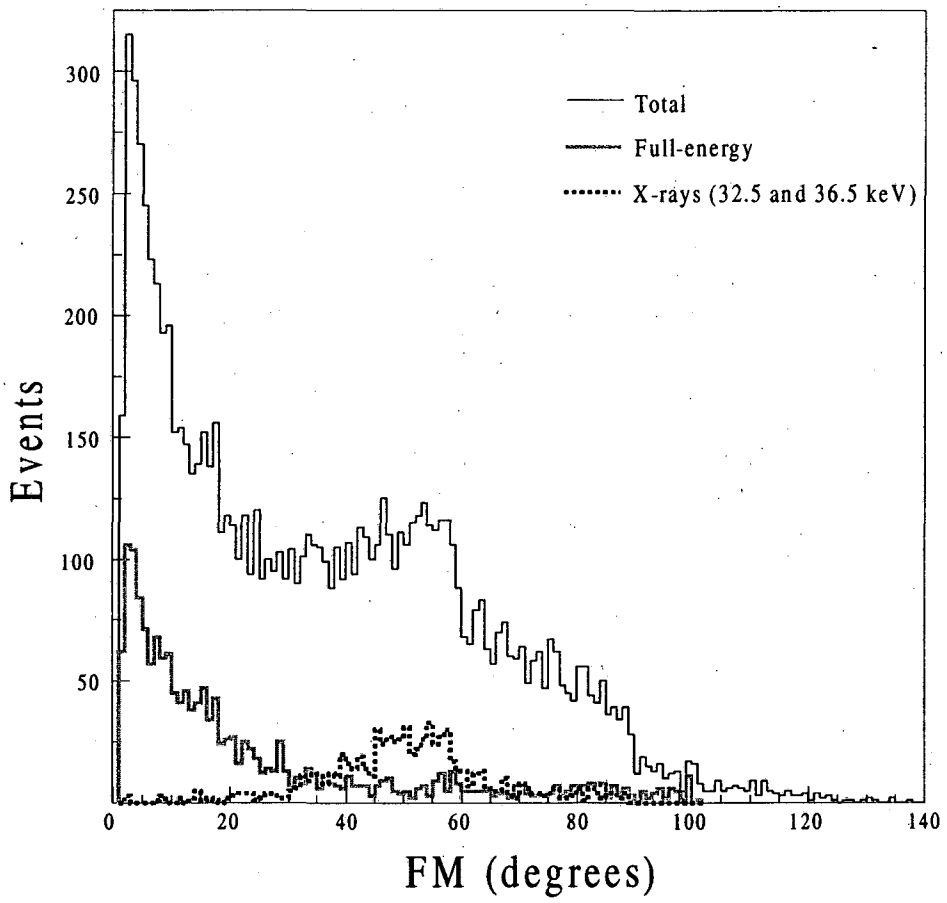

Figure 5.4: Distribution of FMs calculated in the ^{137}Cs experiment. The total distribution is separated into the full-energy component as well as that of the x-rays.

Any increase in *P/T* obtained by applying a threshold in *FM* will come at the expense of full-energy efficiency. In order to examine this trade-off and allow

comparison to the simulations presented in the following section, the relative efficiency is defined as:

$$\varepsilon_R = \frac{N_p}{N_p^*}, \tag{5.6}$$

where N_p is the number of events in the full-energy peak with a threshold in *FM* and N_p^* is the number of events in the full-energy peak without implementing tracking (e.g. that shown in the spectrum of Figure 5.3). Therefore, $\varepsilon_R = 1$ before tracking is performed. Once tracking is performed, ε_R immediately drops because events with a single interaction can not be tracked and are rejected.

In order to examine the *P/T* and ε_R relationship at the 661.7 keV γ ray energy, various threshold levels were placed on the *FM*. At each threshold, an energy spectrum was produced and the *P/T* ratio and ε_R were calculated. Figure 5.5 shows the relationship between *P/T* and ε_R. For reference, the *P/T* and ε_R without tracking are indicated as the data point to the far right on the graph. Starting at the right of the curve, the first data point indicates the removal of events with single interactions upon the implementation of tracking. As can be seen, ε_R drops to 0.87 ± 0.02 signifying that about 13% of the full-energy events were found to have a single interaction. However, the *P/T* rises from 0.162 to 0.181 ± 0.004, thus indicating that rejecting events having single interactions is beneficial to the *P/T* at this γ-ray energy. The data points, moving from right to left on the curve, indicate decreasing thresholds on the *FM* shown in Figure 5.4. The sharp

increase in *P/T* as the *FM* threshold is decreased signifies that partial-energy events can be preferentially rejected of the basis of their *FM*.

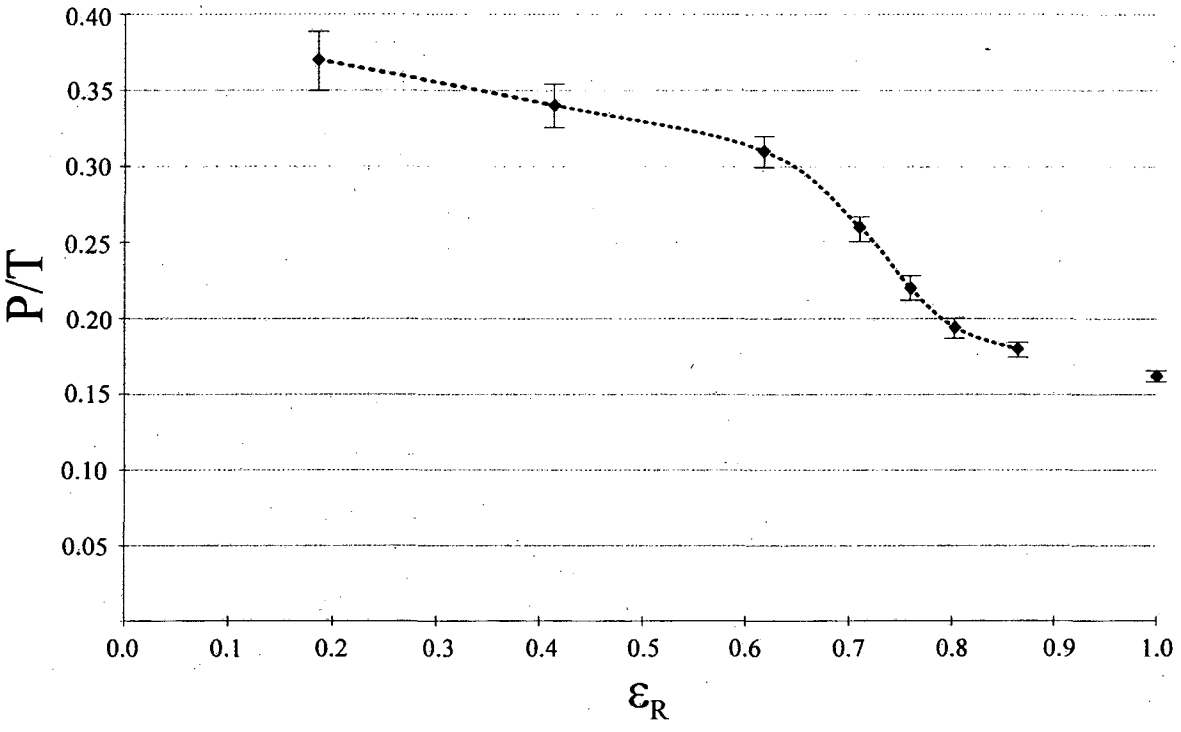

Figure 5.5: Relationship between P/T and ε_R in the ^{137}Cs experiment as thresholds are placed on the FM. The data point to the far right marks the P/T prior to tracking. Note that the error bars in ε_R are small relative to the point size.

To illustrate the gain in *P/T* in an energy spectrum, Figure 5.6 shows the energy spectrum for all events before tracking (same as Figure 5.3) and the energy spectrum after tracking for a *FM* threshold of 25. Note that the number of events in the full-energy peak for each have been normalized and the energy bins now have a 10 keV width. The

increase in *P/T* from 0.162 without tracking to 0.31 $\pm$ 0.01 is clearly evident in the reduction in the Compton continuum of partial-energy events. This comes with a change in ε_R from one to 0.62 $\pm$ 0.02. Additionally, it is important to point out the large reduction in the x-ray peaks. This is due to the fact that in approximately 70% of these events two interactions with a $FM > 25$ are found. The number of events found having two interactions is well above the predictions of the Monte-Carlo calculations. Therefore, it can be assumed that the majority of these events were truly single interactions that have been misidentified as two. This occurs because the events have a very low signal-to-noise ratio and thus greater flexibility of the fit parameters is allowed in the signal decomposition process.

The fact that the x-ray events are concentrated around $FM \cong 55$ (see Figure 5.4) is an artifact of the signal decomposition and tracking process. In the majority of these events, the signal decomposition process returns an energy ratio for the two interactions greater than that allowed in the Compton scattering formula (the maximum energy that can be deposited in a Compton interaction is only about 4 keV at the x-ray energies). In such cases, the energy ratio is assumed to be the maximum when the *FM* is calculated in the tracking process. This fixes θ_c (in Equation 5.4) to 180°. The θ_m values fall around 125° because the signal decomposition algorithm returns one interaction close to the initial search conditions, near the center of the segment, and the other close to the front face of the detector where the interaction is likely to have occurred (the mean free path of the x-rays is less than 1 mm in Ge). The failure of the signal decomposition process for the x-ray events is not of great importance because their energies are well outside of the interest range for tracking. However, it brings to light issues which may effect γ rays at

the lower end of the energy range, as will be examined in the ^{152}Eu source results in Section 5.2.4.

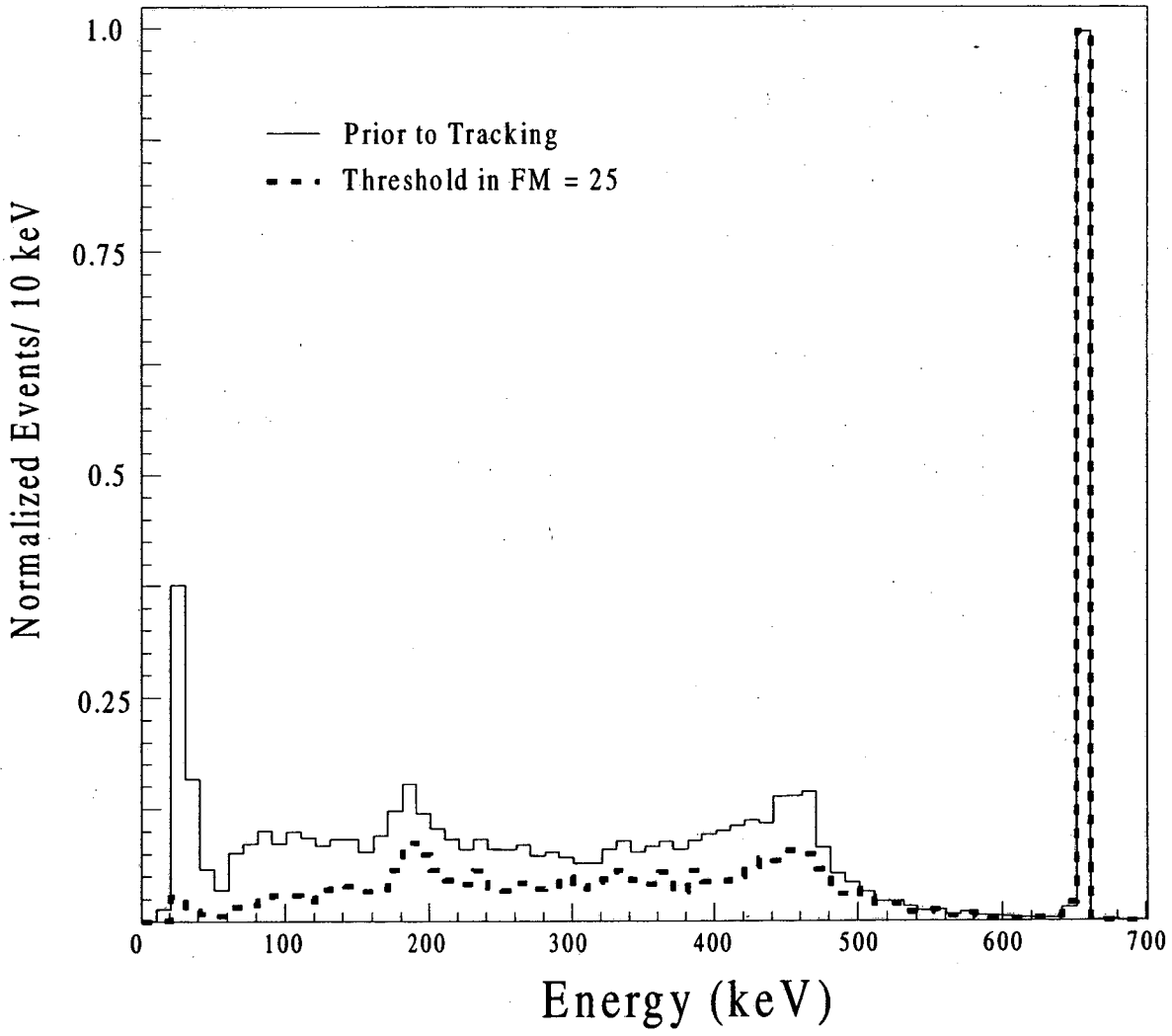

Figure 5.6: Total-energy spectrum for the 12,000 ^{137}Cs events experimentally measured prior to tracking (solid line) along with the energy spectrum after tracking for a FM threshold of 25 (dashed line). The spectra have been normalized to the number of events in the 661.7 keV peaks.

5.2.3 Results with ^{60}Co Source

The analysis performed on the experimental data measured using the ^{60}Co source was conducted in the same manner as that presented in the previous section. However, decay of the ^{60}Co source leads to the emission two separate γ rays with energies of 1.173 and 1.332 MeV. The peaks from both γ rays will be considered in the analysis, although due to their proximity in energy the results are very similar. Their energies vary significantly from that of the 661.7 keV γ ray discussed in the previous section and subsequent differences in the results will be pointed out.

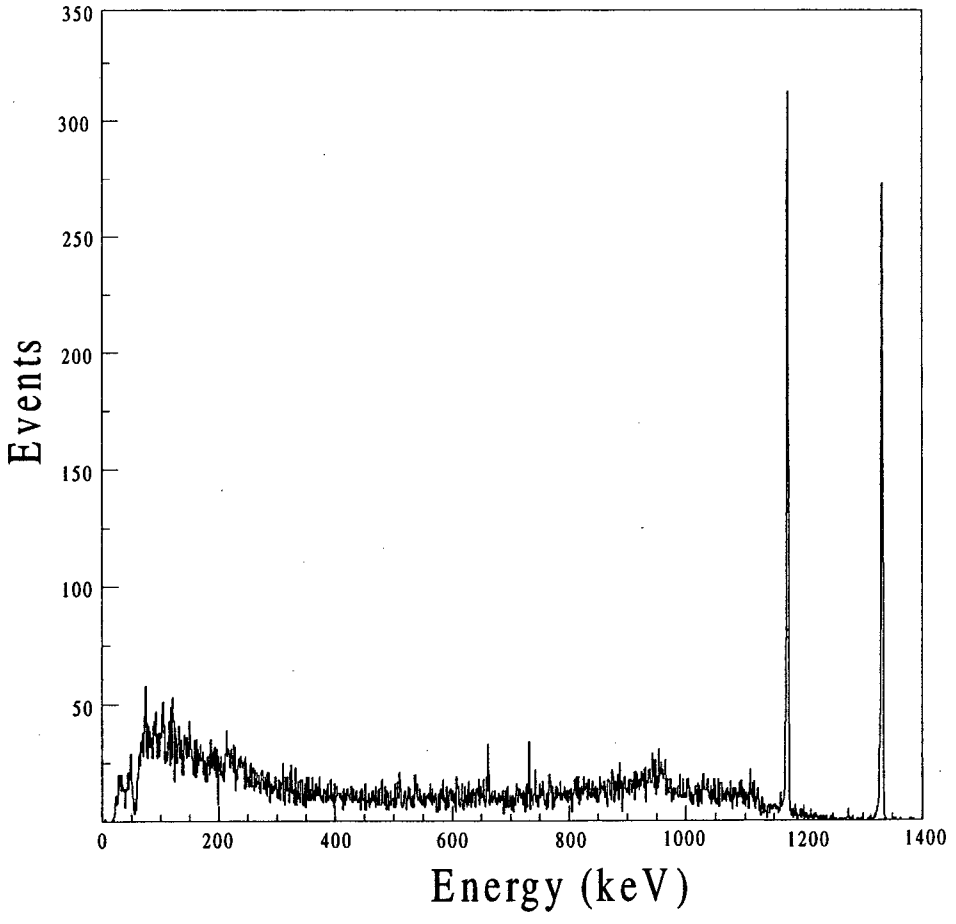

Figure 5.7: Total-energy spectrum for the 19,500 ^{60}Co events. The two γ-ray peaks at 1173 and 1.332 MeV can be seen.

A spectrum, prior to the implementation of tracking is shown in Figure 5.7. The *P/T* ratio was determined, in the same manner as previously discussed, for each full-energy peak resulting in values of 0.059 ± 0.002 and 0.049 ± 0.002 for the 1.173 and 1.332 MeV peaks, respectively. Because the γ rays are emitted with the same intensity, the difference in *P/T* stems from the decrease in efficiency for detecting the higher energy γ ray.

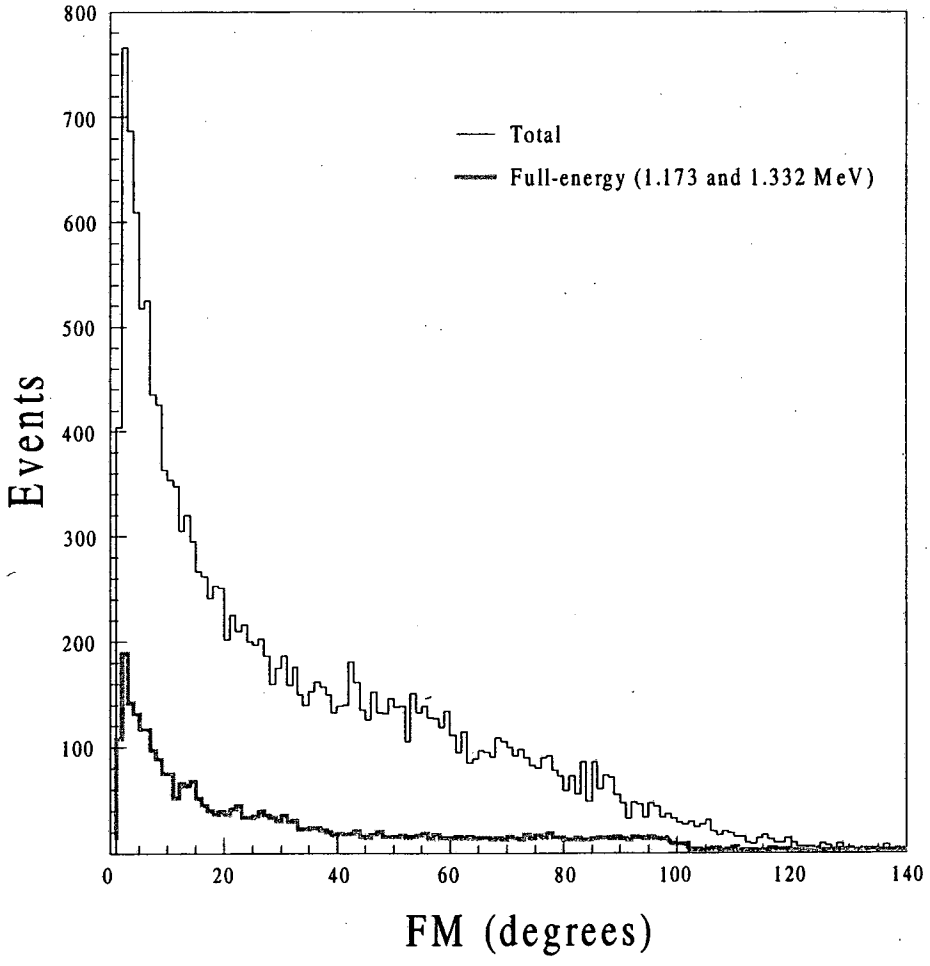

Figure 5.8: Distribution of FMs calculated in the ^{60}Co experiment. The total distribution is separated into the full-energy for both γ-ray peaks.

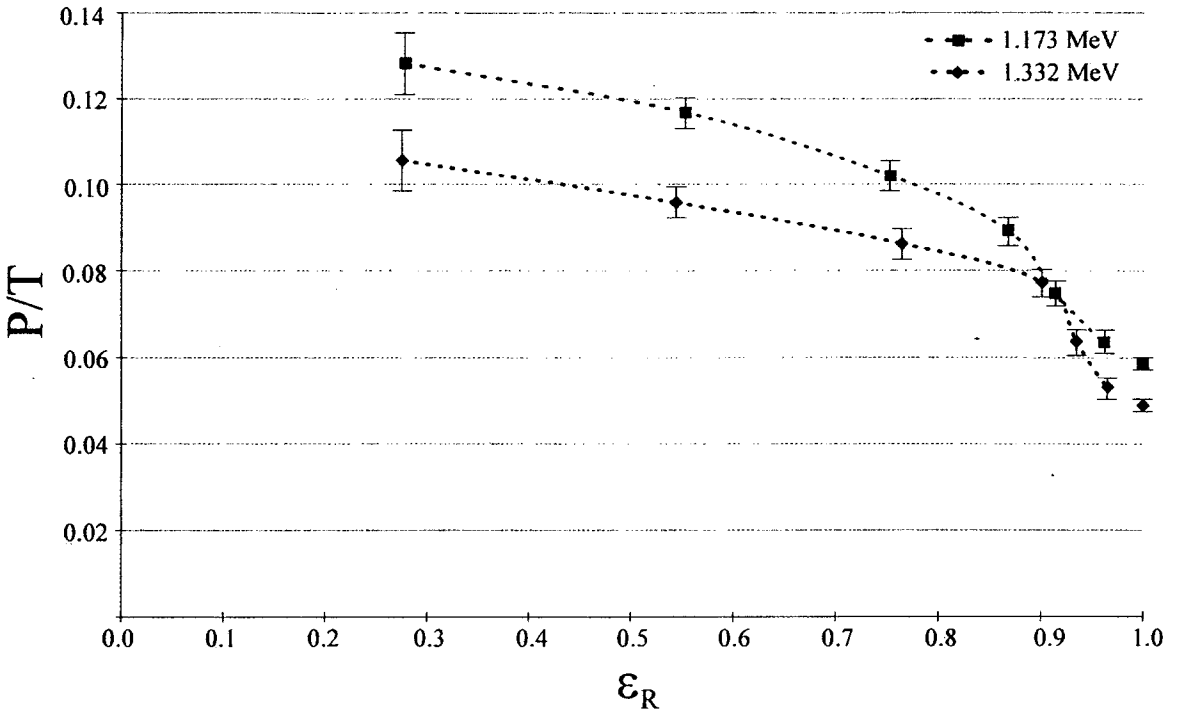

Figure 5.9: Relationship between P/T and ε_R in the ^{60}Co experiment as thresholds are placed on the FM. The data points to the far right mark the P/T ratios prior to tracking. for both the 1.173 and 1.332 MeV peaks. Again, the error bars in ε_R are small relative to the point size.

The tracking process was implemented for the 19,500 measured events and Figure 5.8 shows their distribution of *FM*s. Again, thresholds were set in the *FM* to illustrate the relationship between *P/T* and ε_R. Figure 5.9 shows the trade off for each of the γ-ray peaks. The two data points at ε_R = 1.0 mark the *P/T* ratios prior to tracking. Upon implementation of tracking, ε_R drops to 0.961 $\pm$ 0.002 and 0.965 $\pm$ 0.002 for the 1.173 and 1.332 MeV peaks, respectively. The percentage of single interactions rejected (i.e. 3.9% and 3.5%) at each energy is very similar, with slightly more at 1.173 MeV due to its lower energy. However, these values are much lower than in the case of ^{137}Cs reflecting

the reduction in the photoelectric absorption cross-section at 1.173 and 1.332 MeV as compared to 661.7 keV. In general, the curves follow the same pattern with an offset reflecting the initial difference in *P/T*.

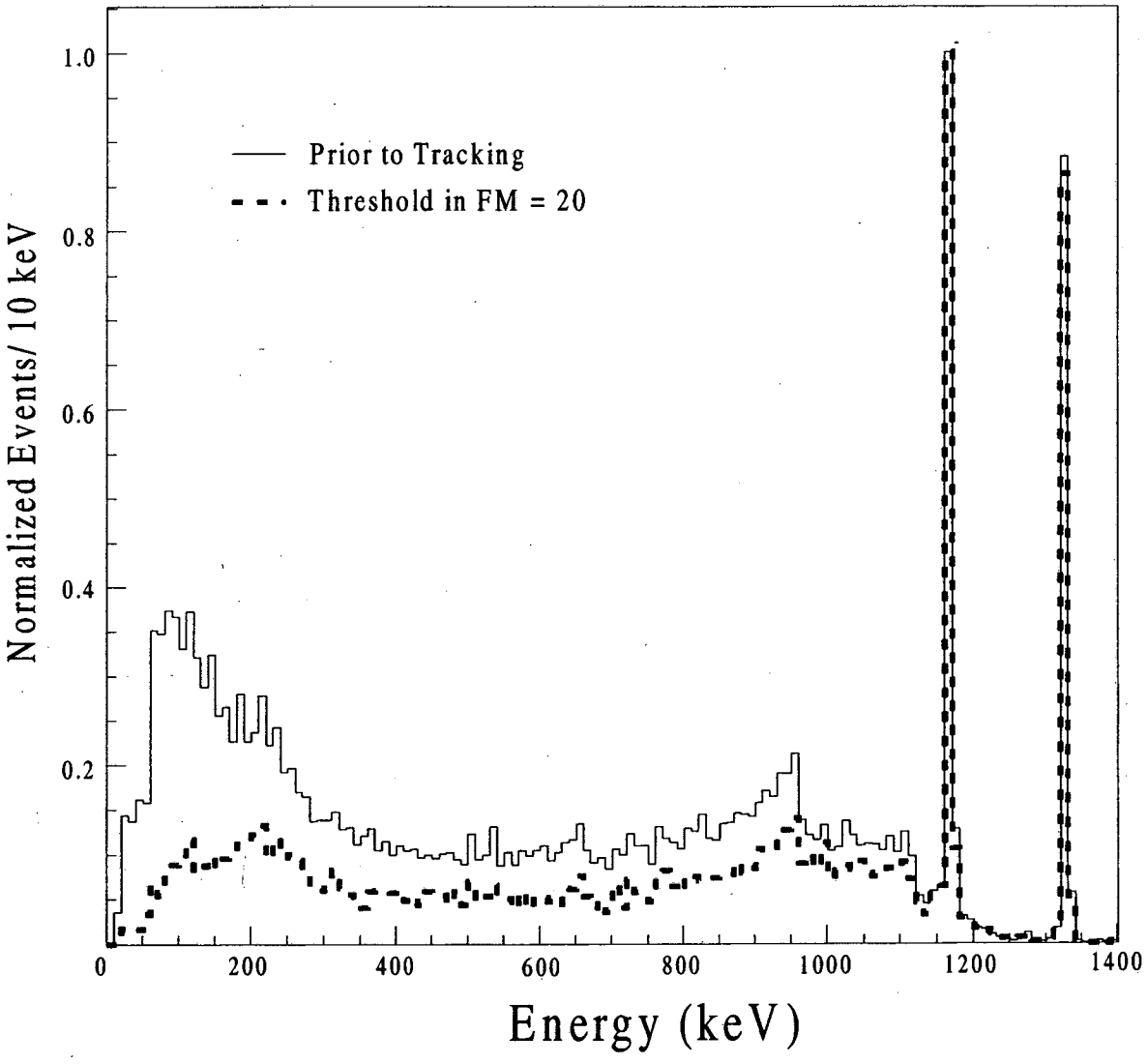

Figure 5.10: Total-energy spectrum for the 19,500 ^{60}Co events prior to tracking (solid line) along with the energy spectrum after tracking for a FM threshold of 20 (dashed line). The events in the 1.173 MeV peak for both spectra have been normalized to one.

To illustrate the *P/T* improvement in the energy spectrum, Figure 5.10 shows the energy spectrum for a *FM* threshold of 20 along with the total-energy spectrum prior to tracking. The spectra have been normalized to the number of events in the 1.173 MeV peak with energy bins 10 keV in width. A reduction in the Compton continuum is clearly visible with a change in *P/T* ratios from 0.059 and 0.049 prior to tracking to 0.107 ± 0.005 and 0.088 ± 0.004 with a threshold in $FM = 20$ for the 1.173 and 1.332 MeV γ rays, respectively. This comes with a change in ε_R from one to 0.71 ± 0.02 at 1.173 MeV and 0.70 ± 0.02 at 1.332 MeV.

5.2.4 Results with ^{152}Eu Source

Although ^{60}Co emits two γ rays, their energies are not separated enough to see a substantial difference in the ability to track each. Therefore, data was measured using a ^{152}Eu source. Decay of this source is followed by the emission of numerous γ rays with dominant energies ranging from 121.8 keV to 1.408 MeV. Figure 5.11 shows the measured spectrum of total-energy deposited in the detector for the 65,000 events recorded. Each peak is marked with the emitted γ-ray energy in keV. Note that the wide range in peak heights is due to varying emission probabilities for each γ ray in addition to their relative efficiency for detection.

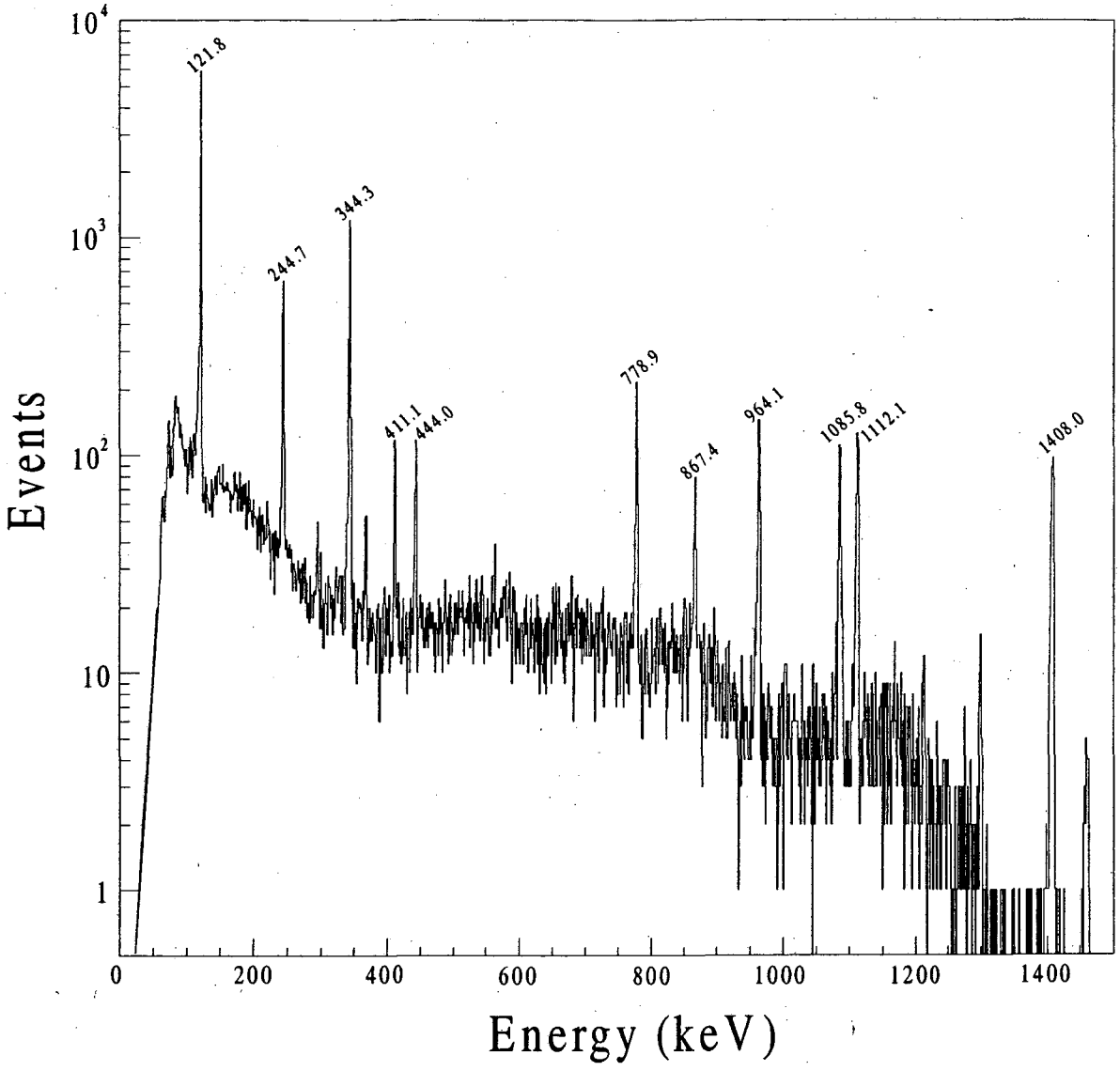

Figure 5.11: Total-energy spectrum for the 65,000 ^{152}Eu events plotted on a log scale. The dominant γ-ray peaks are marked with their energy in keV.

Figure 5.12 shows the distribution of *FM*s calculated for the events in the tracking process. As in the ^{137}Cs case, a rise is seen at about *FM* = 55. Although there are no x-rays present in the spectrum shown in Figure 5.11, the spectrum does have a large low-

energy component from the 121.8 keV γ ray contributing to the rise in the *FM* distribution. This feature will be discussed further in the following section.

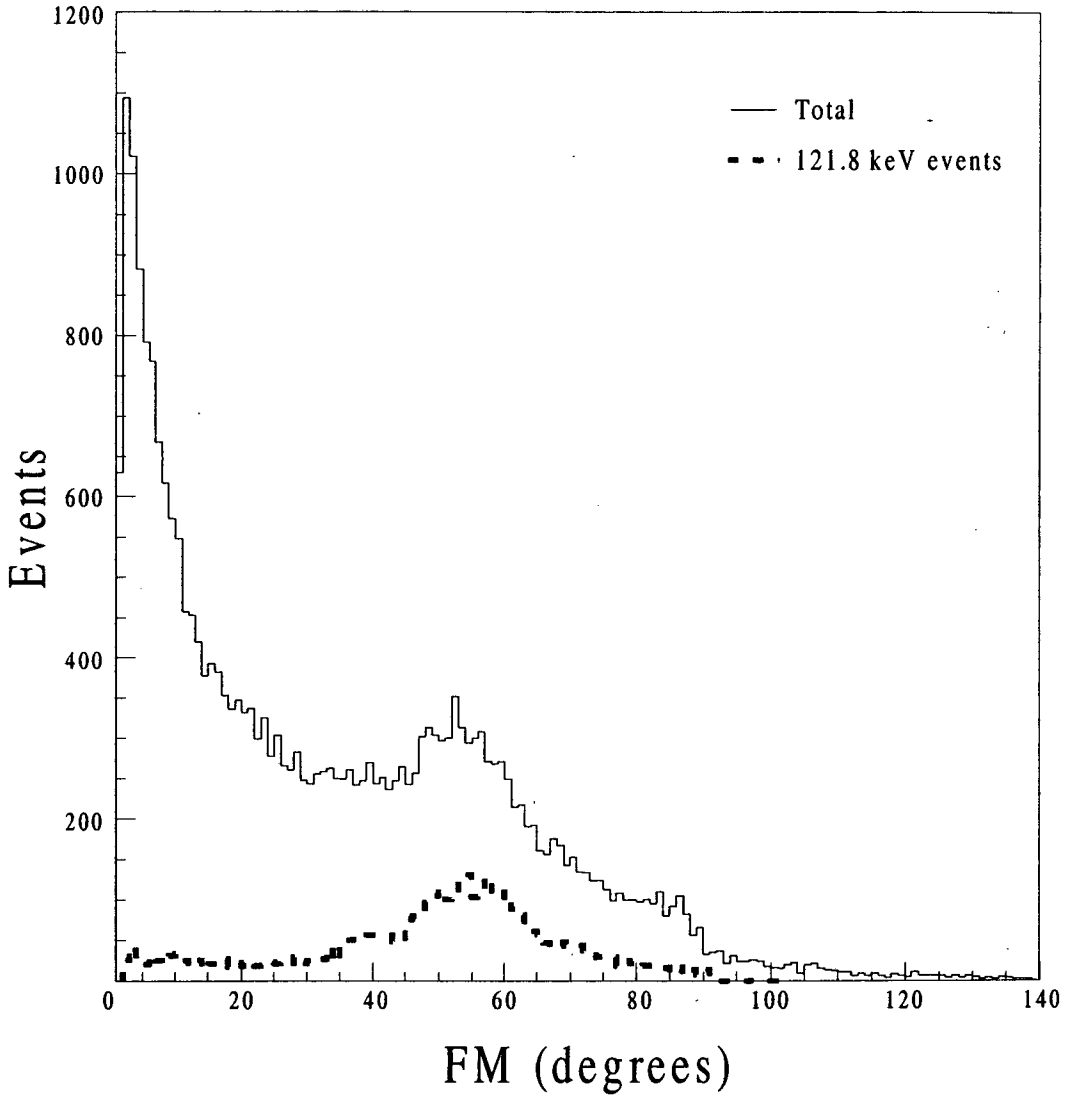

Figure 5.12: Total distribution of FMs calculated in the ^{152}Eu experiment. The separate component for 121.8 keV events, giving rise to the increase in the distribution around FM = 55, is also shown.

Again, it is important to examine the relationship between *P/T* and ε_R. Here, this can be examined as a function of γ-ray energy for the same spectrum. Since the various γ rays have a wide range of *P/T* values prior to the implementation of tracking, it is useful to plot this relationship using the gain in *P/T* rather the absolute *P/T* (as defined by Equation 5.5). The gain in *P/T* is simply defined as:

$$G_{P/T} = \frac{(P/T)}{(P/T)^*}, \qquad 5.7$$

where $(P/T)^*$ represents the peak-to-total ratio for a given γ ray prior to the implementation of tracking. Therefore, $G_{P/T} = 1$ at every γ-ray energy before tracking. Thresholds were placed in the *FM* to allow the $G_{P/T}$ verses the ε_R to be plotted for several of the γ-ray energies as shown in Figure 5.13. Upon the implementation of tracking ε_R drops, marked by the data point to the far right of each curve. Note that the drop in ε_R depends on the γ-ray energy and increases as the energy decreases. The increase in the number of single full-energy interactions found with decreasing γ-ray energy follows the increase in the photoelectric absorption cross-section. The removal of single interactions has a varying effect on the *P/T* ratio. At the higher γ-ray energies there is an increase in the *P/T* (i.e. $G_{P/T} > 1$) which decreases with the γ-ray energy until 244.7 keV at which point there is no substantial increase in the *P/T* (i.e. $G_{P/T} \cong 1$). At 121.8 keV the *P/T* is reduced having a $G_{P/T} < 1$.

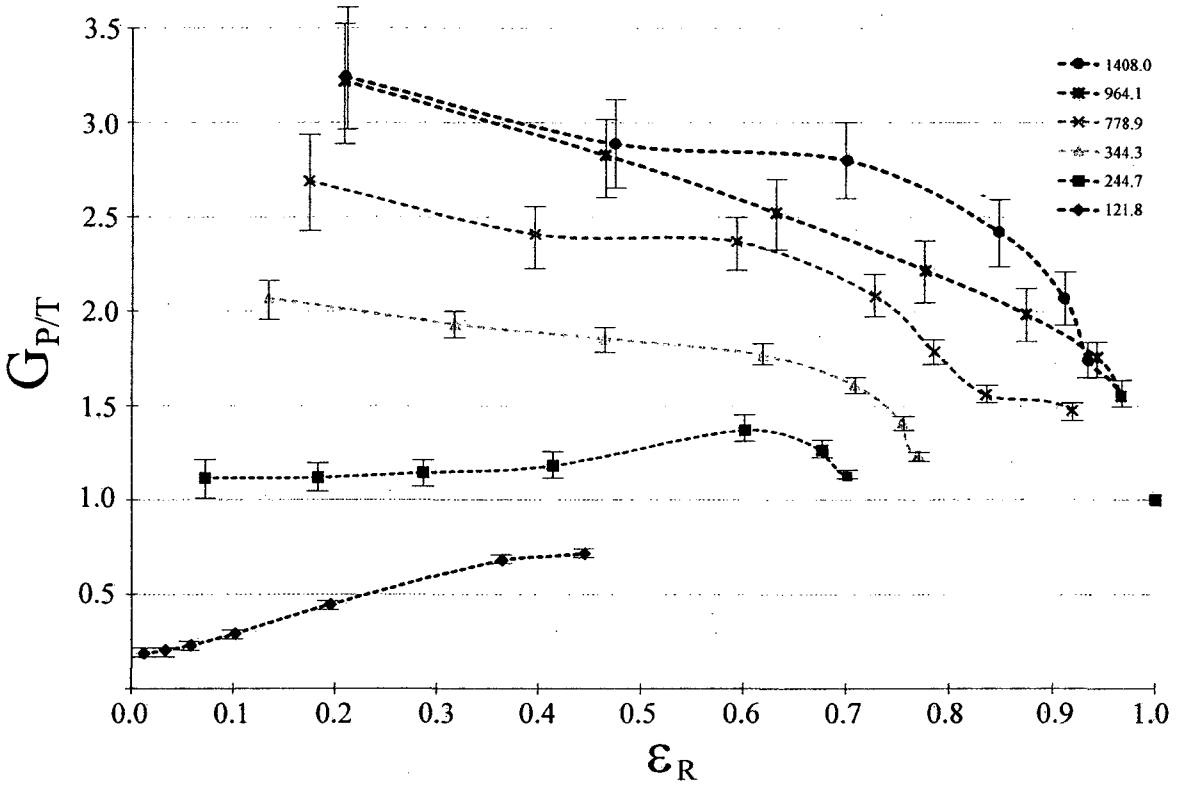

Figure 5.13: Relationship between the gain in P/T and ε_R in the ^{152}Eu experiment as thresholds are placed on the FM. The legend gives the energy of the g rays in keV with the associated data points. The data point to the far right marks the $G_{P/T}$ prior to tracking for all energies. The error bars in ε_R are small relative to the point size.

As the threshold in *FM* is decreased (i.e. moving right to left on the curves), the overall behavior of the $G_{P/T}$ as a function of γ-ray energy is clearly separable. The higher the γ-ray energy the larger the $G_{P/T}$ for any given *FM* threshold. There are two major

reasons for this behavior. First, higher energy γ-rays will, on average, have larger mean free paths for their scattered photons. Therefore, their interactions will be separated by larger distances and more easily distinguished from one another in the signal decomposition process. Secondly, higher energy γ-rays will deposit, on average, more energy per interaction, thus increasing the signal-to-noise ratio for these events. Again, this is beneficial to the accuracy of the signal decomposition process. In each case, this improves the full-energy *FMs* for higher-energy γ rays relative to those with lower energies. As is evident, there is not a significant gain in *P/T* from tracking until the γ-ray energy of 344.3 keV. At 121.8 keV the *P/T* actually decreases as the threshold in *FM* is decreased because of the two previously mentioned reasons. Due to the low signal-to-noise ratio of the 121.8 keV events, single interactions are easily mistaken for two in the signal decomposition process. Such events contribute to the rise in the *FM* distribution around *FM* = 55 (see Figure 5.12) because of the same reasons discussed for x-ray events in the case of ^{137}Cs. As the threshold is reduced, a large fraction of events at 121.8 keV are removed thus reducing the *P/T*. In addition, even correctly identified events that did undergo two interactions will likely have a *FM* that is larger than the higher γ-ray energies due to the proximity of the interactions.

5.3 Simulation of the Tracking Experiments

As a means of comparison with the experimental results presented in the previous section, the tracking process was performed using simulated pulse shapes. The simulations were performed by modeling the radiation transport and using the information to generate theoretically calculated pulse shapes. The same simulation procedure was employed for both the ^{137}Cs and ^{60}Co sources. First, the radiation transport was modeled using Monte-Carlo calculations performed with GEANT-3 [34] for the given experimental arrangement described in Section 5.2.1. This provided simulated interaction locations and energies within the detector for each event. Given the location and energy of each interaction, the detector pulse shapes were theoretically calculated for each event using the model described in Section 3.1 (with the sampling frequency adjusted to 40 MHz). To simulate measured pulse shapes, random noise was added to each modeled pulse shape. Figure 5.14 shows the distribution of noise experimentally measured on pulse shape samples from the ADC acquisition system. A Gaussian fit to the distribution yields a FWHM of 1.62 keV, and thus the same distribution of random noise was added to the simulated pulse shapes. The change in noise level, as compared to the 5 keV mentioned in the previous chapters, stems from the fact that a different acquisition system is employed here (i.e. a 40 MHz ADC as compared to a 500 MHz ADC).

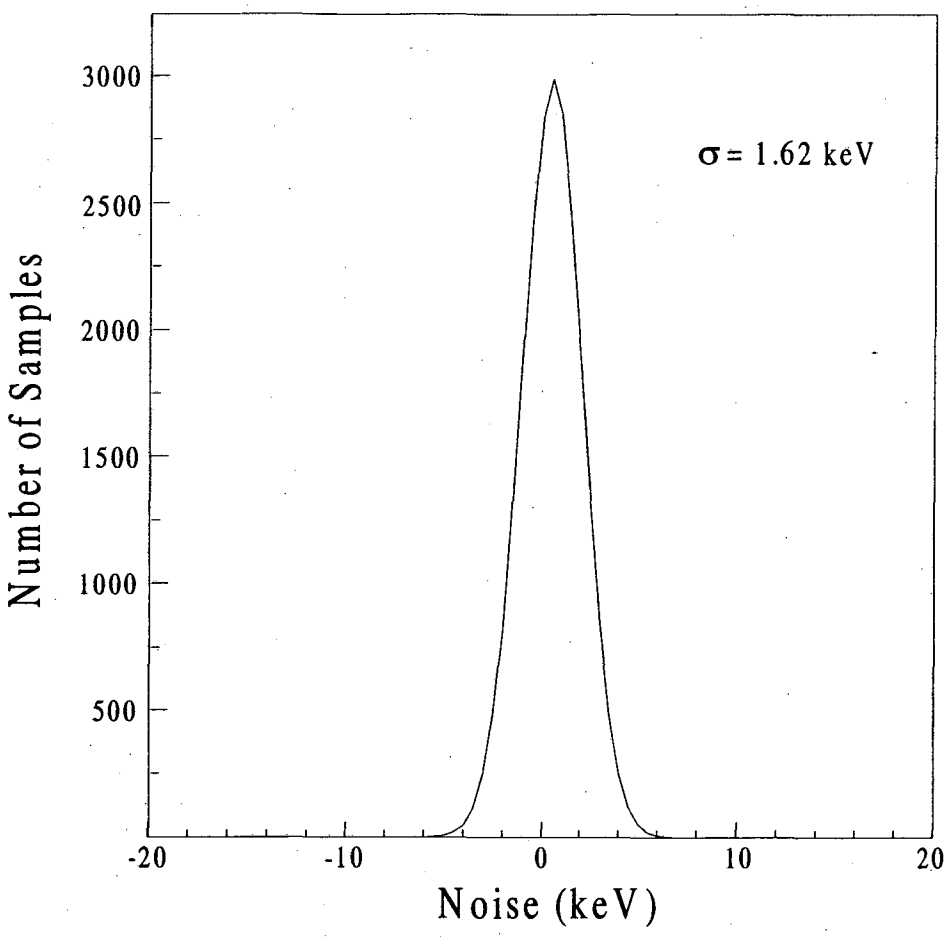

Figure 5.14: Distribution of the experimentally measured noise from detector pulse shape samples using the ADC acquisition system. The standard deviation, σ, is indicated for a Gaussian fit of the distribution.

To ensure the simulations accurately represented the experimental conditions, the events were sorted in the same manner described in Section 5.2.1. Therefore, only events interacting in the same functioning segments as in the experiment were excepted. These pulse shapes were then input into the signal decomposition algorithm. The algorithm fit the pulse shapes to the basis functions to return the interaction positions and energies for each event. The remainder of the tracking process, discussed in Section 5.1, was

employed to construct a *FM* from the positions and energies for each event. This allowed the analysis to be conducted in the same fashion as performed with the experimental data.

5.3.1 Results for the Simulation of ^{137}Cs and Comparison to Experiment

For the ^{137}Cs source, events were simulated from both the 661.7 keV γ ray emitted by the source as well as the two dominant x-rays. The number of sorted events used in the analysis was about the same as the experimentally measured events (e.g. 12,000). The energy spectrum, obtained by summing the energy returned in the signal decomposition process for each of the simulated events, is shown in Figure 5.15. For comparison, the measured total-energy spectrum prior to tracking (previously shown in Figure 5.3) is shown in the same figure. The overall shape of each spectrum is in good agreement with one another. The measured spectrum has a slightly larger Compton continuum, becoming more pronounced at lower energies. This difference is due primarily to inaccuracies in modeling the true physical properties of the environment around the detector (i.e. walls, floors, laboratory equipment, ect.) in the Monte-Carlo simulations. The presence of photons scattering in the environment and then into the detector adds to the background measured in the experiment. This is reflected in a slight difference in *P/T* for the simulation as compared to the experiment. A $P/T = 0.221 \pm 0.004$ for the simulated events is obtained prior to tracking where as the experimentally measured *P/T* was 0.162 ± 0.005.

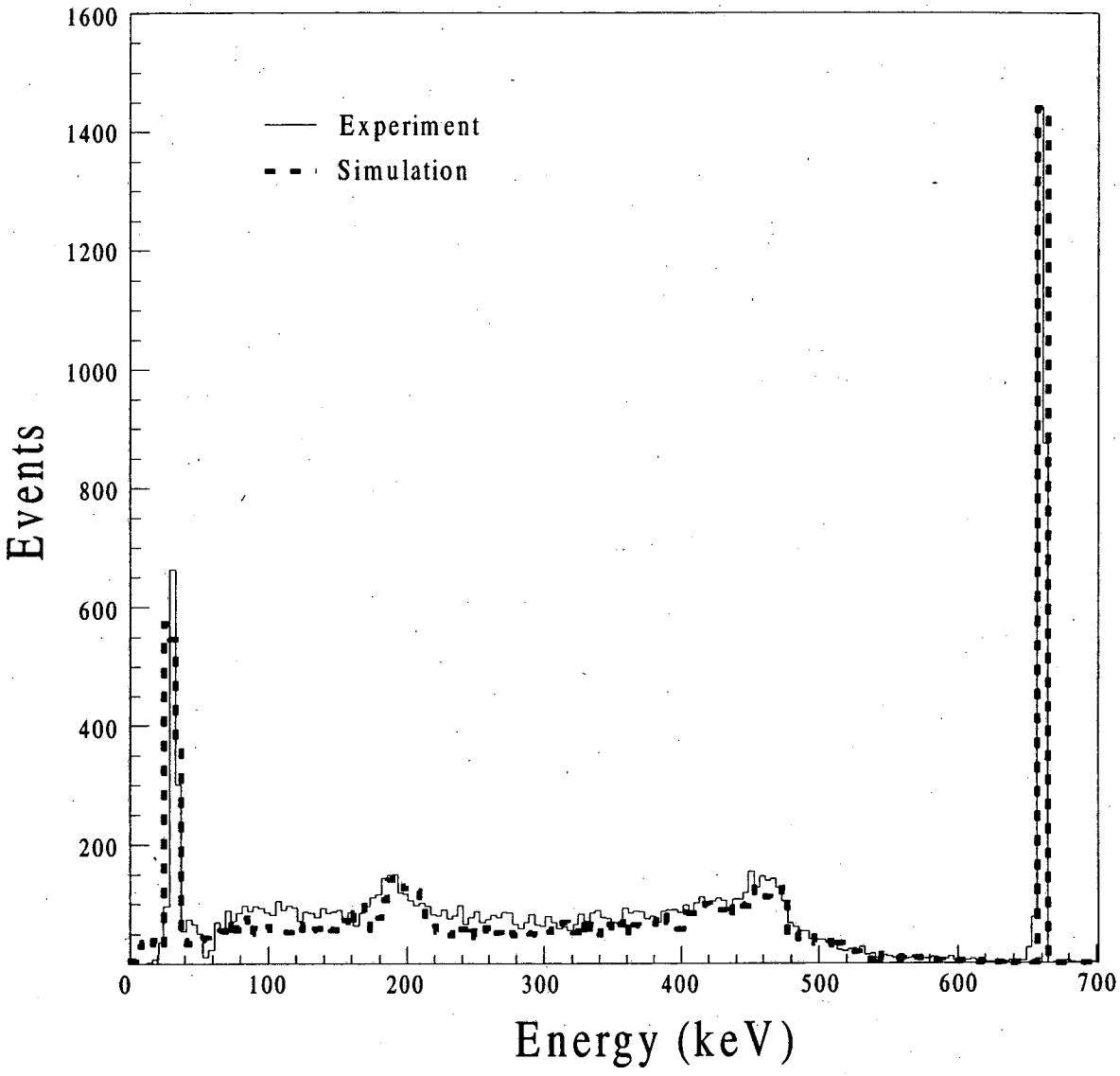

Figure 5.15: Total-energy spectrum for the 12,000 ^{137}Cs events prior to tracking for the experiment (solid line) along with the simulation (dashed line).

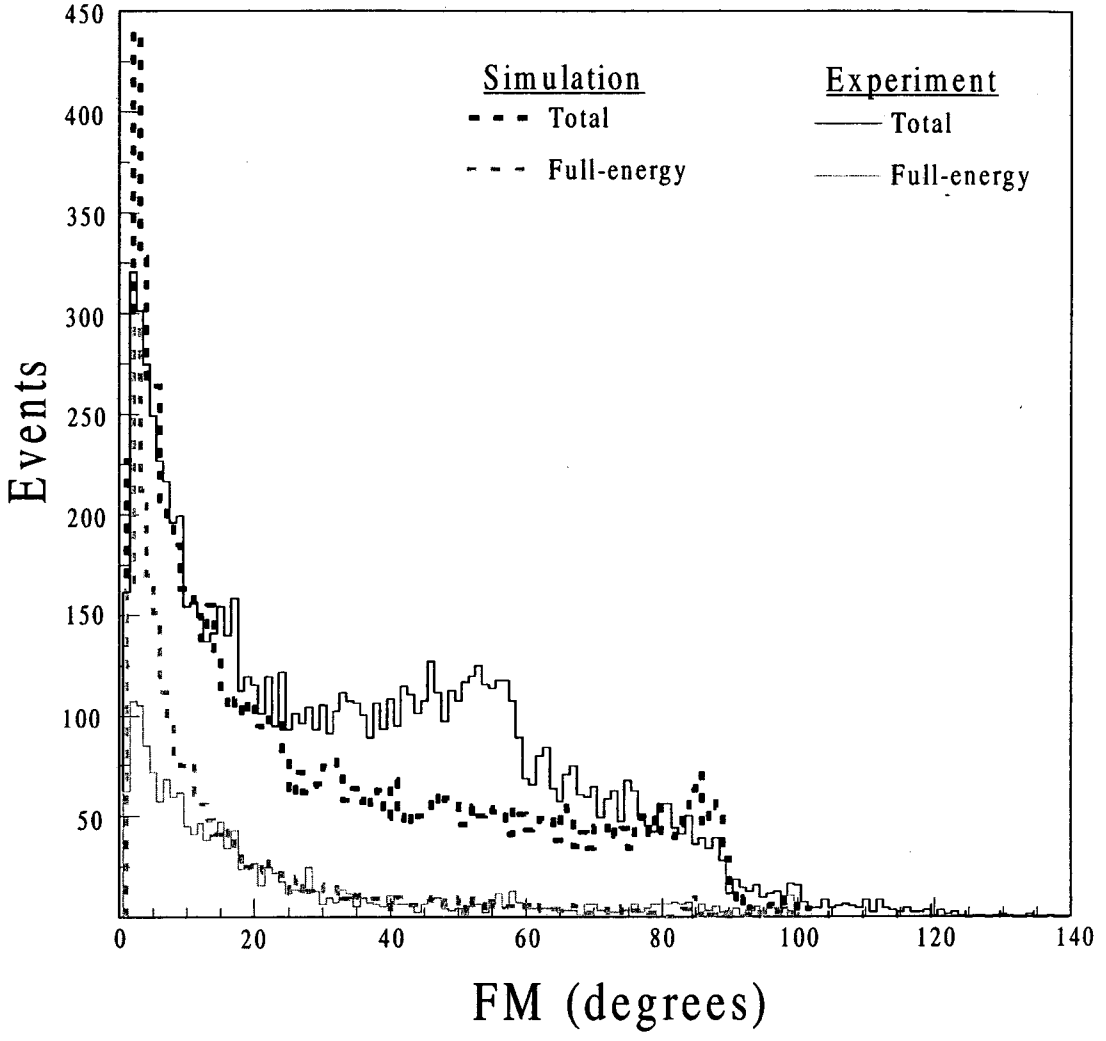

Figure 5.16: Distribution of FMs calculated in the ^{137}Cs experiment (solid lines) and the simulation (dashed lines). The total distribution is separated into the full-energy components for each.

The tracking process was implemented for the simulated events and the total distribution of *FMs* as well as the distribution full-energy *FMs* are shown in Figure 5.16. Again, the measured distribution is shown for comparison. The distribution of full-energy events in the simulation is narrower than that in the experiment. Several reasons for this will be discussed in the following section. Noticeably, the rise around $FM = 55$ in the total distribution of events is not as pronounced in the simulation. The number of x-ray events identified as having two interactions in the simulation is about 45%, as compared to approximately 70% in the experiment. The number of events identified as having two interactions in the simulation is well above the ~1% predicted in the Monte-Carlo calculations. Again, the reason is due to the very low signal-to-noise ratio of these pulse shapes. One possible reason for the larger misidentified fraction in the experiment may be discrepancies between the experimentally measured and calculated pulse shapes. As mentioned previously, the interactions from the x-rays occur very close to the outer-electrode surfaces of the detector. The electrical characterization of these regions can be rather difficult (see Section 3.2.3). Inconsistencies between the experimentally measured and modeled basis pulse shapes in these regions may contribute to the larger number of x-ray events being misidentified as two interactions in the experiment. This could give rise to the difference in the shape of the *FM* distributions.

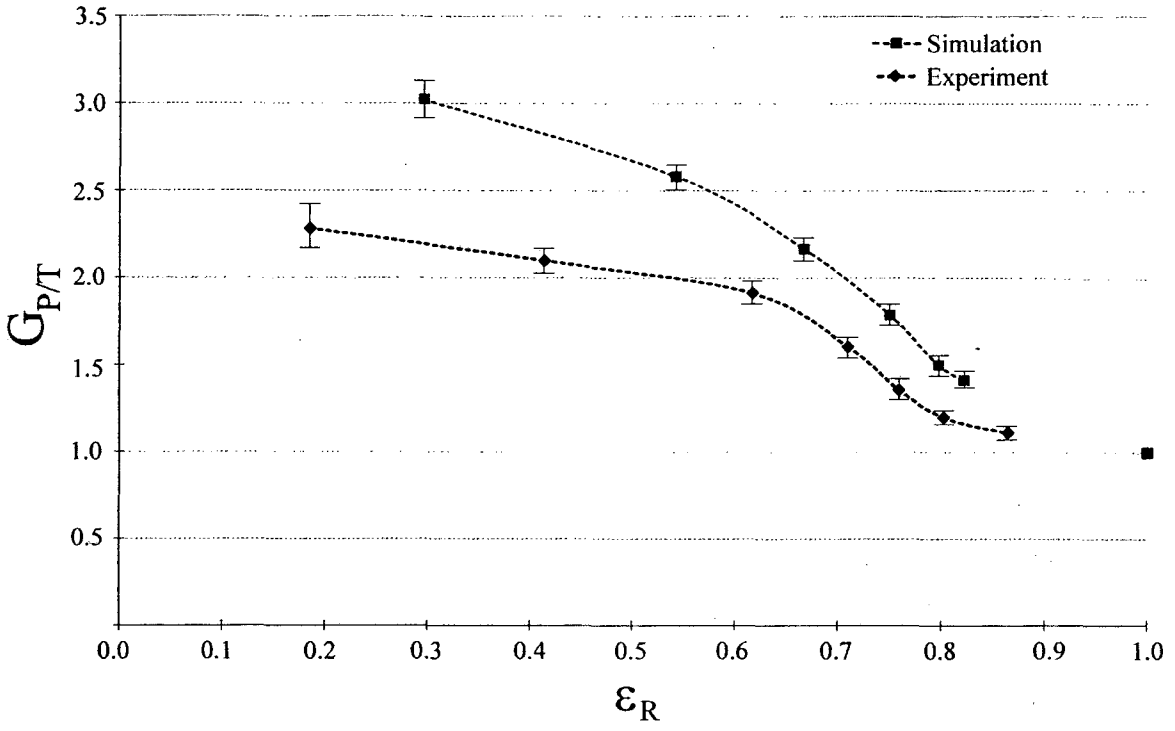

Figure 5.17: Relationship between the gain in P/T and ε_R in the ^{137}Cs experiment and simulation as thresholds are placed on the FM. The data point to the far right marks the $G_{P/T}$ prior to tracking for each. The error bars in ε_R are small relative to the point size.

Thresholds were placed on the *FM* to examine the behavior of the *P/T* ratio for the simulated events. Because of the difference in *P/T* between the simulation and experimental measurement prior to tracking, the gain in *P/T* ($G_{P/T}$) is used rather than the absolute value. This allows a more direct comparison of the two. Figure 5.17 shows the $G_{P/T}$ as thresholds are placed on the *FM* for both the simulated and experimentally measured events. As decreasing thresholds are placed on the *FM* (moving right to left on the curves), the $G_{P/T}$ for the simulation is consistently larger than that measured in the experiment. This reflects the fact that, on average, the *FM*s for the full-energy events in

the simulation are smaller than that in the experiment (see Figure 5.16). Several reasons for the improved *FM*s in the simulation as compared to the experiment will be discussed in Section 5.4.

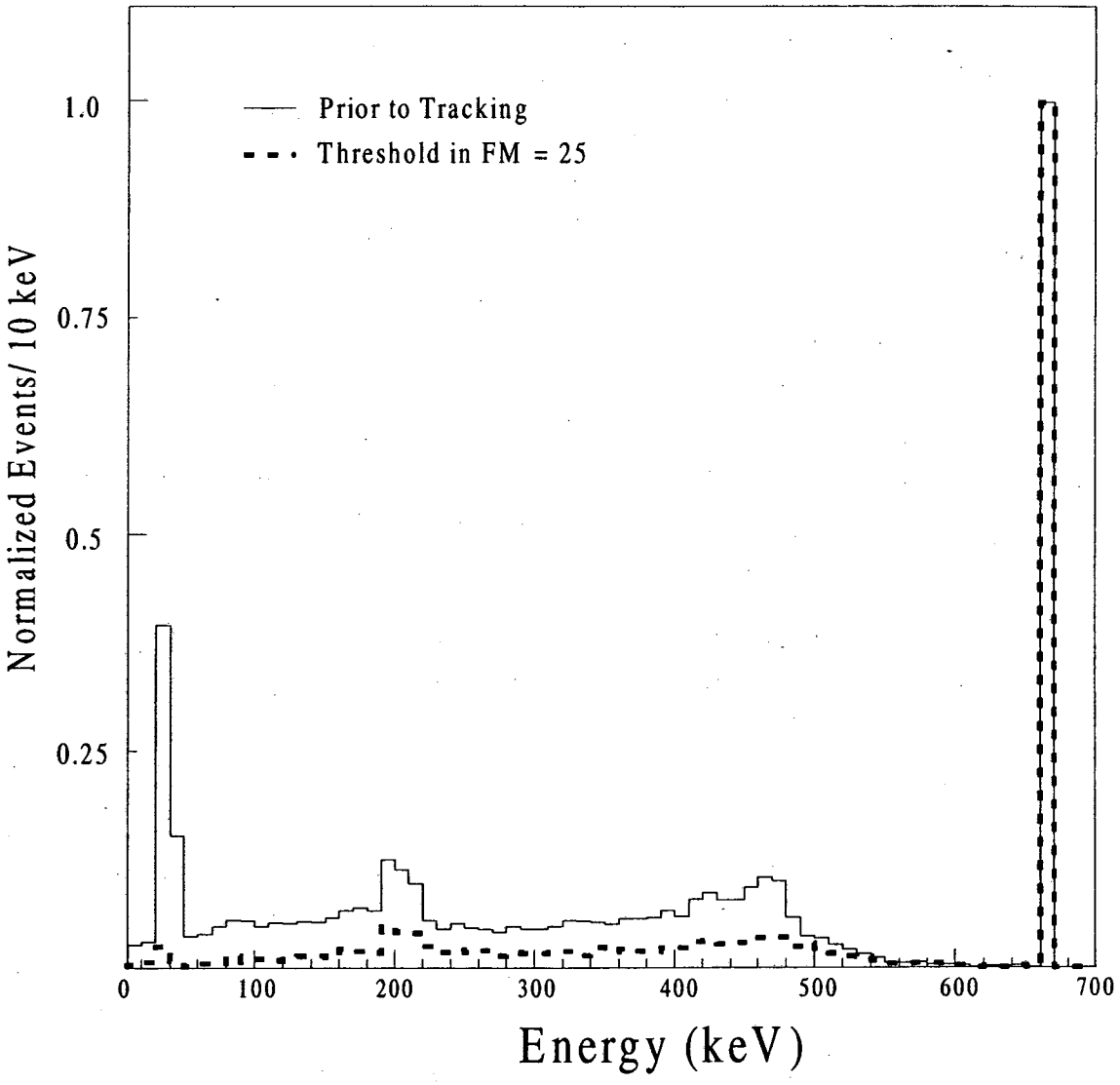

Figure 5.18: Total-energy spectrum for the 12,000 simulated ^{137}Cs events prior to tracking (solid line) along with the energy spectrum after tracking for a FM threshold of 25 (dashed line). The events in the 661.7 keV peaks have been normalized to one.

In order to compare simulated and experimentally measured energy spectrums obtained through the implementation of tracking, a spectrum at a *FM* threshold of 25 (the same as that used to create the experimental spectrum in Figure 5.6) was produced for the simulation and is shown in Figure 5.18. The simulated energy spectrum prior to tracking (normalized to the number of events in the 661.7 keV peak) is shown as reference. The *P/T* increases from 0.221 to 0.478 $\pm$ 0.011 with an ε_R = 0.67 $\pm$ 0.02 after the threshold is applied. As a means of comparing the change in shape of the spectrum after tracking for both the simulation and experiment, the ratio of the number of events per energy bin before tracking to the number of events per energy bin after tracking is shown in Figure 5.19. This ratio, below 661.7 keV, represents the factor by which the partial-energy events are reduced. The overall shape of the simulation and experiment are in good agreement with one another. The ratio of partial-energy events removed is slightly larger for the simulation over the energy range of the spectrum. This is consistent with the larger $G_{P/T}$ for the simulation as compared to the experiment (see Figure 5.17). The increased reduction in partial-energy events becoming pronounced below 200 keV reflects the increase in the number of single interactions at lower energies.

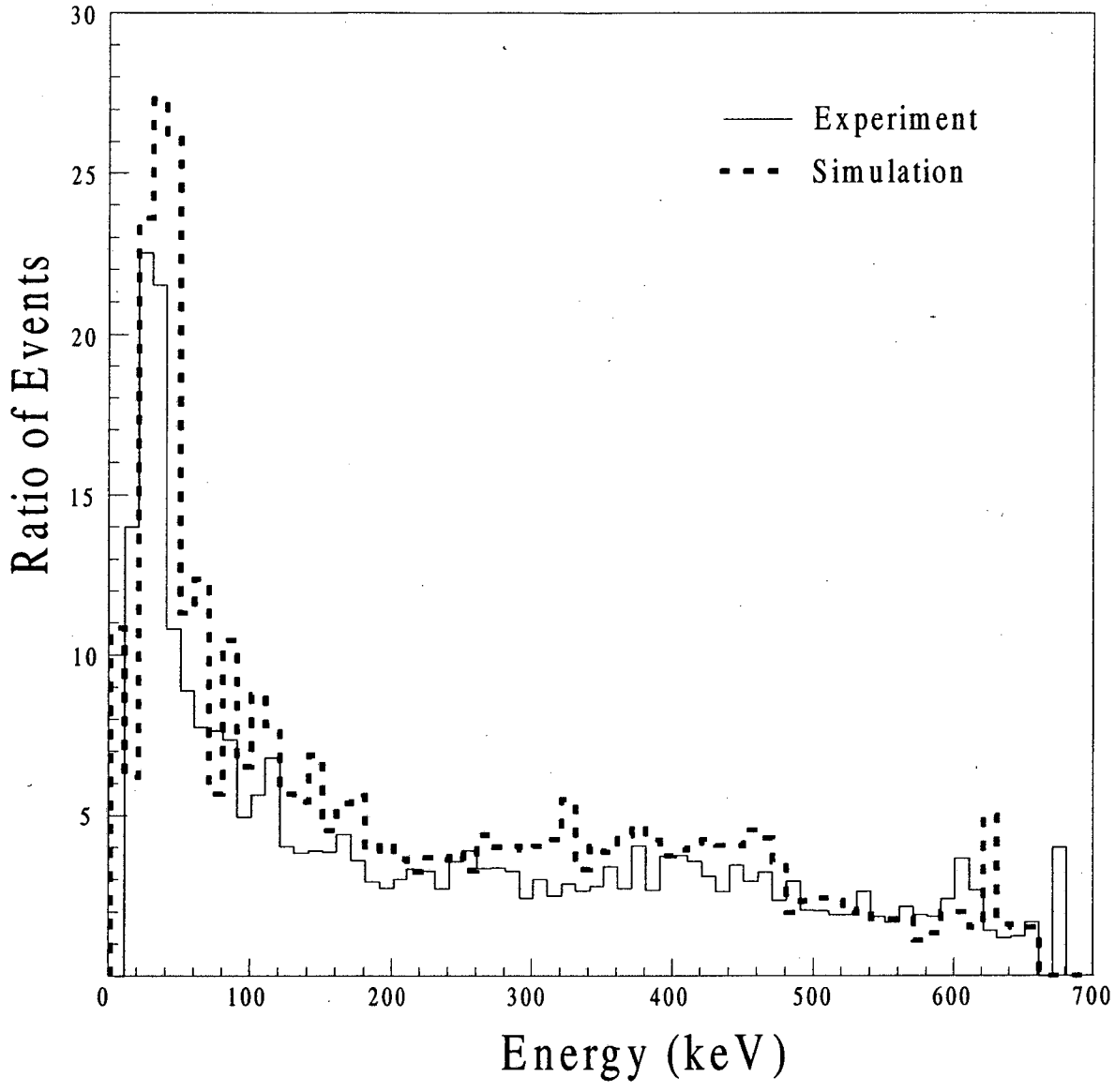

Figure 5.19: Ratio of the number of events in 10 keV intervals in the energy spectra before and after tracking for ^{137}Cs experiment (solid line) and simulation (dashed line).

5.3.2 Results for the Simulation of ^{60}Co and Comparison to Experiment

Simulations were performed for γ rays of 1.173 and 1.332 MeV emitted from the source with equal intensity to obtain a total of 19,500 events after the sorting process. The total-energy spectrum, prior to tracking, is shown in Figure 5.20 for the simulation as well as that experimentally measured (shown previously in Figure 5.7). Again, the Compton continuum of background events is larger in the experimentally measured spectrum, becoming more pronounced at lower energies. The reason for this difference is the same as that mentioned for the ^{137}Cs source (e.g. the inability to accurately model the physical environment). The difference seen here is larger than that of the ^{137}Cs simulation due to the higher-energy of the emitted γ rays. The mean free path of the ^{60}Co photons are longer, allowing them to interact with a larger portion of the environment, and thus increasing their chance of scattering into the detector. This is evident in the increased *P/T* ratios for the simulation of 0.090 ± 0.002 and 0.078 ± 0.002 as compared to those experimentally measured of 0.059 ± 0.002 and 0.049 ± 0.002 for the 1.173 and 1.332 MeV peaks, respectively.

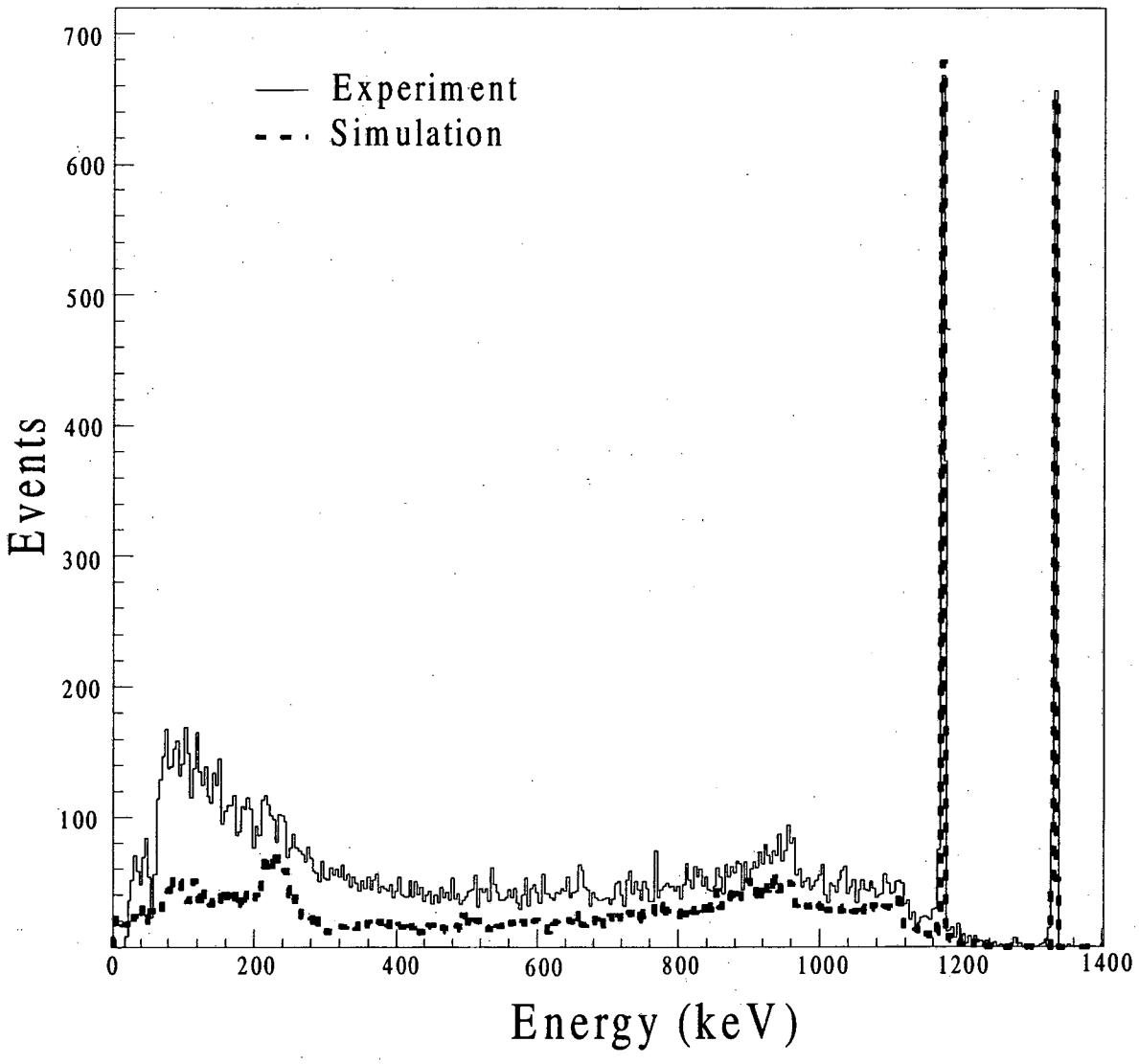

Figure 5.20: Total-energy spectrum for the 19,500 ^{60}Co events prior to tracking for the experiment (solid line) along with the simulation (dashed line).

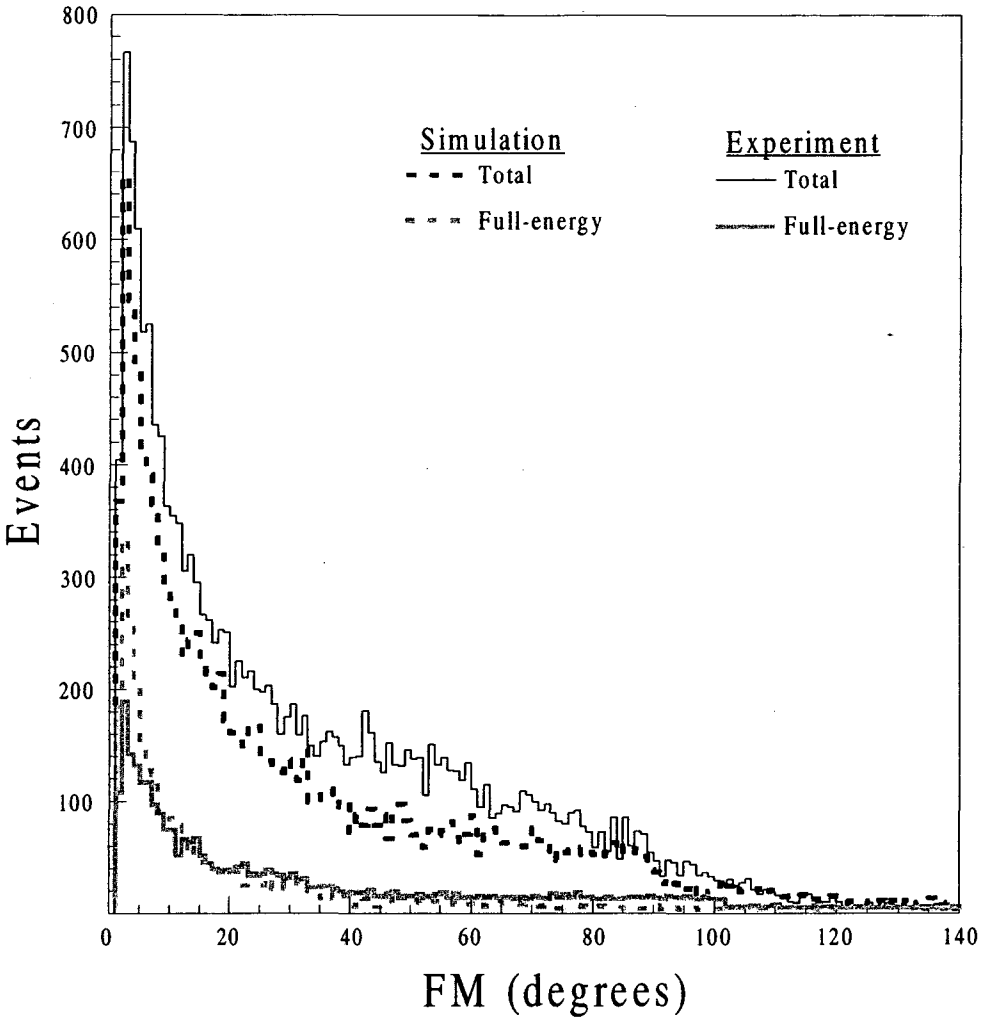

Figure 5.21: Distribution of FMs calculated in the ^{60}Co experiment (solid lines) and the simulation (dashed lines). The total distribution is separated into the full-energy components for each.

The distribution of *FM*s for the simulated events as well as that of the experiment is shown in Figure 5.21. The separate full-energy components are also shown. Again, the full-energy *FM*s in the simulation are more narrowly distributed while the total distributions are fairly consistent with one another. As thresholds are place on the *FM*, the $G_{P/T}$ is used to compare the simulation with the experiment.

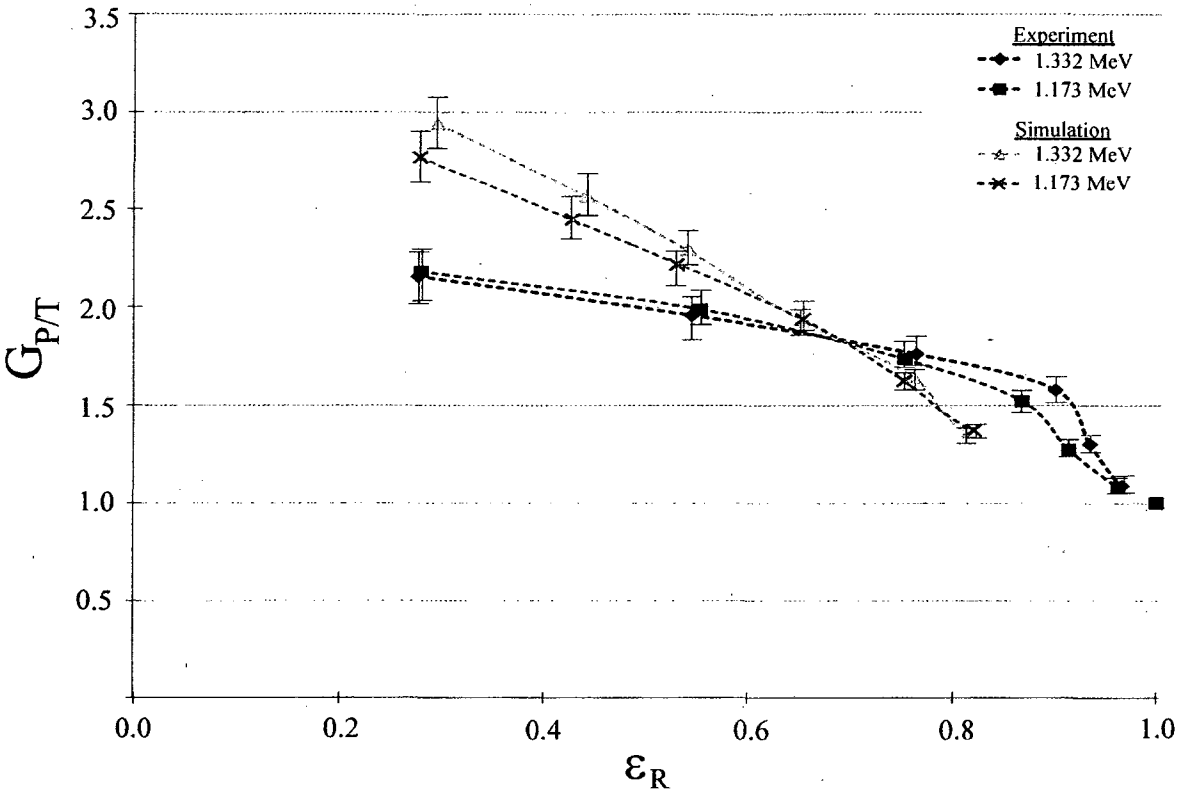

Figure 5.22: Relationship between the gain in P/T and ε_R in the ^{60}Co experiment and simulation as thresholds are placed on the FM. The data point to the far right marks the $G_{P/T}$ prior to tracking for each. The error bars in ε_R are small relative to the point size.

Figure 5.22 shows the behavior of the $G_{P/T}$ and ε_R for the 1.173 and 1.332 MeV peaks in simulation and experiment. Noticeably, upon the implementation of tracking the drop in ε_R (or fraction of single interactions removed) is greater in the simulation, marked by the far right data point of each curve. The fraction of single interactions returned in the signal decomposition for both peaks in the experiment is about 3% while in the simulation it is about 16%. The Monte Carlo transport calculations predict the fraction to be about 9%. Therefore, when measured signals are decomposed the process is prone to misidentify single interactions as two, giving rise to the smaller percentage of single

interactions found. The exact opposite is true in the simulation and more single interactions are found. The same behavior is present in the ^{137}Cs but to a lesser extent. This is reinforced by the findings in the previous section where there was a greater tendency for the ^{137}Cs x-rays to be misidentified as two interactions in the experiment. This gave rise to the difference in the shape of the *FM* distribution as compared to that of the simulation.

When comparing the $G_{P/T}$ curves it is important to realize that the data points moving right to left on the curves represent the same sequence of decreasing *FM* thresholds. Therefore, at any given point, the $G_{P/T}$ is greater in the simulation. This behavior is expected given the narrower distribution of full-energy *FMs* in the simulation as compared to the experiment (see Figure 5.21). The same feature was seen in the ^{137}Cs data and reasons for this will be discussed in the following section. In order to compare a simulated energy spectrum obtained by applying tracking with one experimentally measured, a *FM* threshold of 20 was used. Figure 5.23 shows the energy spectra before (shown previously in Figure 5.20) and after tracking for the simulation, normalized to the number of events in the 1.173 MeV peak. After the threshold is applied, the *P/T* increases from 0.090 to 0.178 $\pm$ 0.003 and 0.078 to 0.158 $\pm$ 0.003 for the 1.173 and 1.332 MeV peaks, respectively. This comes with a change in ε_R from one to 0.58 $\pm$ 0.03 at 1.173 MeV and 0.60 $\pm$ 0.03 at 1.332 MeV. The change in shape of the energy spectrum after tracking for the simulation and experiment can be compared in the same manner as performed for the ^{137}Cs. Figure 5.24 shows the ratio of the number of events per energy bin before and after tracking in the simulation and experiment. The ratio, over the majority of the spectrum, is larger in the simulation. This is consistent with the larger

$G_{P/T}$ in the simulation as compared to the experiment. Again, the increase in the ratio below about 200 keV reflects the increase in the number of single interactions at these energies.

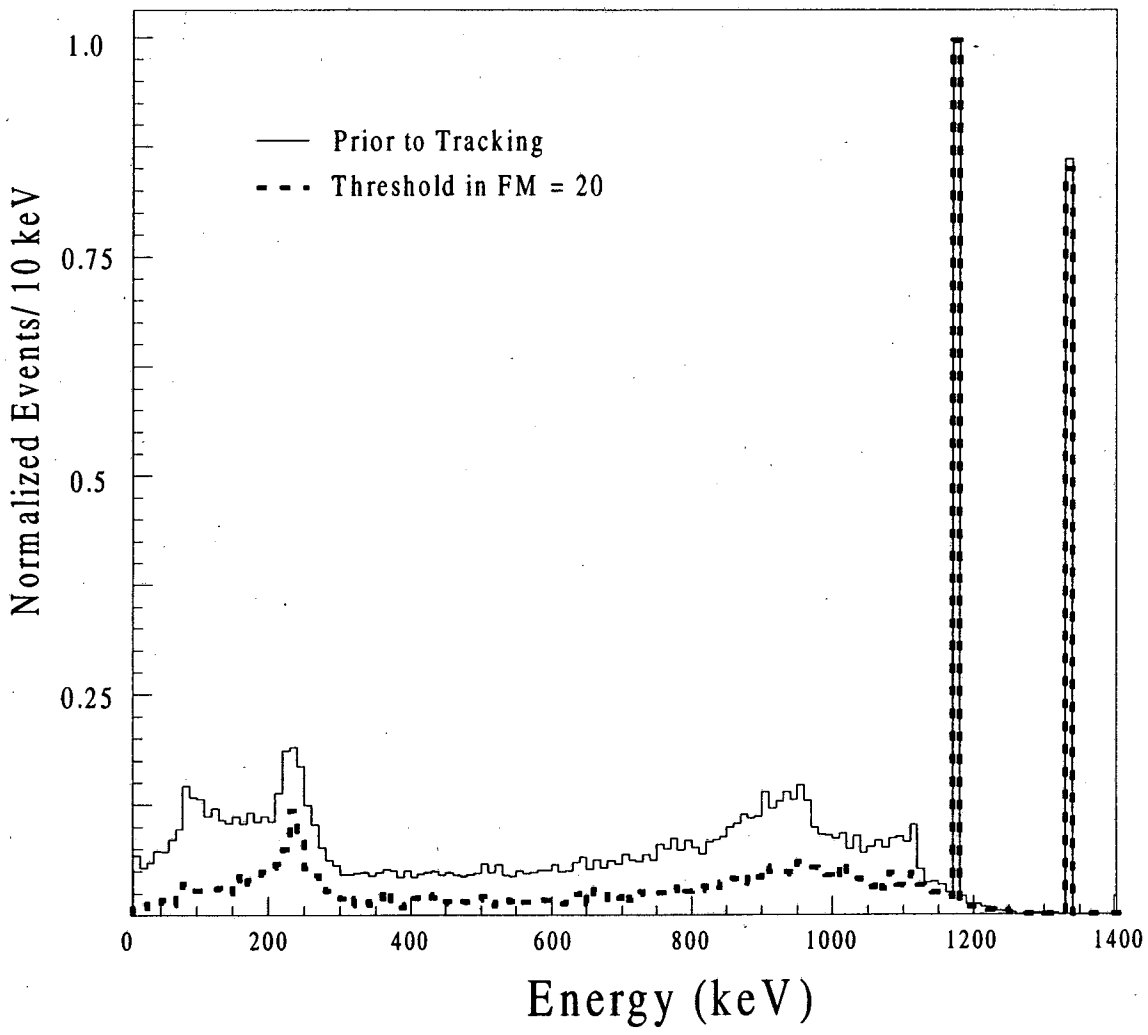

Figure 5.23: Total-energy spectrum for the 19,500 simulated ^{60}Co events prior to tracking (solid line) along with the energy spectrum after tracking for a FM threshold of 20 (dashed line). The events in the 1.173 MeV peaks have been normalized to one.

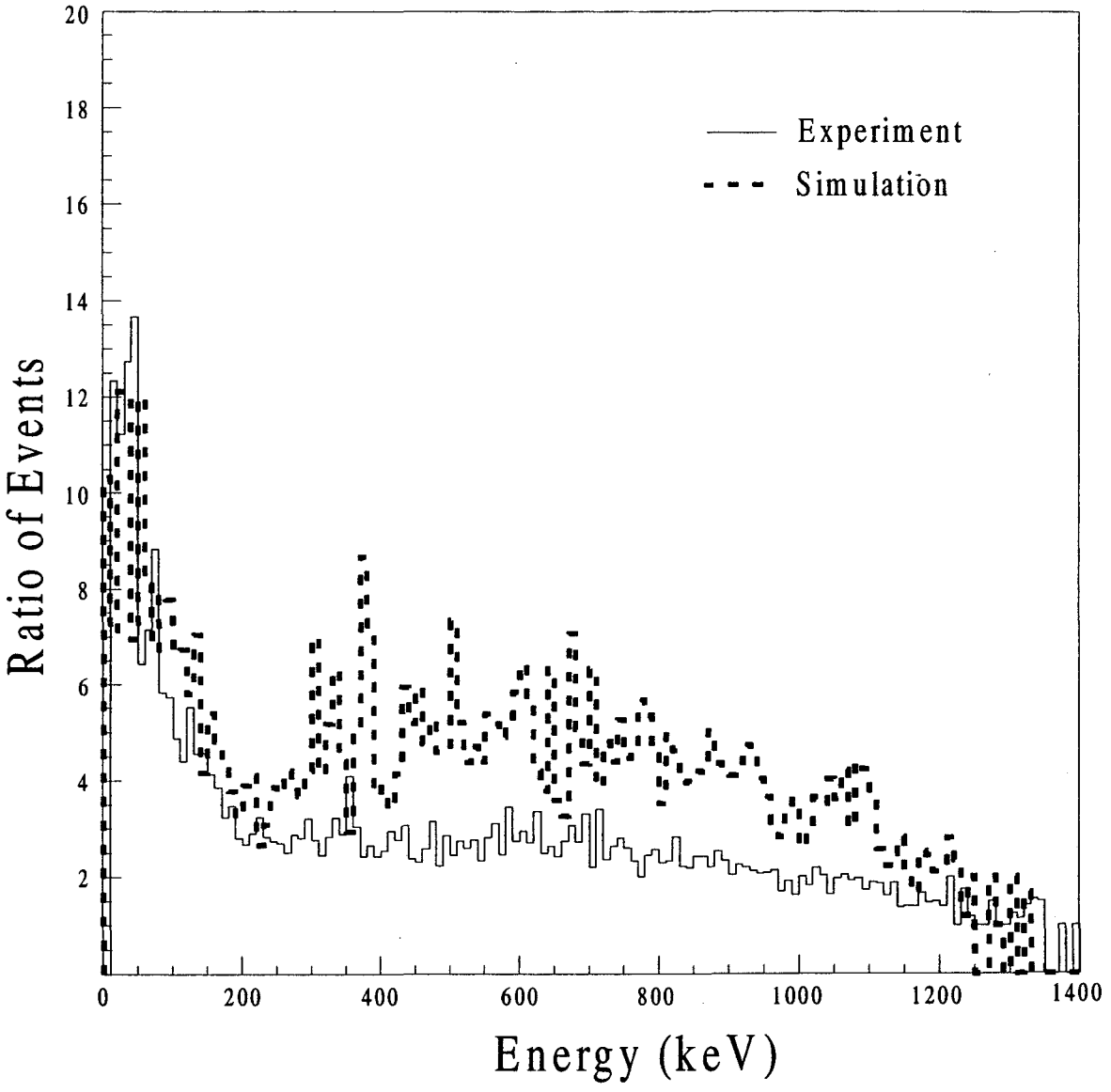

Figure 5.24: Ratio of the number of events in 10 keV intervals in the energy spectra before and after tracking for ^{60}Co experiment (solid line) and simulation (dashed line).

5.4 Discussion

A complete tracking process was implemented for both experimentally measured and simulated data. It was shown that the *P/T* ratio could be increased, from that obtained prior to tracking, by distinguishing full- and partial-energy events based on their figure-of-merit (*FM*). As evident in their narrower distribution of full-energy *FMs*, the gain in *P/T* was significantly higher in both the ^{137}Cs and ^{60}Co simulations as compared to the experiments. Several factors contribute to this difference.

First, the ability to align the start of a measured pulse shape with the basis pulse shapes in the signal decomposition contributes to differences between the experiment and simulation. To accurately fit the shape of a measure pulse to the basis, the start of the two pulses must be aligned. However, the 40 MHz ADC system employed dictates the accuracy of this alignment. Because the measured charge is recorded at 25 ns intervals, the start of the pulse can only be aligned to the basis pulse shapes with this accuracy. This is not an issue in the simulation because only calculated pulse shapes are used, and thus the start of the pulse shapes that are input in the signal decomposition algorithm and the basis pulse shapes are always consistent. The misalignment of measured pulse shapes with the basis functions will contribute to inaccuracies in the signal decomposition process. This problem, however, can be rather easily addressed. Simply employing an ADC system with a higher sampling frequency will lessen this problem.

The most pressing issue is the agreement between the experimentally measured pulse shapes and those theoretically calculated to form the basis pulse shapes in the signal decomposition process. In some cases, significant deviations between the calculated and

experimental pulse shapes are present. As discussed in Chapter 3, these deviations are a result of many factors such as the three dimensional spatial distribution of charge carriers, variations in impurity concentration, and fluctuations in electric field values near electrode surfaces. This leads to added inaccuracies in localizing interactions during the signal decomposition of experimentally measured pulse shapes as compared to the calculated pulse shapes used in the simulation. Evidence of this is reinforced by the findings in the ^{137}Cs experiment. In regions near the electrode surfaces the signal decomposition process had a greater tendency to misidentify the x-ray events as two interactions in the experiment as compared to simulation. In general, the same is true for the full-energy events in both the ^{137}Cs and ^{60}Co experiments. This suggests that the misidentification of single interactions as two interactions acts to compensate deviations between the experimentally measured pulse shapes and modeled basis pulse shapes in the signal decomposition process. The only way to correct this is to incorporate additional physical phenomena into the model to better parameterize the pulse shapes.

Chapter 6

CONCLUSIONS

The research presented in this dissertation has led to a number of contributions in the development and implementation of γ-ray tracking with a segmented coaxial HPGe detector. For the first time, studies were performed to compare theoretically calculated pulse shapes to those measured in a prototype GRETA detector. In addition, the position sensitivity was examined for one and two interactions occurring in a single segment throughout the volume of the detector. Finally, a signal decomposition and tracking algorithm was implemented to obtain tracking results for both experimentally measured and simulated data. The findings of this research are summarized here, along with ideas for future research that will be beneficial to GRETA and the possibilities of other applications of γ-ray tracking.

6.1 Results

It was experimentally shown through the implementation of rather simple pulse shape modeling and signal decomposition/tracking algorithms that distention between full- and partial-energy events measured in the prototype detector could be made and thus

increase the P/T ratio in the resulting energy spectrum. Just as will be performed with GRETA, this was achieved without the use of shielding detectors or knowledge of the emitted γ-ray energy. However, when compared to the results of the simulation the gain in P/T was significantly less in the experimentally measured data. The reasons for these differences are reinforced by the findings in the comparison between experimentally measured and calculated pulse shapes and the position sensitivity studies.

When interactions were localized within a small volume of the detector, the general features of the experimental pulse shapes were reproduced by those calculated using the model. However, significant deviations between the two were observed in some cases. These deviations contribute to the differences between the results obtained with the experimentally measured and simulated data in the implementation of tracking. In order to improve their agreement additional physical phenomena must be included in the modeling of the signal generation processes, along with more accurate electronic characterization of the detector crystal. This is crucial in optimizing the performance of GRETA.

In addition, the findings of the position sensitivity studies showed that the separation required to distinguish two interactions from that of a single interaction between them was, on average, considerably larger than the desired position resolution of 2 mm in the larger detector segments. These findings are consistent with those obtained in the analysis of the signal decomposition algorithm and tracking experiments where a tendency to misidentify two interactions as one and visa versa was present. In order to reduce this effect and improve the performance of GRETA detectors, the segmentation scheme of future detectors must be changed. The larger detector segments (i.e. 4 and 5)

must be reduced in size to that comparable of segments 1-3 and thus increase their sensitivity.

6.2 Future Work

As with all research, new questions arise and motivate the need for further inquiries. It is evident from the findings of this research that the parameterization and modeling of pulse shapes is one area that requires further investigation. In particular, the effect that the range of the primary electron, three-dimensional spatial distributions and drift properties of charge carriers, and electronic characterization of the detector crystal have on the ability of the model to accurately represent experimentally measured pulse shapes should be investigated. This requires that pulse shapes from single interactions be recorded over a broader range of the detector volume to ensure that the parameterization is consistent throughout the crystal.

In addition, the multiple-interaction position sensitivity should be investigated as it relates to changes in the segmentation scheme of the detectors. Such changes are necessary to increase the likelihood of properly distinguishing events with one or two interactions occurring in a single detector segment. Ultimately, simulations of the tracking process can be performed to determine the potential gain changes in the segmentation have on the P/T and relative efficiency.

While the performance of the signal decomposition algorithm was consistent with the findings of the position sensitivity studies, there are areas that should be investigated to determine if potential improvements could be made. One method maybe to include the

physical phenomena involved in the interaction of radiation with matter to increase the success of properly identifying interactions. As a simple example, one can potentially use the energy deposition in the segment to aid in predicting the number of interactions that took place. In the current algorithm, as the amount of energy deposited in a segment goes down (decreasing the signal-to-noise ratio) the likelihood that a single interaction is misidentified as two goes up. In reality, however, the probability that two interactions occur decreases due to an increase in the photoelectric absorption cross-section. Such physical phenomena are not currently considered in the decomposition process and thus their inclusion could greatly increase the performance of the tracking process. Furthermore, the algorithm is rather computation intensive and would prove to be very time consuming when utilized with the high data rates expected in GRETA. Other decomposition methods based on wavelet transformations and artificial neural networks should be investigated as a means of reducing computation time.

6.3 Other Applications

While the focus of this dissertation was on γ-ray tracking of radiation emitted from a known source location, the same basic principles can potentially be applied to localize and characterize unknown γ-ray sources. A system similar to GRETA could be used to define the incident angle of detected radiation using the Compton scattering formula rather than determining if the event comprised the full-energy of the γ ray. In effect, this would image the source of radiation. This could have applications in a wide range of fields from astrophysics to nuclear medicine.

Currently, in the field of astrophysics Compton camera systems are used to define the incident direction of radiation. However, these systems require the use of two detectors separate by a large distance. This arrangement restricts the solid angle coverage and greatly reduces the efficiency of the system. Segmented HPGe detectors could potentially eliminate the need for separate detectors and thus increase the efficiency of the system.

Additionally, applications can be envisioned in the field of medical imaging. For example, in nuclear medicine γ-ray detectors are used to image the distribution of radioactive tracers administered to find physiological abnormalities in the human body. Current techniques such as single photon emission computed tomography (SPECT) and position emission tomography (PET) generally use detectors that are collimated to define the direction of the incident photons. Tracking could potentially be used to define the incident direction of the photon without the need for collimation. This would greatly increase the efficiency of the system and result in decreased measuring time and/or reduced activity received by the patient. Each of these factors would be beneficial in the treatment process.

Bibliography

[1] A.J. Tavendale and G.T. Ewan, "A High Resolution Lithium-drifted Germanium Gamma-ray Spectrometer," *Nucl. Instr. and Meth. A*, vol. 25, pp. 185, 1963.

[2] R.H. Pehl, R.C. Cordi, and F.S. Goulding, "High-Purity Germanium: Detector Fabrication and Performance," *IEEE Trans. Nucl. Sci.*, vol. 19, pp. 265-269, 1972.

[3] G. Knoll, *Radiation Detection and Measurement*. 2nd Ed., New York: John Wiley & Sons, 1989.

[4] P.J. Nolan, D.W. Gifford, and P.J. Twin, "The Performance of a Bismuth Germanate Escape Suppressed Spectrometer," *Nucl. Instr. and Meth. A*, vol. 236, pp. 95, 1985.

[5] I.Y. Lee, "Gamma-ray tracking detectors," *Nucl. Instr. and Meth. A*, vol. 422, pp. 195-200, 1999.

[6] Gammasphere Proposal, ed. M.A. Delephanque and R.M. Diamond, Lawrence Berkeley National Laboratory, Report 5202, 1988.

[7] P.J. Twin et al., "Observation of a Discrete-line Superdeformed Band up to 60h in ^{152}Dy," *Phys. Rev. Lett.* , vol. 57, pp. 811, 1986.

[8] M.A. Deleplanque et al., "GRETA: Utilizing new concepts in gamma-ray detection," *Nucl. Instr. and Meth. A*, vol. 430, pp. 292-310, 1999.

[9] Proposal for a GRETA Module Cluster, ed. I.Y. Lee and K. Vetter, Lawrence Berkeley National Laboratory, Report March 2000.

[10] R.D. Evans, *The Atomic Nucleus*. New York: McGraw-Hill, 1955.

[11] G. Bertolini and A. Coche, *Semiconductor Detectors*. Amsterdam: Elsevier - North Holland, 1968.

[12] W.L. Hansen and E.E. Haller, "Fabrication Techniques for Reverse Electrode Coaxial Germanium Nuclear Radiation Detectors," *IEEE Trans. Nucl. Sci.*, vol. 28, No. 1, pp. 541-543, 1981.

[13] W.L. Hansen and E.E. Haller, "High-Purity Germanium Crystal Growing," *Proc. Mat. Res. Soc. 1982 Annual Meeting*, Symposium F, Nuclear Radiation Detector Materials, E. E. Haller, H. W. Kraner and W. A. Higinbotham, eds., Elsevier Science Publishing Inc., New York, vol. 16, pp. 1-16, 1983.

[14] E.E. Haller and F.S. Goulding, "Nuclear Radiation Detectors," *Handbook on Semiconductors*, 2nd Ed., vol. 4, Elsevier North-Holland Inc., New York, pp. 1-54, 1993.

[15] J. Llacer, "Planar and Coaxial High Purity Germanium Radiation Detectors," *Nucl. Instr. and Meth. A*, vol. 98, pp. 259, 1972.

[16] K. Vetter. Personal Communication.

[17] A. Kuhn, *Effects of the Anisotropy in Charge Carrier Drift Velocity on Position-Sensitive Germanium Detectors.* Master's Thesis, University of California at Berkeley, 1999.

[18] G. Ottaviani, C. Canali, and A. Quaranta, "Charge carrier transport properties of semiconductor materials suitable for nuclear radiation detectors," *IEEE Trans. Nucl. Sci.*, vol. 22, pp. 192-204, 1975.

[19] L. Reggiani, C. Canali, F. Nava, and G. Ottaviani, "Hole Drift Velocity in Germanium," *Phys. Rev. B*, vol. 16, pp. 2781, 1977.

[20] W. Sasaki, M. Shibuya and K. Mizuguchi, "Anisotropy of hot electrons in n-type germanium," *J. Phys. Soc. of Japan*, vol. 13, pp. 456-460, 1956.

[21] I.Y. Lee. Personal Communication.

[22] A. van der Ziel, *Proc. IRE* pp. 1808, 1962.

[23] V. Radeka, "Field Effect Transistors for Charge Amplifiers," *IEEE Trans. Nucl. Sci.*, vol. 20, pp. 182, 1973.

[24] J. Blair et al., "Spatial Resolution Attainable in Germanium Detectors by Pulse Shape Analysis," *Nucl. Instr. and Meth. A*, vol. 422, pp. 331-336, 1999.

[25] W. Shockley, "Currents to Conductors Induced by Moving Point Charge," *J. Appl. Phys.*, vol. 9, pp. 635-636, 1938.

[26] S. Ramo, "Currents Induced by Electron Motion," *Proc. IRE*, vol. 27, pp. 584-585, 1939.

[27] L.S. Darken et al., "Mechanism for Fast Neutron Damage of Ge(HP) Detectors," *Nucl. Instr. and Meth. A*, vol. 171, pp. 49, 1980.

[28] B. Hubbard-Nelson et al., "A Module for Energy and Pulse Shape Data Acquisition," *Nucl. Instr. and Meth. A*, vol. 422, pp. 411, 1999.

[29] B. Philhour et al., "Simulations of Pulse Shape Discrimination (PSD) Techniques for Background Reduction in Germanium Detectors," *Nucl. Instr. and Meth. A*, vol. 403, pp. 136-150, 1998.

[30] Th. Kroll et al., "Analysis of Simulated and Measured Pulse Shapes of Closed-ended Coaxial HPGe Detectors," *Nucl. Instr. and Meth. A*, vol. 371, pp. 489-496, 1996.

[31] F.S. Goulding and D. Landis, "GAMMASHPERE - Correction Technique for Detector Charge Trapping," *IEEE Trans. Nucl. Sci.*, vol. 41, pp. 1145, 1994.

[32] S. Mahajan and K.S. Sree Harsha, *Principles of Growth and Processing of Semiconductors*. New York: McGraw-Hill, 1999.

[33] E. Brown et al., *Table of Isotopes*. 7th Ed., New York: John Wiley & Sons, 1978.

[34] GEANT3, Detector Description and Simulation Tool. CERN, Geneva, 1993.

[35] J. Turner. *Atoms, Radiation, and Radiation Protection*. 2nd Ed. New York: John Wiley & Sons, Inc. 1995.

[36] T. Mukoyama, "Range of Electrons and Positrons," *Nucl. Instr. and Meth. A*,vol. 134, pp. 125-127, 1976.

[37] R.A. Kroeger, N. Gehrels, W.N. Johnson et al., "Charge Spreading and Position Sensitivity in a Segmented Planar Germanium Detector," *Nucl. Instr. and Meth. A*, vol. 422, pp. 206-210, 1999.

[38] P.N. Luke, N.W. Madden and F.S. Goulding, "Germanium Detectors with a Built-In Transverse Drift Field," *IEEE Trans. Nucl. Sci.*, vol. 32, pp. 457, 1985.

[39] P. Rehak et al., "Semiconductor Drift Chambers for Position and Energy Measurements," *Nucl. Instr. and Meth. A*, vol. 235, pp. 224, 1985.

[40] W. Press et al. *Numerical Recipes in C: The Art of Scientific Computing*. Cambridge University Press. 1992.

[41] K. Vetter, A. Kuhn, I.Y. Lee et al., "Performance of the GRETA Prototype Detectors," *Nucl. Instr. and Meth. A*, vol. 452, pp. 105-114, 2000.

[42] M. Amman and P.N. Luke, "Three-dimensional Position Sensing and Field Shaping in Orthogonal-strip Germanium Gamma-ray Detectors," *Nucl. Instr. and Meth. A*, vol. 452, pp. 155-166, 2000.

[43] E. Gatti, A. Geraci, G. Casati et al., "Spatial Localization of Multiple Simultaneous Hits in Segmented Detectors: A New Algorithm," *Nucl. Instr. and Meth. A*, vol. 458, pp. 738-744, 2001.

[44] *NAG Fortran Library: Introductory Guide, Mark 19.* Numerical Algorithms Group Limited, 1999.

[45] P.E. Gill et al., "User's Guide for NPSOL," Version 4, *Report SOL*, 86-2, Dept. of Operations Research, Stanford University, 1986.

[46] M.J. Powell. *Introduction to Constrained Optimization: Numerical Methods for Constrained Optimization.* Academic Press, 1974.

[47] R. Fletcher. *Practical Methods of Optimization.* 2nd Ed. New York: John Wiley & Sons, Inc. 1987.

[48] P.E. Gill et al. *Practical Optimization.* Academic Press. 1981.

[49] M.J. Powell. *Mathematical Programming: The State of the Art.* Springer - Verlag. 1983.

[50] G.J. Schmid et al., "A γ-ray tracking algorithm for the GRETA spectrometer," *Nucl. Instr. and Meth. A*, vol. 430, pp. 69-83, 1999.

[51] E. Gatti et al., "Timing of Pulses of any Shape with Arbitrary Constraints and Noises: Optimum Filters Synthesis Method," *Nucl. Instr. and Meth. A*, vol. 457, pp. 347-355, 2001.

[52] V.T. Jordanov et al., "Digital techniques for real-time pulse shaping in radiation measurements," *Nucl. Instr. and Meth. A*, vol. 353, pp. 261-264, 1994.

[53] V.T. Jordanov et al., "Digital synthesis of pulse shapes in real time for high resolution radiation spectroscopy," *Nucl. Instr. and Meth. A*, vol. 345, pp. 337-345, 1994.

[54] V.T. Jordanov and G.F. Knoll, "Digital Pulse Processor Using A Moving Average Technique," *IEEE Trans. Nucl. Sci.*, vol. 40, pp. 764-769, 1993.

[55] A.O. Macchiavelli, "Physics of Gammasphere," *Proc. Euro. Phys. Soc. XVI 1998*, Nuclear Physics Division Conference, S. Lunardi, R.A. Ricci and W. von Oertzen, eds., vol. III, pp. 589-599, 1998.

Ernest Orlando Lawrence Berkeley National Laboratory
One Cyclotron Road | Berkeley, California 94720

Prepared for the U.S. Department of Energy under Contract No. DE-AC03-76SF00098